UNIVERSIDADE DE LISBOA
INSTITUTO SUPERIOR TÉCNICO

CRITICAL PHENOMENA IN GRAVITATIONAL COLLAPSE

Beyond spherical symmetry

ISABEL SUÁREZ FERNÁNDEZ

SUPERVISOR : Doctor David Matthew Hilditch

CO-SUPERVISOR : Doctor Miguel Rodrigues Zilhão Nogueira

THESIS APPROVED IN PUBLIC SESSION TO OBTAIN THE PHD DEGREE IN PHYSICS

JURY FINAL CLASSIFICATION: PASS WITH DISTINCTION

2022

TÉCNICO LISBOA

UNIVERSIDADE DE LISBOA
INSTITUTO SUPERIOR TÉCNICO

CRITICAL PHENOMENA IN GRAVITATIONAL COLLAPSE

Beyond spherical symmetry

ISABEL SUÁREZ FERNÁNDEZ

SUPERVISOR : Doctor David Matthew Hilditch

CO-SUPERVISOR : Doctor Miguel Rodrigues Zilhão Nogueira

THESIS APPROVED IN PUBLIC SESSION TO OBTAIN THE PHD DEGREE IN PHYSICS

JURY FINAL CLASSIFICATION: PASS WITH DISTINCTION

JURY

CHAIRPERSON : Doctor José Pizarro de Sande e Lemos, Instituto Superior Técnico, Universidade de Lisboa

MEMBERS OF THE COMMITTEE :

Doctor Ulrich Sperhake, School of Mathematics, University of Cambridge, UK

Doctor Isabel Cordero Carrión, Facultad de matemáticas, Universidad de Valencia, Spain

Doctor David Mathew Hilditch, Instituto Superior Técnico, Universidade de Lisboa

Doctor Alex Vano Vinuales, Instituto Superior Técnico, Universidade de Lisboa

FUNDING INSTITUTION:

Fundação para a Ciência e Tecnologia (PD/BD/135434/2017)

Fundação para a Ciência e Tecnologia (COVID/BD/152485/2022)

2022

RESUMO

Há evidencia numérica que indica que em relatividade geral soluções perto do limite de formação de um buraco negro em simetria esférica têm um comportamento crítico, isto é, existe invariância de escala, universalidade e comportamento de lei de potências. Porém, quando se abandona esta simetria, estes fenómenos ainda não estão totalmente compreendidos. Este manuscrito contém evidencia de que quando se deixa a simetria esférica nem todas as características de colapso crítico se mantêm.

Primeiro, como estudar um sistema na relatividade geral sem restrições de simetria é computacionalmente custoso e desafiante, é desejável construir modelos que reproduzam o quadro do colapso crítico e que sejam mais simples de estudar. Na primeira parte deste documento estes modelos são construídos em espaço-tempo plano. Começando com deformações da equação de onda, estes modelos admitem solução analítica e é possível mostrar que a solução limite tem auto simetria discreta. Estas soluções limite são estudadas no cone de luz passado do ponto de explosão. Em simetria esférica há um sentido no qual a solução crítica é única. Também são apresentadas evoluções numéricas esféricas para modelos mais gerais, os quais mostram um comportamento semelhante. Fora da simetria esférica as soluções limite têm mais liberdade. Diferentes topologias para a explosão são possíveis, e até a solução crítica precisa de uma reinterpretação localmente como uma família parametrizada.

A segunda parte deste manuscrito tem uma abordagem mais canónica para explorar o colapso crítico para além da simetria esférica. Usando ferramentas da relatividade numérica, o colapso de ondas gravitacionais no vácuo é estudado. Primeiro, para levar a cabo as ditas evoluções numéricas, os dados iniciais são sumamente importantes. Motivado por estudos de fenómenos críticos nesta configuração, duas abordagens comuns para a construção de dados iniciais do tipo de ondas gravitacionais são comparados a nível linear. Em particular, dados iniciais tipo ondas de Brill são construídos analiticamente e comparados com ondas de Teukolsky, numa tentativa de compreender o comportamento numérico diferente que estes dois tipos de dados iniciais apresentam. Em geral, as ondas de Brill têm momentos multipolares mais altos do que as ondas de Teukolsky, que são puramente quadrupolares. Isto poderia ser uma explicação para as diferenças observadas na evolução dinâmica destes dois tipos de ondas. Porém, para uma escolha típica da função de semente das ondas de Brill, todos os momentos de ordem elevada são cancelados identicamente, o que faz os dados iniciais de Brill no regime linear serem surpreenden-

temente semelhantes aos de Teukolsky para uma escolha semelhante da sua função de semente.

Por último, empregando as ondas de Brill já mencionadas, ondas gravitacionais axi-simétricas e sem torção são evoluídas perto do limite do colapso com o código pseudo-espectral de relatividade numérica `bamps`. Esta é a primeira aplicação da nova funcionalidade de refinamento de malha adaptável. Seis famílias diferentes de dados de Brill que dependem de um único parâmetro são consideradas; duas centradas e quatro descentradas, das quais as últimas nunca foram anteriormente estudadas. Para cada família, o parâmetro é ajustado até o limite da formação de buraco negro. Os resultados para as famílias centradas concordam com a literatura. Os resultados chave são os seguintes. Primeiro, perto do limite de colapso o pico global da curvatura aparece no eixo de simetria mais afastado da origem, o que indica que no limite o colapso aconteceria em redor de dois centros separados. Isto era já conhecido para as famílias centradas, pois horizontes aparentes foram encontrados explicitamente. Agora, a mesma prova é dada para duas das famílias descentradas. Segundo, não se encontrou evidência de auto simetria discreta nem de uma lei de potências universal no escalamento do escalar de curvatura. Finalmente, são observadas algumas características universais na curvatura, em concordância com estudos prévios. Estas características aparecem várias vezes em cada espaço-tempo individual perto do limite do colapso e, para além disso, estão presentas nas seis famílias.

PALAVRAS-CHAVE: relatividade geral; relatividade numérica; fenómenos críticos; colapso gravitacional, ondas gravitacionais.

ABSTRACT

There is numerical evidence implying that in general relativity solutions near the threshold of black hole formation in spherical symmetry follow critical behavior, this is, scale-invariance, universality and power-law scaling. However, when abandoning such symmetry the full extent of critical phenomena in gravitational collapse has yet to be completely understood. This manuscript contains compelling evidence that when dropping spherical symmetry not all the features of critical collapse carry over.

First, as investigating numerically a system in general relativity without symmetry restrictions is both, computationally expensive and challenging, it is desirable to construct models that vindicate the picture of critical collapse that are easier to study. In the first part of this document, such models are constructed in flat spacetime. Starting with deformations of the wave equation these models admit analytical solutions, and it is possible to show that they have discrete self-similar threshold solutions. These threshold solutions are studied in the past light cone of the blowup point. In spherical symmetry there is a sense in which a unique critical solution exists. Spherical numerical evolutions are also presented for more general models, and exhibit similar behavior. Away from spherical symmetry threshold solutions attain more freedom. Different topologies of blowup are possible, and even locally the critical solution needs reinterpretation as a parametrized family.

The second part of this manuscript has a more canonical approach to exploring critical collapse beyond spherical symmetry. Using tools from numerical relativity, collapse of gravitational waves in vacuum is studied. First, to carry out such numerical evolutions, initial data are of great importance. Motivated by studies of critical phenomena in such a setup, two common approaches to constructing gravitational wave initial data are compared at the linear level. In particular, Brill wave initial data are constructed analytically and compared with Teukolsky waves in an attempt to understand the different numerical behavior observed in dynamical nonlinear evolutions of these two different sets of initial data. In general, Brill waves feature higher multipole moments than the quadrupolar Teukolsky waves, which might have explained the differences observed in the dynamical evolution of the two types of waves. However, for a common choice of the Brill wave seed function, all higher order moments vanish identically, rendering the linear Brill initial data surprisingly similar to the Teukolsky data for a similarly common choice of its seed function.

Last, using the Brill waves mentioned above, twist-free, axisymmetric gravitational waves are evolved close to the threshold of collapse with the pseudospectral numerical relativity code `bamps`. This is the first application of the new adaptive mesh refinement functionality of the code. Six different one-parameter families of Brill wave initial data are considered; two centered and four off-centered, of which the latter have not been treated before. Within each family the parameter towards the threshold of black hole formation is tuned. The results for the centered families agree with the literature. The key results are first, that close to the threshold of collapse the global peak in the curvature appears on the symmetry axis but away from the origin, indicating that in the limit the collapse would happen around two disjoint centers. This was known for the centered by families by explicitly finding a pair of separated apparent horizons around these peaks, and now the same empirical evidence is given for two of the off-centered families. Second, evidence neither for strict discrete self-similarity nor for universal power-law scaling of curvature quantities is found. Finally, approximately universal strong curvature features are observed, in agreement with previous work. These features appear multiple times within individual spacetimes close to the threshold and are furthermore present within all six families.

KEY-WORDS: general relativity; numerical relativity; critical phenomena, gravitational collapse, gravitational waves.

PUBLICATIONS

This doctoral thesis is based on the following publications:

I. Suárez Fernández, S. Renkhoff, D. Cors Agulló, B. Bruegmann, D. Hilditch, *Evolution of Brill waves with an adaptive pseudospectral method*,; arXiv:2007.13764 [gr-qc].

I. Suárez Fernández, T. W. Baumgarte and D. Hilditch, *Comparison of linear Brill and Teukolsky waves*, Phys. Rev. D102 (2021) , 124036 ; arXiv:2111.04752 [gr-qc].

I. Suárez Fernández, R. Vicente and D. Hilitch, *Semilinear wave model for critical collapse*, Phys. Rev. D103 (2021), 044016; arXiv:2007.13764 [gr-qc].

ACKNOWLEDGMENTS

This doctoral thesis might have my name, but definitely, it would not be possible without you David. I had the enormous pleasure to share my PhD journey with you as my supervisor, from whom I have learned not only physics but also personally. Thank you for always believing in me, pushing me further and giving me your help, advice and support every time I needed it. I am proud to call you my supervisor, and also my friend.

I also want to thank my co-supervisor Miguel Zilhão for always being available to discuss physics, give advice and especially for thoroughly reading this manuscript.

I developed my PhD within GRIT, as part of CENTRA at Instituto Superior Técnico. I had the opportunity to meet excellent scientists and amazing colleagues. Thanks to you all for creating this nice work environment, for all the interesting discussions, group meetings and seminars. In particular, thanks to those of you who spent some of your time helping me to improve this manuscript.

I am thankful as well to Thomas Baumgarte. Your scientific work is enlightening and served to construct the base of my numerical relativity knowledge. Working with you was very inspiring and an honor.

João Vasconcelos, the computer genius. Thank you so much for all the hours you spent, with endless patience, solving every computer-related issue that I faced. This thesis would not be possible without your technical support.

Rita Teixeira, you are the hero of the department and you should be properly acknowledged. You always receive us with a smile on your face and helped us countless times. Bureaucrary is less bad thanks to you.

It is very important to feel good in your workplace, and you all guys made me feel always comfortable and welcome. Krinio, Christian, Arianna, Tiago, Francisco... thank you for your support, interesting office discussions and random jokes. Sharing an office with you was great.

To the Jena crew, Bernd, Florian, Sarah, Daniela... thank you for your hospitality during my time there and the fruitful scientific work. Espe-

cially to you, Daniela, work can also lead to friendships.

To my *cosmic guapos*, Lorenzo and Thanasis. You know this journey would not be possible without you two. I will never forget our crazy travel adventures, Lisbon nights and neverending laughs. Thank you for your friendship, you will always have a place wherever I am. Viva el Señor Trapemar.

Rodrigo, you also deserve special mention. I not only had the pleasure of working with you but also being your friend. I hope we never stop discussing physics and politics.

Lisbon gave me incredible people, Rebecca, Diogo, Chrysalena, Eloy, Eli, Isma, Liandra, Juliana... I am grateful to have you all in my life. Your support made the path easier and my time in Lisbon beautiful.

João, *meu companheiro*. Words are not enough to descibe it. Obrigada.

To my people from Santiago: Miguel, Miriam, Diego, Carlos, Ali... and of course to Sito and Ventosela, the best corner to drown PhD students' tears in good wine and company.

To my Galician friends, Bea, Lito, Prada and Miguel, always ready to offer moral support. Thank you, guys.

I am very grateful to my parents, for the support and for the patience in driving to and from Porto every time, so I could come back home.

To Hélder and all the circus friends from Chapitô, Aurore, Laura, Fede, Alex, Filipe, Tiago, Zé, Fanny, Astrid, Leonor, Elena and you all. Thanks to you I discovered a new passion. Your always fun classes and companionship definitely made this last year of PhD easier to handle. Whatever had happened, the good vibes you all have always saved the day.

To all the brave women before me that made possible that today I stand where I am.

This work was supported by the IDPASC program with the FCT grants PD/BD/135434/2017 and COVID/BD/152485/2022.

I acknowledge the hospitality of the physics department of Jena Friedrich-Schiller-Universitaet during my time there.

CONTENTS

LIST OF FIGURES

LIST OF TABLES

CONVENTIONS, NOTATION AND UNITS

Unless stated otherwise, I use geometrized units ($c = G = 1$) and work with the *mostly positive* metric signature $(- + + +)$.

$\alpha, \beta, \gamma, ...$	spacetime indices (from 0 to 3)
$i, j, k, ...$	3-spatial indices (from 1 to 3)
$V_\alpha W^\alpha \equiv \sum_{\alpha=0}^{3} V_\alpha W^\alpha$	Einstein's notation
$T_{(\alpha_1 \dots \alpha_l)} \equiv= \frac{1}{l!} \sum_\sigma T_{\alpha_{\sigma(1)} \dots \alpha_{\sigma(l)}}$	symmet. over all permutat. σ
$g_{\alpha\beta}$, $\eta_{\alpha\beta}$	curved, flat spacetime metric
γ_{ij}	3D spatial metric
$\partial_\alpha(\cdot) = \frac{\partial}{\partial x^\alpha}(\cdot)$	coord. derivative
$\nabla_\alpha(\cdot)$	Levi-Civita derivative
$\Box(\cdot) \equiv \nabla_\alpha \nabla^\alpha(\cdot)$	Levi-Civita d'Alembertian

ACRONYMS

ADM	Arnowitt-Deser-Misner
AH	Apparent Horizon
AMR	Adaptive Mesh Refinement
BH	Black Hole
BKL	Belinskii-Lifschitz-Khalatnikov
BSSN	Baumgarte-Shapiro-Shibata-Nakamura
CSS	Continuos Self-Similarity
DF	Dual Foliation
DSS	Discrete Self-Similarity
GHG	Generalized Harmonic Gauge

GR	General Relativity
GW	Gravitational Wave
IBVP	Initial Boundary Value Problem
IVP	Initial Value Problem
NR	Numerical Relativity
PDE	Partial Differential Equation
SCC	Strong Cosmic Censorship
SM	Standard Model
TT	Transverse Traceless
WCC	Weak Cosmic Censorship

INTRODUCTION TO THIS MANUSCRIPT

1

INTRODUCTION TO CRITICAL PHENOMENA IN GRAVITATIONAL COLLAPSE

Using numerical methods to solve Einstein equations of General Relativity (GR) is nowadays its own field of study, known as Numerical Relativity (NR). In the last decades, enormous advances have been made in order to solve complex problems, mainly in the strong-field regime, using this approach to GR together with the help of supercomputers (see [1] for a review). In this manuscript critical phenomena in gravitational collapse are studied from the point of view of NR, which is the connecting thread along with this whole work, which serves, once again, to emphasize the usefulness of NR in the study of extreme spacetimes. First of all, it is of main importance to contextualize this work. The title of this thesis is "critical phenomena in gravitational collapse: Beyond spherical symmetry", which is, already, a non-trivial title. Through the next sections of this introduction the main concepts will be reviewed, starting with the theory of GR, followed by the explanation of the basic concepts of NR, and extending on what critical phenomena are and how they play a role within the gravitational context.

1.1 THEORY OF GENERAL RELATIVITY

The theory of General Relativity (GR), also known as Einstein's theory of gravity, is the current most accepted theory to explain gravity and its properties. This geometric theory was proposed by Albert Einstein in 1915 and since then has been reviewed and collected by many authors. In this manuscript, I will give a small review for the reader that is already familiar with the subject, as the objective is to give the context of this work. For the unfamiliar reader I recommend reading the canonical textbooks [2–7] for a more detailed explanation of GR.

GR is a geometric theory that sees the spacetime as a differentiable four dimensional Lorentzian manifold $(\mathcal{M}, g)$ with a non-degenerate metric tensor $g_{\alpha\beta}$ of signature $(-,+,+,+)$ with the associated Levi-Civita covariant derivative ∇_α. The notion of causality is introduced by the line element, which in coordinates x^α is expressed as

$$ds^2 = g_{\alpha\beta} dx^\alpha dx^\beta, \tag{1.1}$$

often called the infinitesimal interval. This object gives information about the causal structure of the spacetime, as two events that are infinitesimally close can be causally related only if they are in the light cone of each other. That mean both events are connected by a null or timelike path. For a timelike path it is possible to define the proper time

$$\Delta\tau = \int_{\lambda_i}^{\lambda_f} \sqrt{-g_{\alpha\beta}(\lambda)\frac{dx^\alpha}{d\lambda}\frac{dx^\beta}{d\lambda}}d\lambda. \tag{1.2}$$

In the case of null paths the interval is zero, therefore no extra definitions are needed. In the case of spacelike path one can define the path lenght

$$\Delta\tau = \int_{\lambda_i}^{\lambda_f} \sqrt{g_{\alpha\beta}(\lambda)\frac{dx^\alpha}{d\lambda}\frac{dx^\beta}{d\lambda}}d\lambda. \tag{1.3}$$

The affine connection which is compatible with the metric ($\nabla_\alpha g_{\beta\gamma} = 0$), also known as Levi-Civita connection or the Christoffel symbols $\Gamma^\alpha_{\beta\gamma}$ is given by

$$\Gamma^\alpha{}_{\beta\gamma} = \frac{1}{2}g^{\alpha\delta}\left(\partial_\gamma g_{\delta\beta} + \partial_\beta g_{\gamma\delta} - \partial_\delta g_{\beta\gamma}\right), \tag{1.4}$$

which is symmetric $\Gamma^\alpha{}_{\beta\gamma} = \Gamma^\alpha{}_{\gamma\beta}$. The object which measures the failure of ∇_α to commute is the Riemann curvature tensor

$$R^\alpha{}_{\beta\gamma\delta} = \partial_\gamma\Gamma^\alpha{}_{\beta\delta} - \partial_\delta\Gamma^\alpha{}_{\beta\gamma} + \Gamma^\alpha{}_{\rho\gamma}\Gamma^\rho{}_{\beta\delta} - \Gamma^\alpha{}_{\rho\delta}\Gamma^\rho{}_{\beta\gamma}, \tag{1.5}$$

which is symmetric in the index pairs $R_{\alpha\beta\gamma\delta} = R_{\gamma\delta\alpha\beta}$ and anti-symmetric on each pair $R_{\alpha\beta\gamma\delta} = -R_{\beta\alpha\gamma\delta} = R_{\beta\alpha\delta\gamma}$. The Ricci tensor is defined by contracting two indices

$$R_{\alpha\beta} = R^\gamma{}_{\alpha\gamma\beta}, \tag{1.6}$$

which is also symmetric $R_{\alpha\beta} = R_{\beta\alpha}$. The Ricci scalar or scalar curvature is defined as

$$R = R^\alpha{}_\alpha. \tag{1.7}$$

(Note that the Einstein notation for summation when contracting indices is used).

The main idea behind GR is that the gravitational field is measured by the curvature of spacetime, and at the same time, this curvature is related to the presence of matter and energy. This is represented by the Einstein field equations

$$G_{\alpha\beta} = 8\pi T_{\alpha\beta}, \tag{1.8}$$

where $T_{\alpha\beta}$ is the stress-energy tensor, which is symmetric and represents the amount of mass-energy of the matter, and $G_{\alpha\beta}$ is called Einstein tensor,

$$G_{\alpha\beta} = R_{\alpha\beta} - \frac{1}{2} g_{\alpha\beta} R, \tag{1.9}$$

which is also symmetric. Note that in Eq. 1.8 geometrized units ($G = c = 1$) are used. This convention will be maintained through the whole manuscript unless otherwise stated.

By looking at Eq. 1.8, one can see that on the left hand side the curvature of the spacetime is present, and related to the right hand side which encodes energy, momentum, stress and strain. A revolutionary statement that lead to the modern understanding of gravity in a relativistic and geometric manner. The Einstein equations are a nonlinear system of Partial Differential Equations (PDEs) of second order in the metric. Moreover, these field equations imply the local conservation of energy-momentum. As a consequence of the Bianchi identity $\nabla_\rho R_{\alpha\beta\gamma\delta} + \nabla_\delta R_{\alpha\beta\rho\gamma} + \nabla_\gamma R_{\alpha\beta\delta\rho} = 0$, the divergence of the Einstein tensor vanishes, $\nabla_\beta G^{\alpha\beta} = 0$, and therefore

$$\nabla_\beta T^{\alpha\beta} = 0, \tag{1.10}$$

is a requirement for any system satisfying the Einstein equations.

Another important consequence of the Einstein equations is that in vacuum $T_{\alpha\beta} = 0$ the Ricci scalar vanishes $R = 0$, consequently the Ricci tensor does $R_{\alpha\beta} = 0$. Be aware, however, that this does not mean that the curvature of spacetime vanishes as well, since it is given by the Riemann tensor and only $R^\alpha{}_{\beta\gamma\delta} = 0$ means zero curvature (flat spacetime). This implication is of main importance in Part ii of this manuscript, where characteristics of Gravitational Waves (GW) are studied in vacuum and therefore, the curvature scalar R is not a good measure. Instead, another scalar (and thus gauge-invariant) becomes relevant, the Kretschmann scalar

$$I = R_{\alpha\beta\gamma\delta} R^{\alpha\beta\gamma\delta}. \tag{1.11}$$

A solution to the Einstein equations is given by the metric tensor and it is often expressed with the line element in the form of Eq. 1.1. These solutions depend on the matter model, however, it is also possible to have vacuum solutions $T_{\alpha\beta} = 0$. For instance, flat spacetime ($R^\alpha{}_{\beta\gamma\delta} = 0$) is represented by the Minkowski metric

$$ds^2 = -dt^2 + dx^2 + dy^2 + dz^2 = \eta_{\alpha\beta} dx^\alpha dx^\beta, \tag{1.12}$$

where $\eta_{\alpha\beta}$ will be hereafter referred as the flat metric or Minkowski metric.

A vacuum solution of main importance for this manuscript is the one corresponding to a Schwarzschild black hole (BH)

$$ds^2 = -\left(1 - \frac{2M}{r}\right) dt^2 + \left(1 - \frac{2M}{r}\right)^{-1} dr^2 + r^2 d\theta^2 + r^2 \sin^2\theta d\phi^2,$$

(1.13)

which represents a static, uncharged and non rotating BH where M is a constant with dimensions of mass in geometrized units. Note that in the limit of M going to zero Minkowski spacetime is recovered. The boundary of a Schwarzschild BH corresponds to $r = 2M$, a 3 dimensional hypersurface called the event horizon. Once something falls inside the event horizon it can never escape, not even light. Inside the BH, the integral lines of $\frac{\partial}{\partial r}$ are incomplete timelike geodesics, as they cannot be continued past the curvature singularity at $r = 0$. The nature of singularities is uncertain, but here it is considered the Hawking-Penrose definition, that a Lorentzian manifold $(\mathcal{M}, g)$ is singular if it is not geodesically complete. That is, there exists at least one geodesic which is inextendible in at least one direction but has only a finite range of affine parameter. For a more detailed discussion about spacetime singularities see Section 9.1 from [5] or [8]. This curvature singularity is causally disconnected from the rest of the universe as it is "protected" or "hidden" by the event horizon. It is fair to say that the singularity of a BH is the limit of GR as a valid theory. There are other solutions in GR that represent BHs, including rotating or charged BHs, however as BHs are not the main subject of this work extra details are not given and rather the notion of gravitational collapse is introduced.

To think about gravitational collapse in a heuristic manner one can think of a region of spacetime in which the curvature gets big enough such that the spacetime "collapses" and forms a BH. In other words, one can say that gravitational collapse happens when a BH forms in a region of the space where there was none before. Different scenarios, like a supernovae [9], might lead to collapse, however, the scenario relevant for this work is the collapse of GWs in vacuum. In order to connect with this let us introduce the notion of Apparent Horizon (AH). The AH is the marginally outer trapped surface on which the expansion of outgoing null geodesics vanishes. This is a *quasi-local* notion (i.e. local in time) of the boundary of a BH, in contrast with the event horizon, which is a *global* notion. The fact that the AH is defined quasi-locally makes it possible to build AH locators numerically (see Section 4.2.3). This tool will be used for the diagnosis of a spacetime in Chapter 4, where it will be considered that a spacetime contains a BH only if an AH is found.

Let us now for completeness introduce the notion of GW or gravitational radiation. GWs are undulations of the spacetime that propagate at the speed of light. These waves can normally be described in the linearized theory as

$$g_{\alpha\beta} = \eta_{\alpha\beta} + h_{\alpha\beta}, \quad |h_{\alpha\beta}| \ll 1, \tag{1.14}$$

where $\eta_{\alpha\beta}$ is the Minkowski metric and $h_{\alpha\beta}$ is the perturbation around flat space. Now, it is possible to define the trace-reversed wave perturbation

$$\bar{h}_{\alpha\beta} \equiv h_{\alpha\beta} - \frac{1}{2} h^{\gamma}{}_{\gamma} \eta_{\alpha\beta}. \tag{1.15}$$

Using the Lorentz gauge condition $\nabla_{\alpha} \bar{h}^{\alpha\beta} = 0$, the trace-reversed wave perturbation satisfies the wave equation

$$\Box \bar{h}_{\alpha\beta} = \nabla^{\gamma} \nabla_{\gamma} \bar{h}_{\alpha\beta} = 0, \tag{1.16}$$

and therefore, giving name to the GWs. For an extended textbook treatment see Chapter 9 in [10]. In fact, one of the biggest successes of GR was the prediction of GWs, whose detection was first reported in 2015 by the LIGO/VIRGO Collaboration [11].

1.2 NUMERICAL RELATIVITY

With the context, GR, clear, it is time to introduce the tool that is used in this manuscript, NR. In Chapter 4 an all-purpose NR code is used and in Chapter 2 a code in flat space but using a 3+1 spherical splitting as inspired by NR is employed. In this section, a brief review of the basic concepts of NR is given. For a textbook treatment see [10, 12–15].

NR is the tool that allows the scientific community to have, let us say, a laboratory in which to simulate the most extreme spacetime evolutions. It is, moreover, a very useful utensil to study fundamental properties of GR that are not possible to be addressed analytically. The biggest success of NR is providing part of the input for waveform modelling for the detection of GWs (see [16] for a review) together with the discovery of critical phenomena in gravitational collapse [17]. The most common approach to NR is the **3+1 formalism**. This formalism consists of slicing the four dimensional spacetime of Einstein equations into three dimensional spatial hypersurfaces Σ_t, such that the induced metric $\gamma_{\alpha\beta}$ has a positive signature (0,+,+,+). This procedure allows reformulating the equations as an Initial Value Problem (IVP) or Cauchy problem with constraints, as the equations are decomposed into "space" and "time". This 3+1 splitting is not an inherent structure of GR, actually, it depends on the choice of time coordinate. Let us explain the procedure. First of all consider a spacetime with metric $g_{\alpha\beta}$, which is globally hyperbolic and consequently can be foliated in several three dimensional spacelike hypersurfaces Σ_t as in Fig. 1.1.

Consider a particular spacetime foliation, as in Fig. 1.2, where two adjacent hypersurfaces are considered $(\Sigma_t, \Sigma_{t+dt})$. It is necessary to introduce the lapse function $\alpha(t, x^i)$ defined as

$$g^{tt} = g^{\mu\nu} \nabla_{\mu} t \nabla_{\nu} t \equiv \alpha^{-2}(t, x^i), \tag{1.17}$$

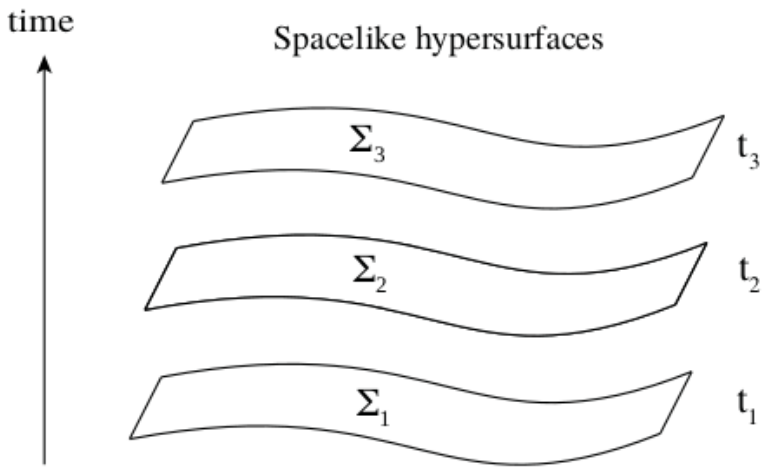

Figure 1.1: Figure 2.1 from [13] in which a foliation of the spacetime into three dimensional spacelike hypersurfaces is illustrated. t is a parameter that can be considered the universal time function (not necessarily the proper time) that labels the spatial hypersurfaces Σ_t.

and the unit normal vector to the spatial hypersurfaces Σ_t, corresponding to the 4-velocity of the normal observers,

$$n_\mu = -\alpha \nabla_\mu t. \tag{1.18}$$

The lapse of proper time $d\tau$ between the two hypersurfaces measured by a normal observer along a integral curve of n^μ is expressed as

$$\frac{d\tau}{dt} = \alpha(t, x^i). \tag{1.19}$$

With these quantities it is possible to define the projection operator onto de spacelike hypersurfaces Σ_t, that is, the spatial metric

$$\gamma_{\mu\nu} = g_{\mu\nu} + n_\mu n_\nu. \tag{1.20}$$

The time vector is defined as

$$t^\mu = \alpha n^\mu + \beta^\mu, \tag{1.21}$$

where β^μ is the shift vector and it is purely spatial $n^\mu \beta_\mu = 0$. The shift vector $\beta^i(t, x^i)$ is the relative velocity between normal observers and the lines of constant spatial coordinates

$$x^i_{t+dt} = x^i_t - \beta^i(t, x^i)dt. \tag{1.22}$$

The lapse α and the shift vector β^i are known as gauge functions since their determination is not unique and they carry information about the coordinates choice. The metric can be 3+1 split in terms of the gauge functions and the spatial metric as

$$ds^2 = (-\alpha^2 + \beta_i \beta^i)dt^2 + 2\beta_i dt dx^i + \gamma_{ij} dx^i dx^j, \tag{1.23}$$

where $\beta_i = \gamma_{ij}\beta^j$. In this coordinate system the unit normal vector can be written as

$$n^\mu = \left(\frac{1}{\alpha}, -\frac{\beta^i}{\alpha}\right),$$
$$n_\mu = (-\alpha, 0). \tag{1.24}$$

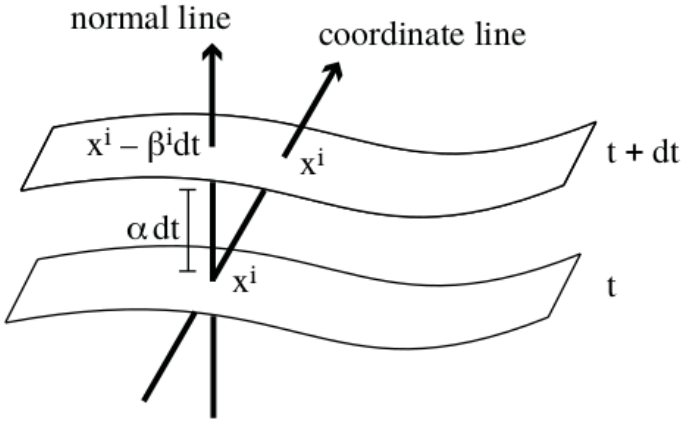

Figure 1.2: Figure 2.2 from [13] in which two consecutive hypersurfaces are shown with their respective parametrization in terms of the lapse α and the shift β^i.

Now, it is needed to differentiate between the intrinsic curvature (the one coming from the internal geometry of the hypersurfaces) and the extrinsic curvature, which is associated with how those hypersurfaces are embedded in the four dimensional spacetime. The extrinsic curvature tensor $K_{\mu\nu}$ is a measure of the change of the normal vector under parallel transport along the spacelike hypersurface Σ_t

$$K_{\mu\nu} = -P^\alpha{}_\mu \nabla_\alpha n_\nu = -(\nabla_\mu n_\nu + n_\mu n^\alpha \nabla_\alpha n_\nu), \tag{1.25}$$

which is symmetric, purely spatial and where $P^\alpha{}_\mu = \delta^\alpha{}_\mu + n^\alpha n_\mu$ is the projection operator onto the spatial hypersurfaces. The projection operator coincides with the induced spatial metric $P_{\alpha\beta} = \gamma_{\alpha\beta}$. The extrinsic curvature can also be written in terms of the Lie derivative along the normal vector of the spatial metric

$$K_{\mu\nu} = -\frac{1}{2}\mathcal{L}_n \gamma_{\mu\nu}, \tag{1.26}$$

where the Lie derivative along a vector X is defined as

$$\begin{aligned}\mathcal{L}_X T^{\alpha_1\ldots\alpha_r}{}_{\beta_1\ldots\beta_s} &= X^\gamma \partial_\gamma T^{\alpha_1\ldots\alpha_r}{}_{\beta_1\ldots\beta_r} \\ &- (\partial_\gamma X^{\alpha_1}) T^{\gamma\alpha_2\ldots\alpha_r}{}_{\beta_1\ldots\beta_s} - \ldots - (\partial_\gamma X^{\alpha_r}) T^{\alpha_1\ldots\alpha_{r-1}\gamma}{}_{\beta_1\ldots\beta_s} \\ &+ (\partial_{\beta_1} X^\gamma) T^{\alpha_1\ldots\alpha_r}{}_{\gamma\beta_2\ldots\beta_s} + \ldots + (\partial_{\beta_s} X^\gamma) T^{\alpha_1\ldots\alpha_r}{}_{\beta_1\ldots\beta_{s-1}\gamma}.\end{aligned} \tag{1.27}$$

In order to write the Einstein equations as a Cauchy problem, evolution equations for the spatial metric and the extrinsic curvature are

needed. The evolution equation for the three dimensional spatial metric is purely kinematic, that is, it comes from rewriting the definition of extrinsic curvature Eq. 1.25 and results in

$$\partial_t \gamma_{ij} = -2\alpha K_{ij} + D_i\beta_j + D_j\beta_i, \tag{1.28}$$

where D_i is the three dimensional spatial covariant derivative associated with γ_{ij}. The evolution equation for the extrinsic curvature, which encodes the dynamics of the system, corresponds to

$$\begin{aligned}\partial_t K_{ij} - \mathcal{L}_\beta K_{ij} = &-D_i D_j\alpha + \alpha\left[{}^{(3)}R_{ij} + KK_{ij} - 2K_{ik}K^k{}_j\right] \\ &+ 4\pi\alpha\left[\gamma_{ij}(S-\rho) - 2S_{ij}\right],\end{aligned} \tag{1.29}$$

where $S_{\mu\nu} = P^\alpha{}_\mu P^\beta{}_\nu T_{\alpha\beta}$ is the spatial stress tensor measured by the normal observers with $S = S^\mu{}_\mu$.

These evolution equations by themselves are not equivalent to the Einstein equations. The 3+1 decomposition also includes the spatial constraint equations. These remaining equations correspond to the relation between dynamical variables that must be satisfied at all times. They only depend on the spatial derivatives and are independent of the gauge functions α and β^i. The first constraint comes from contracting the Einstein field equations with the normal vector twice. It is called the Hamiltonian or energy constraint

$${}^{(3)}R + K^2 - K_{\mu\nu}K^{\mu\nu} = 16\pi\rho \tag{1.30}$$

where $\rho = n^\mu n^\nu T_{\mu\nu}$ is the local energy density as measured by the normal observers. The second constraint comes from projecting the Einstein field equations into the spacelike hypersurfaces and then contracting with the normal vector. This is called the Momentum constraint (which corresponds actually to three equations)

$$D_\mu\left(K^{\alpha\mu} - \gamma^{\alpha\mu}K\right) = 8\pi j^\alpha, \tag{1.31}$$

where $j^\alpha = -P^{\alpha\mu}n^\nu T_{\mu\nu}$ is the momentum density as measured by the normal observers.

The group of Eqs. 1.28, 1.29, 1.30 and 1.31, are commonly referred to as the standard Arnowitt-Deser-Misner (ADM) equations. However, this is not the original form from [18], rather this is the non-trivial rewriting by York [19]. Nevertheless, these are the base equations employed for evolutions in NR. It is important to note, however, that is possible to add arbitrarily multiples of the constraints to these equations, therefore, their formulation is nonunique. One might ask why someone should do this, and the answer is that the physical solutions of the system will always remain the same, but the mathematical properties and how they behave under small constraint violations (a fact that always happens when working with NR) may differ.

There is a wide variety of ways to choose these additions, together with different choices of coordinates. For a summary of different strategies see Chapter 5 from [13] or Chapter 11 from [10]. Probably the most

famous are Z4 [20–25] and Baumgarte-Shapiro-Shibata-Nakamura (BSSN) [26–28] using moving-puncture coordinates. Due to the fact that these formulations are strongly hyperbolic, they have a well-posed IVP. An alternative formulation is Generalized Harmonic Gauge (GHG) [29–31], for which GR is represented as a symmetric hyperbolic system, and therefore, it has a well-posed Initial Boundary Value Problem (IBVP) for which the boundary conditions are required to be constraint preserving and radiation controlling [32]. The GHG formalism is implemented inside `bamps`, the code used for the evolutions of GWs in vacuum in Chapter 4. For a detailed explanation of this formalism see [33] and [34].

1.3 CRITICAL PHENOMENA

Following the structure of the title of this thesis, it is time to explain what critical phenomena are and how they play a role in the gravitational context. Critical phenomena are by definition the name of the physics of critical points. This type of phenomenology appears in several fields of physics, such as thermodynamics (for instance gas-liquid phase transition), magnetism (as the ferromagnetic phase transition) and in GR in the gravitational collapse (at least in spherical symmetry). Critical phenomena, in general, are characterized by three main features: power-law scaling of the order parameter with a critical universal exponent, universality of the critical solution, and scale-invariance. To go deeper into each of these features, let us use the main topic of this manuscript, critical phenomena in gravitational collapse as an example to follow the discussion, and then make the analogy with other physical systems.

1.3.1 *Theory: Critical phenomena in spherical symmetry*

Most of what is well known about critical phenomena in gravitational collapse, independently of the matter model, concerns the spherically symmetric setting. In this section, I give a brief review of the basic theory on this topic, for which the standard picture of critical phenomena corresponds to the spherical symmetry restriction and it is well exemplified by the massless scalar field collapse [17]. For a detailed review of this subject see [35, 36], however, be aware that some of the aspects discussed here will change beyond spherical symmetry thanks to the contributions to this topic in the recent years, including further Chapters of this thesis.

Critical phenomena in gravitational collapse were discovered in 1993, one of the breakthroughs of NR, by Choptuik [17], where he

considered a minimally coupled real massless scalar field ϕ to gravity in spherical symmetry. The action of such a system corresponds to

$$\mathcal{S} = \int \sqrt{-g}\,(R - 8\pi\nabla_\alpha\phi\nabla^\alpha\phi)\,d^4x, \tag{1.32}$$

and the stress-energy tensor for a massless scalar field corresponds to

$$T_{\alpha\beta} = \nabla_\alpha\phi\nabla_\beta\phi - \frac{1}{2}g_{\alpha\beta}\nabla_\gamma\phi\nabla^\gamma\phi. \tag{1.33}$$

The general spherically symmetric line element in Schwarzschild coordinates is

$$ds^2 = -\alpha^2(r,t)dt^2 + a^2(r,t)dr^2 + r^2d\Omega^2, \tag{1.34}$$

where the field equations are

$$\begin{aligned}
&\dot{\Phi} = \left(\frac{\alpha}{a}\Pi\right)', \qquad (1.35)\\
&\dot{\Pi} = \frac{1}{r^2}\left(r^2\frac{\alpha}{a}\Phi\right)',\\
&\frac{\alpha'}{\alpha} - \frac{a'}{a} + \frac{1-a^2}{r} = 0,\\
&\frac{a'}{a} + \frac{a^2-1}{2r} - 2\pi r\left(\Pi^2 + \Phi^2\right) = 0,
\end{aligned}$$

and where $\Phi \equiv \phi'$ and $\Pi \equiv a\dot{\phi}/\alpha$ are the auxiliary scalar field variables. In this notation $\phi' = \frac{d\phi}{dr}$ refers to the spatial derivative and $\dot{\phi} = \frac{d\phi}{dt}$ refers to the time derivative.

In such a setup, Choptuik considered one-parameter families of initial data, for example

$$\phi(r) = \phi_0 \tanh[(r - r_0)/\delta], \tag{1.36}$$

where ϕ_0 generally corresponds to the free parameter to choose, but other combinations are possible, for instance, fixing ϕ_0 and r_0 and varying δ. For other choices see Table I in [17]. Usually this parameter is referred to as p, nomenclature that is used from now on. What Choptuik discovered was that regarding the chosen value for p in the initial data, the outcome of the evolution of the Einstein equations was qualitatively different. When choosing weak initial data ($p < p_\star$), the scalar field would end up dispersing to infinity, i.e. leaving flat space behind. When the initial data was strong enough ($p > p_\star$) the scalar field would collapse, forming a BH. The threshold lying in between both regimes is what later became known as the critical solution, which separates both end states and displays some special properties, called critical phenomena.

First, this threshold solution was universal, that is, independent of the initial data family. The solution on the verge of collapse was always the same. See Fig. 1.3 which was taken from [36], for a illustration of

universality. It is clear looking at that figure that when a phase space trajectory starts on a critical surface, it never leaves it. One can say then that the critical surface is an attracting manifold and that the critical point is an attractor of codimension one. As a consequence, universality emerges. When a set of initial data is tuned close to the critical surface, its evolution will happen almost parallel to this surface getting closer and closer to the critical solution, where any imprint from the initial data is gone but for its distance to $p_\star$. The closer p is to $p_\star$ the more the solution approaches the critical solution and the longer it will stay close to it, resembling its characteristics.

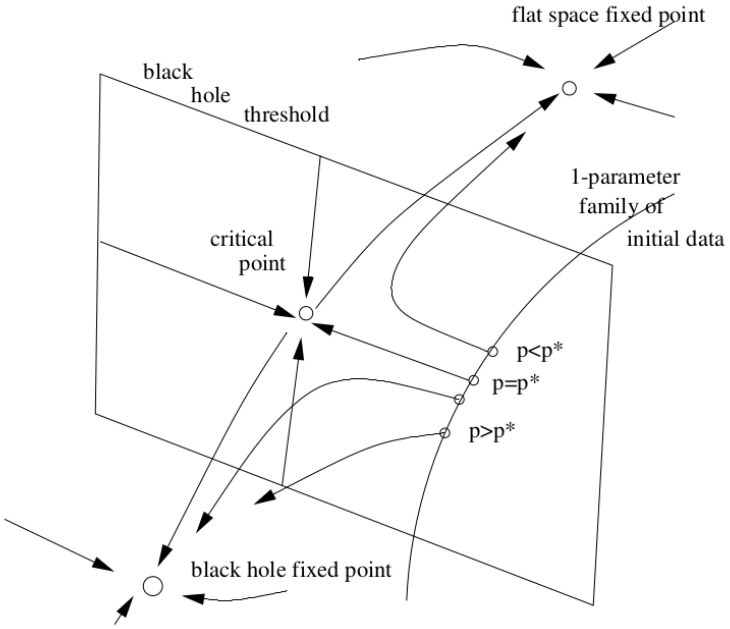

Figure 1.3: The phase space picture for the BH threshold in the presence of a critical point. This image is taken from [36]. In this picture the surface represents the critical solution for $p = p_\star$, the space on the right represents the subcritical regime $p < p_\star$ and the space on the left is the supercritical regime $p > p_\star$. The continuous black line represents an arbitrary one-parameter family of solutions, for which it is possible to choose the value of the parameter p. For any of these lines, $p_\star$ corresponds to the intersection with the critical surface, and any solution that starts tuned to its respective $p_\star$ will end up in the critical solution. It is also shown that when close to criticality (in both regimes) the solutions get very proximate to the critical solution, following its behavior for a finite amount of time.

Second, the main geometric feature of this critical solution is what Choptuik reported as *echoing*, meaning that the critical solution is scale-invariant, or self-similar. Such a symmetry can be Discrete Self-Similar (DSS), as in Choptuik's example, or Continuous Self-Similar

(CSS). A spacetime is said to be CSS if there is a homothetic vector field ξ

$$\mathcal{L}_\xi g_{\mu\nu} = 2g_{\mu\nu}. \tag{1.37}$$

Consequently, in a CSS spacetime, in coordinates adapted to the symmetry $x^\mu = (\tau, x^i)$ the vector field $\xi = -\frac{\partial}{\partial_\tau}$ and the metric coefficients have the form

$$g_{\mu\nu}(\tau, x^i) = e^{-2\tau}\tilde{g}_{\mu\nu}(x^i). \tag{1.38}$$

In the case of a DSS spacetime the definition from Eq. 1.38 can be adapted as

$$g_{\mu\nu}(\tau, x^i) = e^{-2\tau}\tilde{g}_{\mu\nu}(\tau, x^i), \tag{1.39}$$

where $g_{\mu\nu}(\tau, x^i)$ is periodic in τ with period Δ. A more extended explanation about CSS and DSS is given in Section 2.1. This Δ is usually referred as echoing period and in Choptuik's case it experimentally takes the value $\Delta \simeq 3.44$. This echoing period is universal and only depends on the matter model, at least, in the spherically symmetric case.

Third and last, there are some quantities, in this example, the mass of the created BH (which serves as order parameter), that scale for $p > p_\star$ as a power-law of the form

$$M \simeq |p - p_\star|^\gamma, \tag{1.40}$$

where p is the free parameter of the family of initial data, $p_\star$ is the critical value, M is the mass of the BH and γ is the critical exponent, that is universal and experimentally takes a value of $\gamma \simeq 0.37$. This means that a BH arbitrarily small can be formed. However, this power-law behavior also applies to other gravitational quantities, as it was also proven by [37] that in the subcritical regime ($p < p_\star$) the maximum of the curvature scalar R also follows such a relation, but with a scaling exponent of -2γ. In other words, close to the verge of collapse, the dimensionful quantities that have a measure of length scale as a power-law with exponent γ, which is universal and only depends on the matter model. This applies as well to the Kretschmann scalar ($I = R_{abcd}R^{abcd}$), which, as it was explained in Section 1.1, will be the relevant curvature scalar in the vacuum setups as in Chapters 3 and 4, for which the corresponding scaling relation holds as

$$I_{max}^{-1/4} \simeq (p - p_\star)^\gamma. \tag{1.41}$$

Moreover, if the critical spacetime is DSS such power-laws should have a superimposed periodic wiggle.

As Choptuik, Chmaj and Bizon [38] introduced when studying the collapse of a Yang-Mills field, critical phenomena in gravitational

collapse can be classified as type I or type II. They might also be found in the literature as Type I and Type II transitions or Type I and Type II behavior. This classification has some similarities with the statistical mechanics classification of first and second order phase transitions, but they are not a perfect analogy.

- **Type I:**

  In statistical mechanics, in a first order phase transition the order parameter has a finite discontinuity. In type I critical phenomena the mass of the BH turns on at a finite value (see Fig. 1.4). This means that there is a minimum, non-zero BH mass which is in some sense universal, as it does not depend on the initial data. As it is not possible to have arbitrarily light BHs, this discontinuity in the mass has a parallelism with the discontinuity of the order parameter in the first order phase transitions in statistical mechanics. First order phase transitions do not show critical behavior in statistical mechanics, in contrast, in Type I gravitational collapse critical features appear and the diagram from Fig. 1.3 still applies. In this case the critical solution is stationary or time-periodic and can be described by a continuous or discrete symmetry (analogous do DSS and CSS). The dimensionful quantity that follows a power-law behavior and plays the role of an order parameter is the lifetime t_p that a given solution is close to the critical solution [35, 39]

  $$t_p \simeq -\frac{1}{\lambda_0} \ln |p - p_\star|. \tag{1.42}$$

  Type I critical phenomena happen when a mass scale becomes dynamically relevant in the field equations, see for example the massive scalar field [40], the Yang-Mills field [38] or the driven Neutron Star collapse [41].

- **Type II:** Second order phase transitions in statistical mechanics are also called continuous, due to the absence of a finite discontinuity in the order parameter. In type II critical phenomena the mass of the formed BH follows a power-law of the form Eq. 1.40, which implies that arbitrary light BH can be created. In contrast with Type I critical phenomena, the mass of the BH does not have a "jump", it is rather continuous as the order parameter is continuous as well in the second order phase transitions from statistical mechanics. Type II critical phenomena are also characterized by having a critical solution that is either CSS or DSS (see Section 2.1 for more details about this type of scale-invariance). Examples of type II critical phenomena are the massless scalar field [17] in spherical symmetry which shows DSS and the critical solution of a perfect fluid [42] in spherical symmetry which shows CSS.

There are some systems, such as the massive scalar field [40], that might display both Type I and Type II behavior. This seems to depend on the ratio of the length scale of the initial data to the length scale of the mass of the scalar field. For a summary of the type of critical phenomena in gravitational collapse in spherical symmetry for different matter models see Table I in [36], but in this work the focus will exclusively be on Type II critical phenomena.

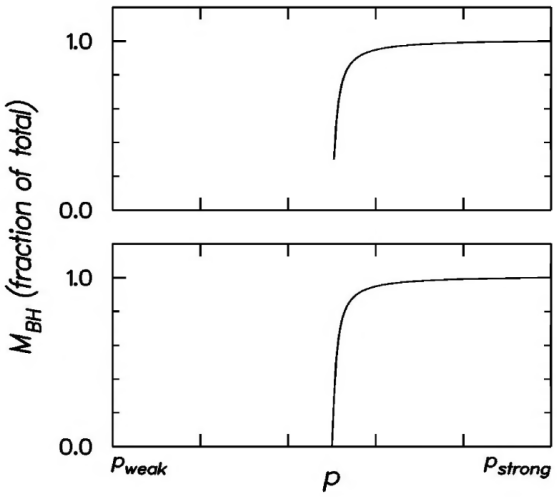

Figure 1.4: Figure 2 from [43]. This image shows the schematic behavior of the mass of the formed BH for critical phenomena. In the top panel, there is a type I transition where the mass of the BH, M_{BH} does not vanish at the threshold. In contrast, in the bottom panel, a type II critical phenomena behavior for the mass of the BH is shown, where M_{BH} gets infinitesimally close to zero at the critical point.

Choptuik's discovery was the first scenario in which critical phenomena in gravitational collapse were reported, opening the door to a new field of study within NR. As it was said, in this thesis the focus will be only on type II critical phenomena. This type of critical phenomena is the one appearing in the Choptuik spacetime and also in the collapse of GWs in vacuum, relevant cases for the Strong and Weak Cosmic Censorship conjectures (see Section 1.4). It is important to remark, nevertheless, that most of the theory about critical phenomena in gravitational collapse comes from studies carried out in spherical symmetry (with the massless scalar field or other matter models), being just a (growing) handful of studies moving beyond. This field of research has substantially changed in recent years (the past four or five years in particular), while the research that is contained in this manuscript was ongoing. In Section 1.5 a historical and chronological recapitulation of critical phenomena in gravitational collapse is done, citing the most relevant works and explaining why this last period had important contributions (including this document and related

work) that motivate a change in the paradigm of critical phenomena in the gravitational collapse.

1.3.2 *Analogy with other systems*

The critical phase transitions in other fields of physics, such as statistical mechanics, share the same properties as in the spherically symmetric gravitational collapse case: fine-tuning, universality, scale-invariant physics, and power-law behavior of the order parameter with universal scaling exponent. As will be mentioned in Section 1.4, this is an important motivation to study critical phenomena in gravitational collapse as part of the theory of critical phase transitions. For the analogy in this manuscript let us just consider two common and well understood cases: the liquid-gas transition in a fluid and the ferromagnetic phase transition as two examples to state the similarities with critical phenomena in gravitational collapse. For a textbook treatment of critical phenomena in statistical mechanics see [44–46].

In thermodynamics, phase transitions are thresholds in the space of external forces at which the macroscopic observables, or one of their derivatives, change discontinuously. For instance, the difference in densities in the liquid and gas phases depends on the temperature as a power-law with a critical exponent γ as follows

$$\rho_{\text{liquid}} - \rho_{\text{gas}} \simeq (T_\star - T)^\gamma, \tag{1.43}$$

which is obviously reminiscent of the power-law from Eq. 1.40. A priori, when crossing the boiling curve (see Fig. 1.5) the density of the fluid changes discontinuously from liquid to gas, however, this difference depends on the temperature according to Eq. 1.43. When the temperature reaches criticality, this difference vanishes and it is possible to change phase continuously. This critical point is defined as the end of the liquid-gas equilibrium curve.

A very similar feature is found in Ising ferromagnets. At high temperatures ($T > T_\star$) and null external magnetic field $\mathbf{B} = 0$ the system is in the paramagnetic phase, that is, there is not an overall magnetization $|\mathbf{m}| = 0$. However, for low temperatures ($T < T_\star$), the spins tend to align along a specific direction, even in the absence of an external magnetic field, therefore the magnetization is not null $|\mathbf{m}| \neq 0$ and the system is in the ferromagnetic phase. This behavior is characterized by the power-law

$$|\mathbf{m}| \simeq (T_\star - T)^\gamma, \tag{1.44}$$

where $T_\star$ is the Curie temperature and γ is the critical exponent. Again, a power-law like Eq. 1.40 is present. By looking at Fig. 1.6 it is clear that there are two phases. When applying an external magnetic field, below the critical temperature the spontaneous magnetization changes discontinuously. However, above the critical temperature the magnetization change it is continuous.

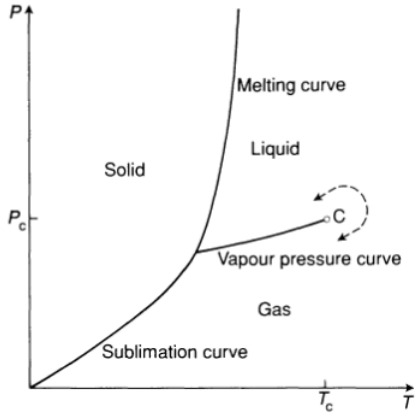

Figure 1.5: Phase diagram of a fluid (from Fig. 1.1 of [44]). In this case all the phase transitions are first order except at the critical point C, beyond which it is possible to move continuously from liquid to gas.

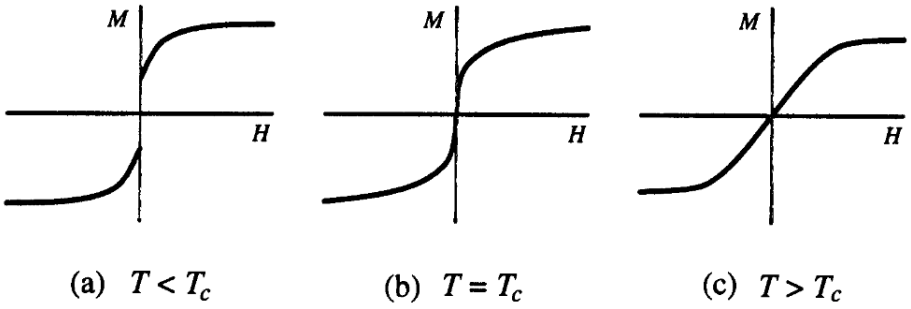

Figure 1.6: This corresponds to Fig. 1.2 in [45]. M corresponds to the magnetization, H to the external magnetic field applied, T to the temperature, and T_c to the critical temperature or Curie temperature. (a) corresponds to the ferromagnetic phase, where the spins align with the applied magnetic field in a discontinuous manner, revealing a first order phase transition. (b) corresponds to the critical point, at which the first order phase transition becomes continuous and the correlation length diverges. (c) corresponds to the paramagnetic regime where the magnetization aligns continuously (second order phase transition) with the external magnetic field.

1.4 MOTIVATION

The main motivation to study critical phenomena in gravitational collapse comes from both, the strong (SCC) and the weak cosmic censorship (WCC) conjectures [47, 48]. They are of great concern in classical 3+1 gravity, therefore a way to try to find counterexamples to them is to use NR to study extreme spacetimes.

The WCC conjecture is usually stated as

Generic asymptotically flat initial data have a maximal future development possessing a complete future null infinity.

Maximal future development here is meant in the sense that any other future development is contained in the maximal development [5].

WCC, in other words means that no naked singularities might be seen from future null infinity. A priori this would be in contradiction with the findings by Choptuik [17] that were explained in the section right above, where for the critical solution a naked singularity appears. Although this might be a counterexample to the WCC, it is not considered a conclusive example due to the fine tuning that is needed to achieve the critical solution. As the conjecture is stated for *generic* data, it means that an open set of initial data that has a zero probability measure (as is the case of the critical solution), is not in contradiction with such a statement.

On the other hand, the SCC conjecture is normally expressed as

Generic asymptotically flat initial data have a maximal future development which is locally inextendible as a Lorentzian manifold in a continuous manner.

Where the continuity requirement on the extension refers to the metric. This can be thought of as for generic initial data, the solution, when maximally extended, is unique. This obviously has to do with the regularity of the solution (see [48] for more details), because when maximally extended *something* has to go wrong such that the solution can not be extended. However, if in the case of critical phenomena the critical solution remains regular enough it might be the case that for an open set of asymptotically flat initial data the solution is extendible beyond the blowup by choosing fresh data in the singular surface in inequivalent manners, which would violate the SCC. It might even happen that this scenario is the case for a large set of solutions in, let us say, the collapse of GWs in vacuum, that is close enough to criticality so that the violation of the SCC would happen in an open set of data. Therefore, the violation of SCC would be *honest*. A further discussion on this topic might be found in Section 2.5.2, nevertheless,

this is an essential point on why one might study critical phenomena in gravitational collapse.

After all, it can not be ignored that the study of the most extreme spacetimes within GR is part of its completeness. On the other hand, phase transitions are very well understood in other systems such as statistical mechanics, thermodynamics, or magnetism, therefore it is a *must* to also find the right significance they have within the gravitational context by focusing on the threshold between collapse and dispersion and comprehending its peculiarities.

1.5 HISTORY OF CRITICAL PHENOMENA IN GRAVITATIONAL COLLAPSE

As is well known and was discussed above, critical phenomena in gravitational collapse discovered by Choptuik in 1993 [17] were a breakthrough in the field of NR. Since then numerous authors have studied such phenomenology in different systems with different symmetry restrictions, however, Choptuik's work was pioneering, setting the discovery of critical phenomena for a massless scalar field in spherical symmetry. The critical exponent for the scaling of the masses of the BHs in this case resulted $\gamma \simeq 0.37$. Critical phenomena in the spherical case are well known, therefore, studying the collapse of GWs in vacuum becomes more interesting. If one wants to understand critical phenomena in GWs, one should go beyond spherical symmetry since any spherically symmetric solution will not represent GWs. The first work investigating such a setting was done by Abrahams and Evans already in 1993 [49], where they evolved a single one-parameter family of Teukolsky waves (see Chapter 3) and report a critical exponent of $\gamma \simeq 0.37$ as well for the scaling of the mass of the BHs, and $\Delta \simeq 0.6$ for the echoing period. Soon after a second study [50] by the same authors came, where they investigated a second family of Teukolsky data where this time they found a critical exponent of $\gamma \simeq 0.36$, compatible with the previous result, leading to the conclusion that the critical exponent was universal and the same as in the pioneering work of Choptuik for the massless scalar field. These two studies were the first ones to report an axisymmetric critical solution, since there are no spherical dynamical GWs. The picture of critical phenomena remained the same so far, a self-similar critical solution that lies on the verge between dispersion and BH formation that acts as an attractor and it is universal, displaying as well a universal critical exponent and echoing period. Since then many other authors evolved GWs trying to look for critical phenomena, however, nobody was able to reproduce such results so far. In Table 1.1 there is a summary of the attempts to evolve GW in vacuum from the '90s until nowadays. In part, an explanation might be that most authors tried to evolve Brill waves (see Chapter 3) instead of Teukolsky due to the fact that they are much simple to

obtain as initial data and, as the features of critical collapse shall not depend on the family of the initial data, there is, a priori, no conflict. It was not until [51] in 2021 that critical phenomena were studied with a Teukolsky family again.

Authors	Year	Data type	References	Comments
Abrahams & Evans	1993	Teukolsky	[49, 50]	critical behavior
Alcubierre *et.al.*	2000	Brill	[52]	
Garfinkle & Duncan	2001	Brill	[53]	
Santamaria	2006	Brill	[54]	
Rinne	2008	Brill	[55]	
Sorkin	2011	Brill	[56]	critical behavior*
Hilditch *et.al.*	2013	Brill & Teukolsky	[57]	
Hilditch *et.al.*	2017	Brill	[58]	critical behavior
Khirnov & Ledvinka	2018	Brill	[59]	
Ledvinka & Khirnov	2021	Brill & Teukolsky	[51]	critical behavior
Suárez *et.al.*	2022	Brill	[60]	critical behavior

Table 1.1: Summary of published results on numerical simulations of nonlinear waves. In the case of [56] it was shown by posterior studies that what the author reported as critical behavior was not fully trustable.

Focusing again on the spherically symmetric cases and in the massless scalar field, in 1998 Garfinkle and Duncan came up with a work [37] in which the power-law scaling was also happening for the maximum of the curvature scalar in the subcritical regime (in addition to the mass of the BHs in the supercritical one). This time, the critical exponent corresponds to -2γ, as the curvature scalar has units of inverse length square. This allows one to study the universal scaling approaching the critical point from both sides, that is, from the subcritical regime as well as from the supercritical one.

The first attempt to understand the critical collapse of a massless scalar field beyond spherical symmetry was performed in 1999 by Martín-García and Gundlach [61] by perturbative analysis of the spherical solution. In this work, the authors study nonspherical linear perturbations of Choptuik's solution. They found that all nonspherical perturbations of the Choptuik's spacetime decay, however, the mode corresponding to $\ell = 2$ had the slowest damping, and that there is a single pure spherical mode that grows, which causes collapse or dispersion. This result will be, somehow, contradicted in the future, see Table 1.2 for a summary of the published results beyond spherical symmetry, but let us proceed with the facts in order.

After Martín-García and Gundlach, the first numerical study beyond spherical symmetry for the massless scalar field came out in 2003 by

Authors	Year	References	Comments
Martín-García & Gundlach	1999	[61]	
Choptuik *et. al.*	2003	[62]	two centers of collapse
Healy & Laguna	2014	[63]	
Deppe *et. al.*	2019	[64]	
Baumgarte	2019	[65]	two centers of collapse

Table 1.2: Summary of published results on studies beyond spherical symmetry for the critical gravitational collapse of the massless scalar field.

Choptuik *et. al.* [62], where the authors studied the collapse of a massless scalar field in axisymmetry. The authors adopted a two-parameter family of initial data parametrized by η as the overall strength which was tuned to criticality, and ϵ for the deviation from spherical symmetry. In this work, the authors report that the critical solution might be considered as the spherically symmetric one but with axisymmetric perturbations. In other words, they found that both, the critical exponent γ and the echoing period Δ decrease when increasing ϵ, the parameter measuring departure from sphericity. A second important result from this study was that for large values of ϵ and fine tuning to criticality, the collapsing region bifurcates into two collapsing centers along the symmetry axis, which suggest a nonspherical growing mode dominating the evolution, in apparent contradiction with Martín-García and Gundlach [61]. The authors also speculate that despite the insufficient resolution in their numerical simulations, this bifurcation would occur indefinitely, making the critical solution much more complex and interesting than was initially thought. As one will see further in this manuscript, such a bifurcation behavior is found for other setups as it is described in Section 4.3.2 for the collapse of GWs in vacuum, however, this was the very first time such a feature was reported.

Following the study of scalar fields in axisymmetry, the next year, in 2004, the same authors, Choptuik *et. al.* [66] published a study describing the critical collapse of a complex (rather than real) scalar field with angular momentum, again, an axisymmetric setup. This time the authors find a DSS critical solution that is universal modulo a family dependent phase. It was also found that the angular momentum was not much relevant for the critical behavior and it turned out that it did not scale as a pure power-law. This was the second non spherically symmetric critical solution after Abrahams and Evans and the collapse of GWs in vacuum [49]. The authors take this fact as a positive outcome, where they even state that

"[...] the phase space has a more intricate structure than one might have naively imagined, probably containing an infinite set of distinct intermediate attractors characterized by their behavior near the center of symmetry".

This was the second indication, together with [62] that when going beyond spherical symmetry a more complex threshold solution might arise.

In the meantime, other authors [52–55] evolved non-linear GWs as summarized in Table 1.1, but the case of Sorkin in 2011 [56] deserves special attention. This was the first work after Abrahams and Evans [49] that successfully evolved non-linear GWs and reported critical behavior. The initial data chosen by Sorkin were centered prolate Brill waves, a popular choice also in the previous evolutions of Brill waves (see Table 1.1). In this work, Sorkin reports the finding of a different critical solution from the one found by Abrahams and Evans [49]. In this case, the blowup of the curvature occurs in concentric rings in the equatorial plane centered on the symmetry axis rather than pointwise (see Section 2.3.7 for a similar solution in a toy model). However, regarding the power-law, Sorkin reports that the maximum curvature scales as a power-law and that the scaling exponent for all the studied families lies in a range of $\gamma \in [0.38, 0.4]$, which is compatible both with Abrahams and Evans [49] and Choptuik [17]. This result was very exciting as it could lead to a change in the understanding of the universality of critical solutions. However, in previous studies the regime in which the critical amplitude should lie was reported below the limit given by Sorkin, and finally, in 2017, it was found by Hilditch *et. al.* [58] that the regime that Sorkin was studying as subcritical was in fact supercritical as they had better numerical results to bound the critical amplitude. More details about this work are given below. Unfortunately, this means that despite the excitement there exists subsequent work that contradicts the result of the work done by Sorkin.

It is worth commenting that before Hilditch *et. al.* [58] there was an earlier attempt to study critical collapse evolving non-linear GWs in moving-puncture coordinates in 2013 [57]. In this work the authors do not study critical phenomena due to the lack of accuracy of their numerical simulations, however, they attempt to evolve both Brill and Teukolsky waves, noticing that the latter have improved numerical behavior. This fact will be relevant further in this manuscript as there are some differences between these two types of initial data that might explain some discrepancies in the behavior near the critical regime (see Chapter 3).

Moreover about the same time, in 2014 the work by Healy and Laguna [63] about the critical collapse of scalar fields beyond axisymmetry was a second attempt to study numerically the massless scalar field in a setup different than spherical symmetry. This time the au-

thors study deviations from the spherical solution with a parametrized addition of the spherical harmonic $Y_{21}(\theta, \phi)$, finding that the mass of the BHs scales as a power-law with the critical exponent of $\gamma \approx 0.37$, as in the spherical case, independently of the amount of the spherical harmonic of the initial data. So far, the authors give evidence of one single spherical unstable mode and they find difficulty in reporting echoing, however, they argue that the tuning to the critical amplitude could be better, as they are still far from the threshold. This result is in agreement with the theoretical findings by Martín-García and Gundlach [61] and, as it is not as close as Choptuik *et. al.* [62] to criticality, it is not in contradiction.

Let us now focus on Hilditch *et. al* [58], where the authors evolve centered Brill waves with a pseudospectral method, `bamps`, the same code that has been used (although with updates and the inclusion of Adaptive Mesh Refinement (AMR)) in Chapter 4 of this document. See Section 4.1 and [34] for a detailed description of the code. In this work, the authors find evidence of critical phenomena in the collapse of axisymmetric prolate Brill waves in vacuum, and they can tune the closest to the threshold amplitude so far, designated as $A_\star = 4.6966953125$, giving evidence of the powerful numerical method that is implemented within `bamps`. The authors also rule out the critical amplitude achieved by Sorkin [56] by evolving exactly the same amplitude and finding an (AH), therefore, it *must* be a supercritical amplitude. Nevertheless, right before the AH gets formed, the authors also see that the maximum of the Kretschmann scalar also occurs in equatorial rings centered in the symmetry axis. To classify a set of initial data as supercritical, the authors look for AHs, which are found to bifurcate in parameter space when close to the threshold suggesting that the Brill wave initial data collapse to form a head-on collision of two BHs, however, evidence is still to be determined, but it is a result in agreement with the findings by Choptuik *et. al.* [62]. This study also finds evidence of power-law scaling in the relevant curvature scalar, i. e. the Kretschmann scalar, which behaves like a straight line plus some wiggles where the scaling exponent $\gamma \simeq 0.37$ is compatible with Abrahams and Evans [49], however, they find an echoing period of $\Delta \simeq 3$, which is rather different, suggesting for the first time that the period might depend on the initial data and not only on the matter model. So far the authors were able to show only one period in the scaling of the Kretschmann scalar, therefore speculations on what could happen are open, it might be that the period changes when tuning closer to criticality or that the wiggle even disappears, in either case, it is an indication that the scaling might not be always the same and that more investigation is needed.

Between 2018 and 2019 two interesting publications evolving numerically the massless scalar field beyond spherical symmetry came out. One of them by Deppe *et. al.* [64] carried out evolutions with no

symmetry assumptions with the SpEc code, in full-3d, of the massless scalar field and studied the behavior for different symmetry assumptions close to the threshold of BH formation. The authors report that even with a departure from spherical symmetry the critical solution is always the same as in the spherical case, where the scaling exponent γ is consistent with previous results but the echoing period Δ seems to slightly differ. In this case, the authors do not observe any non spherical growing modes, as Choptuik *et. al.* [62] did, however, it is not clear if the tuning to criticality was sufficient to find such modes. The second work that came out at that time by Baumgarte [65] also studies aspherical deformations of the Choptuik spacetime numerically but restricted to axisymmetry. This time the author evolves axisymmetric sets of initial data and examines the effects of the deviation from sphericity. Baumgarte found that both the scaling exponent γ and the echoing period Δ agree with previous results when the deviation from spherical symmetry is small, however, their values decrease when departing from sphericity, in agreement with Choptuik *et. al.* [62]. The key result of this work is that when studying the spherically symmetric critical solution with nonlinear perturbations the evolution might be described in terms of the effective values of the scaling exponent γ, the echoing period Δ and also the decay rate κ, where the three depend on the departure from spherical symmetry. Baumgarte found that for sufficiently large deviations from spherical symmetry κ decreases and can even change sign, transforming a decaying mode into a growing one, explaining the discrepancy between Martín-García and Gundlach [61] and Choptuik *et. al.* [62]. In summary, when one departs enough from the sphericity there is a non spherical growing mode that in fact leads again to the bifurcation of the spacetime along the symmetry axis with two centers of collapse, above and below the origin.

At this point of the story, there were found at least two models (massless scalar field and GWs in vacuum) that display two centers of collapse when evolving axisymmetric initial data, therefore, investigating other systems that might display such property became relevant. The first study about critical phenomena in gravitational collapse of electromagnetic waves was published by Baumgarte *et. al.* [67] in 2019. The decision to study such a system in axisymmetry makes Maxwell's equations reduce to a wave equation similar to the massless scalar field case and, moreover, this system shares the property with the collapse of GWs in vacuum that none of them have a spherically symmetric solution. This work studies two dipole families of initial data, finding a scaling exponent of $\gamma \simeq 0.145$ for the maximum energy density $\rho \simeq (\eta_\star - \eta)^{-2\gamma}$, and an approximate echoing period of $\Delta \simeq 0.55$, however, the discrete self-similarity of the critical solution and the wiggles in the power-law seems to be only *approximate*, as well as the universality, since two critical solutions seem to be almost the same. The authors speculate that this approximate rather than exact

DSS behavior might be due to the presence of higher order angular multipoles. Soon after, a follow up of this work came out by Mendoza and Baumgarte [68] in 2021, where the authors study critical phenomena in the gravitational collapse of electromagnetic waves for dipole and quadrupole initial data, as a generalization of the above mentioned previous work. This work is one of the breakthroughs regarding critical phenomena in gravitational collapse in recent years, as it was shown that the dipole and the quadrupole initial data lead to different threshold solutions (both qualitative and quantitative). The dipole data (odd) leads to a single collapsing center when on the other hand the quadrupole (even) happens to have two collapsing centers along the symmetry axis, bifurcating the spacetime as it was already been reported previously for the massless scalar field and the GWs in vacuum. One might think that these two solutions can still be locally the same as the bifurcating of the spacetime might be two copies of the dipole solution, however, it is shown in this work by Mendoza and Baumgarte [68] that both the scaling exponent and the average echoing period are different (see their Fig. 7). The authors then speculate that the threshold solution is not universal as it depends on the initial data once spherical symmetry is dropped. This finding is in total agreement with Chapter 2 of this manuscript and [69], where also two different threshold solutions were found in axisymmetry for a toy model that reproduces critical phenomena. The speculation is that different multipoles in the initial data might couple to different parts of the nonlinearities in Einstein's equations, which results in the already explained different behavior of the threshold solution. This work was also the motivation for Chapter 3 of this thesis, where Brill and Teukolsky waves are compared in the linear regime as, a priori, they also correspond to different multipoles.

To complete the historical recapitulation about critical phenomena in gravitational collapse, a discussion of the work by Ledvinka and Khirnov [51] is required, in which the authors study the critical vacuum gravitational collapse using both Teukolsky and Brill waves as initial data. This is the first study using GWs in vacuum that actually studies several families of initial data of different nature. In their conclusions, they explain that they find what happens to be only partially similar to the DSS behavior of the massless scalar field. Despite finding several approximate echoes they do not have a regular delay. The evidence found is that the threshold solution DSS structure might be at most considered *approximate*. This translates as well to the wiggles of the power-law that the maximum of the Kretschmann scalar follows, both the echoing period and the scaling exponent differ and therefore are dependent on the initial data family (see their Fig. 1). As in previous studies, the authors also found a bifurcation of the spacetime along the symmetry axis when tuning to the threshold. The results from Ledvinka and Khirnov are consistent with Chapter 4 of this

manuscript, and both contradict the conclusion made by Abrahams and Evans [49, 50], that both the critical exponent and the echoing period are universal, as well as the DSS nature of the critical solution.

In summary, critical phenomena in gravitational collapse seem to be well understood under the assumption of spherical symmetry where the critical solution displays self-similar behavior, the dimensionful quantities scale as a power-law with universal critical exponent and echoing period, and the critical solution is also unique and independent of the initial data. However, when one departs from spherical symmetry and the studied system does not admit such a spherical solution, the picture becomes more complex. The threshold solution seems to only display *approximate* DSS, in agreement with Chapters 2. The scaling exponent and the echoing period also appear to change and to depend on the specific initial data family, as will be seen in Chapter 4. Finally, the universality of the critical solution, understood as in the spherical setup, changes, since the spacetime shows a bifurcation leading to two centers of collapse. Moreover, it was shown for the toy models [69] and for the electromagnetic waves [68] that actually different threshold solutions exist. For the latest updates within this context please keep reading through this document as we will discuss the state of the art of critical phenomena in gravitational collapse beyond spherical symmetry.

1.6 CONTRIBUTIONS OF THIS MANUSCRIPT

Hereafter, this PhD thesis is divided into two main parts. First of all the study of critical phenomena using toy models [69] corresponding to Chapter 2. In this work a simpler strategy involving modelling is taken rather than investing more computational resources to evolve complicated setups such as GWs in vacuum or electromagnetic waves coupled to gravity. Let us think about some relatively simple nonlinear models that resemble the principal part of GR, reproduce the standard picture of critical phenomena in gravitational collapse in spherical symmetry, and that one can study beyond. In this Chapter, five models with these characteristics are presented, where some of them allow analytical solutions and some of them are studied numerically with a code that I personally wrote from scratch for the occasion, that allows evolution in spherical symmetry. This was the very first time, up to my knowledge, that a simple model with just one single scalar field could reproduce the critical phenomena scenario. This result was an important contribution in recent years to our theoretical understanding of why critical phenomena seem to be more subtle once spherical symmetry is out of the game.

In the second part of this manuscript, which has two chapters, the focus is on GWs in vacuum. In Chapter 3 a comparison in the linear regime between Brill and Teukolsky waves is carried out. The motiva-

tion for such an investigation is that many authors have reported that evolving Brill waves seem more challenging than Teukolsky waves, with a priori, no conjectures explaining this difference. Moreover, under the light of [51], it seems that having different sets of initial data matters regarding the scaling exponent and echoing period in the critical collapse of GWs in vacuum, adding more interest to studying the differences between Brill and Teukolsky waves. Finally, [68] gave the hypothesis that was missing: different multipoles on the initial data might lead to different, at least globally, threshold solutions in the case of critical collapse with electromagnetic waves. Teukolsky waves are quadrupolar by construction, however, Brill waves are multipolar, but the findings by [70], corresponding to Chapter 3, show that the most common choice of the Brill data is also quadrupolar and that at least in the linear regime there are not enough discrepancies between both types of initial data that can explain the different behavior during evolution.

The second Chapter of the second part, about GWs investigates more deeply critical phenomena in GWs in vacuum using the adaptive pseudospectral code `bamps` [34], which includes AMR. More details about this implementation can be found in the forthcoming PhD thesis of Sarah Renkhoff [71]. In this work, six different families of Brill waves are evolved and tuned to the verge of BH formation. The findings for these different families are totally consistent with [58] and [51]. For the centered Brill wave families, the previous results were reproduced, meanwhile, the off-centered families bring again the two key results: evidence of different scaling exponents and echoing period for the different families of initial data, and bifurcation of the spacetime, finding disjoint AHs for supercritical sets of data close to the threshold. In this work it was difficult to claim exact DSS behavior of the threshold solution. It was not possible to claim DSS, both for the threshold solution and for the wiggles in the power-law of the maximum of the Kretschmann scalar. It is clear that more research is needed since there are not enough periods for all families yet and some doors are still open, however, this contribution is another key result that confirms that in the real setting of the collapse of GWs in vacuum, which does not admit a spherically symmetric solution, the scheme gets more complicated.

Finally, a final statement and the conclusions are gathered in 5.

Part I

MODEL FOR CRITICAL COLLAPSE

2

SEMILINEAR WAVE MODEL FOR CRITICAL COLLAPSE

The weak and strong cosmic censorship conjectures are of great importance in classical 3+1 dimensional gravity. The first of them can be informally stated as given generic asymptotically flat initial data, the resulting solution will exist globally outside a BH region [47], [48]. The latter is likewise the conjecture of uniqueness of solutions coming from generic initial data, and it is directly related to regularity of solutions at blowup. Despite their important meaning and significance, both are conjectures. A way to deal with the lack of a global proof is to try to find counterexamples using, for instance, NR. There is the hope that, within the picture of critical phenomena in gravitational critical collapse, giving evidence that an open set of initial data do not have complete BH exteriors, or are regular enough at the blowup such that they might be extended non uniquely, might be possible.

The strategy within NR is to try to construct such extreme spacetime is the following: consider a one-parameter family of initial data such that small values of the (strength) parameter result in data close to flat space, with larger values being more and more deformed. Then tune that strength parameter to the threshold of BH formation. Starting with the pioneering work of Choptuik [17], as seen in Section 1.3.1, studies along these lines in spherical symmetry revealed behavior which has since come to be known as critical phenomena in gravitational collapse. In short, it has been found that for a given family there is, in a sense, a single solution lying between dispersion and collapse to form a BH. Numerical evidence suggests that these solutions have naked singularities. However, these naked singularities are not considered counterexamples to the cosmic censorship conjectures due to the high fine tuning of the initial data that is needed to exactly evolve the critical solution. These threshold solutions are captivating as they show the features of the called critical phenomena. Empirically, these solutions are either continuously (CSS) or discretely (DSS) self-similar and, for a given model, seem to be unique (in the sense that all families of initial data display the same threshold solution, i.e. the critical solution). As a consequence, when considered as a function of the strength parameter, solutions naturally engender a power-law behavior near the threshold. Some examples, in spherical symmetry, are [72, 73] and [37], where

the critical solution is DSS and the maximum of any nonvanishing curvature scalar represented as a function of the distance from the threshold in phase space, exhibits a power-law with a superposed periodic wiggle.

Beyond spherical symmetry, the picture gets more complicated (see Section 1.5). Similar behavior was found, although with features that have yet to be explained. For instance, in [67] and in [68] the authors study the gravitational collapse of electromagnetic waves, where the threshold solutions seem to only be *approximately* self-similar. Studying dynamic systems that display critical phenomena in gravitational collapse beyond spherical symmetry is complicated and computationally expensive (see for example the collapse of GWs in vacuum from Chapter 4), hence, it is worth looking for an easier and computationally cheaper option to rigorously understand what happens with the critical phenomena once spherical symmetry is out of the game. To walk in this direction it is then desirable to construct *maximally* simple models that capture the qualitative behavior of critical phenomena close to the threshold of blowup. Some research has been made [74–78], however, all of these works show continuos rather than discrete self-similarity. Therefore in this Chapter, and from the point of view of nonlinear partial differential equations (PDEs), the aim is to find a simple system that admits small-data global existence, meaning that if the initial data is sufficiently small in some norm (a high derivative version of E^1) then the solution exists as a smooth function for all t, but large data blowup and that has a unique *discretely* self-similar critical solution at the threshold between the two regimes.

Let us illustrate what the next sections of this Chapter will be about. Let us take the system

$$\Box\phi = \nabla_a\phi\nabla^a\phi\,, \tag{2.1}$$

as a model to indicate the structural shape of the terms that generate the self-similar critical solutions, where ∇ is the Levi-Civita derivative compatible with the Mikowski metric η_{ab}, and $\Box$ is the flat space D'Alambertian operator. The main aim of this Chapter is to give such a model, therefore in Section 2.2 several toy models are presented, some of them with analytical solutions and some others for which numerical tools were employed, explaining also in detail how the numerical solutions were computed.

Furthermore, the properties of solutions near blowup are of interest as well as the status of conjectures related to cosmic censorship for spherical symmetry and beyond. All the presented models are of the type of Eq. 2.1 but with different coefficients before the nonlinearity. This means that the principal part is taken to be the D'Alambertian associated with η_{ab}. Please, be aware that, as only semilinear wave models are introduced, there are no notions of trapped surface, nor of a BH formation intrinsic to the model.

2.1 SELF-SIMILAR FUNCTIONS

Solutions to these models either live forever (small-data global existence) or terminate at some finite time (large-data breaking down). There are two ways in which, depending on the model, the blowup happens: either it is just the first derivative that blows up, or it is the field itself that explodes pointwise. Each of them has an analog in L^2-like norms, although they are not equivalent. All the models of Section 2.2 have fine structure at the threshold of blowup which is described by self-similarity, either continuous or discrete, a special case of scale-invariance that will be introduced in more detail in Section 2.1.2. Since there are two types of blowup and two types of self-similarity there must be a relationship between both concepts that are discussed below.

2.1.1 *Definitions and blowup*

Let us start giving some definitions. A function $f(t, x^i)$ is said to be in L^2 at instant t if the integral

$$||f||_{L^2} \equiv \left(\int_{\mathcal{D}[f(t,\cdot)]} \mathrm{d}\Sigma \left| f(t, x^i) \right|^2 \right)^{1/2}, \tag{2.2}$$

exists and it is finite, where $\mathcal{D}[f(t,\cdot)]$ is the domain of $f(t, x^i)$, (T, x^i) are global inertial coordinates on Minkowski and $d\Sigma$ is the natural volume form induced in level sets of t.

Referring to the H^1 norm, a function $f(t, x^i)$ it is said to be H^1 at instant t if the integral

$$||f||_{H^1} \equiv \left(\int_{\mathcal{D}[f(t,\cdot)]} \mathrm{d}\Sigma \left(\left| f(t, x^i) \right|^2 + \sum_i \left| \partial_i f(t, x^i) \right|^2 \right) \right)^{1/2} \tag{2.3}$$

exists and it is finite, where ∂_i denotes the partial derivative $\partial/\partial x^i$. Generalizing these definitions, a function $f(t, x^i)$ is said to be in the Sobolev space H^k at instant t if the norm [79]

$$||f||_{H^k} \equiv \left(\int_{\mathcal{D}[f(t,\cdot)]} \mathrm{d}\Sigma \sum_{|\alpha| \leq k} \left| \partial_i^\alpha f(t, x^i) \right|^2 \right)^{1/2}, \tag{2.4}$$

exists and it is finite, where $\alpha = (\alpha_1, \alpha_2, \alpha_3)$ are non-negative integers, $|\alpha| = \alpha_1 + \alpha_2 + \alpha_3$ and $\partial_i^\alpha f \equiv \partial_x^{\alpha_1} \partial_y^{\alpha_2} \partial_z^{\alpha_3} f$. Please, note that the case $|\alpha| = 0$ refers to no derivatives, so the pure function is applied. Please, note as well that $H^0 \equiv L^2$ and that $k = 1$ corresponds to the definition of H^1 from Eq. 2.3.

As a last definition, a function $f(t, x^i)$ is said to be E^1 at instant t if the integral

$$||f||_{E^1} \equiv \left(\int_{\mathcal{D}[f(t,\cdot)]} \mathrm{d}\Sigma \left(\left| \partial_t f(t, x^i) \right|^2 + \sum_i \left| \partial_i f(t, x^i) \right|^2 \right) \right)^{1/2},$$

exists and it is finite. Let us also explain what is the meaning of what is called "blowup". If a function that is initially H^k (or E^1) fails to fulfill the definition at some instant $t' > t$, it is said that it blows up in H^k (or E^1) at that instant t'. Please note that if a function blows up in H^k it will also do so for any $H^{k'}$ for $k' > k$.

The formulation of the WCC conjecture [48] is given in terms of the local L^2 norm integrability of the connection coefficients. Intuitively, if any blowup happens, it might be directly associated with at least one derivative of the metric, and therefore, the connection appears naturally. As it would be the first derivative of the metric blowing up, the modelling interest relies on the semilinear wave equations with blowup in E^1 rather than in L^2.

2.1.2 *Self-similar functions*

Self-similarity means invariance under specific scale transformations, however, let us properly define it. In this case, two types of self-similarity will be considered: continuos (CSS) and discrete (DSS).

A scalar function f is said to be CSS if there exists a coordinate system (t, x^i) and a $\nu \in \mathbb{R}$ such that

$$f(\lambda t, \lambda x^i) = \lambda^\nu f(t, x^i)\,, \tag{2.5}$$

for any $\lambda > 0$. Please note that the chosen coordinates are such the center of the symmetry is the origin. Homegeneous functions of degree ν are a particular case of CSS for when ν is an integer.

A scalar function f is said to be DSS if there exists coordinate system (t, x^i), a $\nu \in \mathbb{R}$, and *some* $\Delta > 0$ such that (2.5) holds for $\lambda = e^{-m\Delta}$, with any $m \in \mathbb{Z}$. Thus, DSS functions have a fractal-type behavior under scale transformations. The condition (2.5) is often expressed in *similarity coordinates* $(T, X^i) = (-\log|t|, x^i/t)$ as

$$f(T + \tau, X^i) = e^{-\nu\tau} f(T, X^i)\,, \tag{2.6}$$

where $\tau = -\log\lambda$. In the case of DSS functions the last condition is satisfied for $\tau = m\Delta$.

2.1.3 *Self-similarity and blowup*

Self-similar functions exhibit particular examples of blowup, either pointwise or under some integral norm. To show this let us integrate Eq. 2.5 in the following way

$$\int_{\mathbb{R}^3} \mathrm{d}\Sigma \sum_{|\alpha|=k} \left|\partial_i^\alpha f(t, x^i)\right|^2 = \frac{1}{\lambda^{2(\nu-k)}} \int_{\mathbb{R}^3} \mathrm{d}\Sigma \sum_{|\alpha|=k} \left|\partial_i^\alpha f(\lambda t, \lambda x^i)\right|^2, \tag{2.7}$$

now, carrying out a change of variables such that $\tilde{x} = \lambda x$, $\tilde{y} = \lambda y$, $\tilde{z} = \lambda z$ and therefore $d\tilde{\Sigma} = \lambda^3 d\Sigma$

$$\int_{\mathbb{R}^3} \mathrm{d}\Sigma \sum_{|\alpha|=k} \left|\partial_i^\alpha f(t, x^i)\right|^2 = \lambda^{2(\nu-k+3/2)} \int_{\mathbb{R}^3} \mathrm{d}\tilde{\Sigma} \sum_{|\alpha|=k} \left|\partial_i^\alpha f(\lambda t, \tilde{x}^i)\right|^2 . \tag{2.8}$$

As inside an integral, it is possible to name the integration variables as one please, it is clear that a CSS function satisfying Eq. 2.5 also satisfies

$$\int_{\mathbb{R}^3} \mathrm{d}\Sigma \sum_{|\alpha|=k} \left|\partial_i^\alpha f(t, x^i)\right|^2 = \frac{1}{\lambda^{2(\nu-k+3/2)}} \int_{\mathbb{R}^3} \mathrm{d}\Sigma \sum_{|\alpha|=k} \left|\partial_i^\alpha f(\lambda t, x^i)\right|^2 , \tag{2.9}$$

for any λ, where x^i are the canonical Cartesian coordinates and the domain of f is $\mathbb{R}^3$, except (possibly) a set of zero measure.

Now, making the particular choice of $\lambda = 1/|t|$, for $t < 0$

$$\int_{\mathbb{R}^3} \mathrm{d}\Sigma \sum_{|\alpha|=k} \left|\partial_i^\alpha f(t, x^i)\right|^2 = \frac{1}{|t|^{2(k-\nu-3/2)}} \int_{\mathbb{R}^3} \mathrm{d}\Sigma \sum_{|\alpha|=k} \left|\partial_i^\alpha f(-1, x^i)\right|^2 . \tag{2.10}$$

Therefore, a nontrivial CSS function with $\nu \leqslant -3/2 + k$ cannot be in H^k for all times because if this function is considered H^k at a certain instant of time $t < 0$, it blows up at $t = 0$. The analogous argument goes through in the case of a CSS function in E^1, where it also blows up at $t = 0$ if the nontrivial CSS function with $\nu \leqslant -1/2$ is in E^1 at $t < 0$.

A CSS function must satisfy

$$\begin{aligned} \partial_t^\alpha f(t, x^i) &= \frac{1}{\lambda^{\nu-k}} \partial_{\lambda t}^\alpha f(\lambda t, \lambda x^i) , \qquad |\alpha| = k , \\ \partial_{x^i}^\alpha f(t, x^i) &= \frac{1}{\lambda^{\nu-k}} \partial_{\lambda x^i}^\alpha f(\lambda t, \lambda x^i) , \qquad |\alpha| = k , \end{aligned} \tag{2.11}$$

for any λ. Making again the choice $\lambda = 1/|t|$, the CSS function satisfies

$$\begin{aligned} \partial_t^\alpha f(t, x^i) &= \frac{1}{|t|^{k-\nu}} \partial_{\lambda t}^\alpha f(\lambda t, \lambda x^i)_{|(-1, x^i/|t|)} , \quad |\alpha| = k , \\ \partial_{x^i}^\alpha f(t, x^i) &= \frac{1}{|t|^{k-\nu}} \partial_{\lambda x^i}^\alpha f(\lambda t, \lambda x^i)_{|(-1, x^i/|t|)} , \quad |\alpha| = k . \end{aligned} \tag{2.12}$$

It is easy to see that a CSS function with $\nu < k$ will not be in C_b^k (fucntions with k-derivatives bounded). It the CSS function is at C_b^k at a certain time $t < 0$, it will blow up at $t = 0$.

In the case of DSS functions, the both arguments above can be extended. Take a nontrivial DSS function with the same bounds on ν and take the limit $t \to 0^-$ trhough a sequence $t_m = -1/\lambda_m = -e^{-m\Delta}$, then, the DSS function will satisfy Eq. 2.9 and Eq. 2.11 for a discrete set of values λ. The results on the bounds of ν and the blowup on the respective norms for both CSS and DSS functions are summarized in Table. 2.1.

H^k	E^1	C^k_b
$\nu \leq -3/2 + k$	$\nu \leq -1/2$	$\nu < k$

Table 2.1: A CSS or DSS function with degree ν (see Eq. 2.5) must blow up in a given function norm (first line) if the associated condition in ν (second line) is satisfied.

2.1.4 *Sobolev embedding*

It can be shown (see for details Theorem 6.5 in [79]) that, for each k a non-negative integer and $s > k + 3/2$, there is a constant c such that

$$||f||_{C^k_b} \leq c\, ||f||_{H^s}\,, \tag{2.13}$$

with f an arbitrary function. In particular, for $k = 0$ and $s = 2$,

$$||f||_{C^0_b} \leq c\, ||f||_{H^2}\,. \tag{2.14}$$

This implies that if a function blows up in C^0_b, it also blows up in H^2. Since the C^0_b-norm is equal to the L^∞-norm, if a function blows up in L^∞ it also blows up in H^2.

2.2 MODEL EQUATIONS

In this Section the used models are presented. It is shown a simple method to generate nonlinear wave equations with an analytical solution, that can be stated in terms of partial waves. Note, however, that not all the presented models respond to this procedure and have analytical solutions, in those cases the numerical method of Section 2.4.1 is applied.

2.2.1 *The wave equation and partial wave solutions*

Let (r, θ^A) be spherical polar coordinates built from x^i in the usual manner. In these coordinates the flat-space wave equation is,

$$\Box\varphi \equiv -\partial_t^2\varphi + \partial_r^2\varphi + \tfrac{2}{r}\partial_r\varphi + \not{\Delta}\varphi = 0\,, \tag{2.15}$$

with $\not{\Delta}$ the standard Laplacian on the round two-sphere of area radius r. Then, the general solution might be written in terms of the partial waves $\varphi_{\ell m}(t, r)$, where the full solution is constructed as

$$\varphi = \sum_{\ell=0}^{\infty} \sum_{m=-\ell}^{\ell} \varphi_{\ell m}(t, r) Y_{\ell m}(\theta^A)\,, \tag{2.16}$$

where $Y_{\ell m}$ are the standard spherical harmonics. Each partial wave has an associated equation

$$-\partial_t^2\varphi_{\ell m} + \partial_r^2\varphi_{\ell m} + \tfrac{2}{r}\partial_r\varphi_{\ell m} - \tfrac{\ell(\ell+1)}{r^2}\varphi_{\ell m} = 0\,, \tag{2.17}$$

whose solution may be written, independently of m, as [80]

$$\varphi_{\ell m} = \sum_{k=0}^{\ell} \frac{(k+\ell)!}{2^k k!(\ell-k)!} \frac{1}{r^{k+1}} [F^{\ell-k}(u) - (-1)^{\ell-k} F^{\ell-k}(v)] \,, \tag{2.18}$$

where $u = t - r$ is the retarded time, $v = t + r$ is the advanced time, and F is a real-valued function that decays at large argument, and that it is determined by the chosen initial data for the partial wave and its time derivative.

2.2.2 *Deformation functions*

In order to generate nonlinear equations, the deformed scalar field ϕ is defined as

$$\phi \equiv D(\varphi), \tag{2.19}$$

for which whenever φ satisfies Eq. 2.15 it must solve

$$\Box\phi - \chi \nabla_a \phi \nabla^a \phi = 0 \,, \tag{2.20}$$

where $\nabla_a \phi \nabla^a \phi \equiv -(\partial_t \phi)^2 + (\partial_r \phi)^2 + \mathbb{\nabla}_a \phi \mathbb{\nabla}^a \phi$ and $\mathbb{\nabla}$ denotes the covariant derivative induced by η_{ab} on the two-spheres of constant u and v. Let us see in more detail how this happens

$$\begin{aligned} \Box\phi &= \nabla^a \nabla_a \left(D(\varphi)\right) = \nabla^a \left(D'(\varphi) \nabla_a \varphi\right) \\ &= D''(\varphi) \nabla^a \varphi \nabla_a \varphi + D'(\varphi) \nabla^a \nabla_a \varphi. \end{aligned} \tag{2.21}$$

Taking into account that by Eq. 2.15, $D'(\varphi)\nabla^a \nabla_a \varphi = 0$ is satisfied, replacing $\varphi = D^{-1}\phi$ and moving terms to the left hand side it is possible to arrive to Eq. 2.20 where being D the deformation function twice continuosly differentiable, the coefficient χ from Eq. 2.20 takes the form

$$\chi = \tfrac{D''}{D'^2}, \tag{2.22}$$

and it is single valued when represented as a function of ϕ. It is required, moreover, that the deformation function $D(\varphi) \simeq \varphi$ for small φ, so the model will have small data global existence. This last condition also implies that analytic solutions to Eq. 2.20 can be trivially constructed using Eq. 2.16. It is important to note, however, that the specific type of blowup, if happens, is determined by the specific choice of the deformation function $D(\varphi)$ and as it will be shown in Sections 2.4.3 and 2.4.4 it will depend on its periodicity. Below there is the list of the models studied in this manuscript.

2.2.3 *Model 1*

The deformation function that generates this model is

$$\phi = D(\varphi) \equiv A_1^{-1} \log(1 + A_1 \varphi) \,, \tag{2.23}$$

which results in the nonlinear wave equation

$$\Box\phi + A_1 \nabla_a \phi \nabla^a \phi = 0\,, \tag{2.24}$$

where $A_1 \in \mathbb{R}$ is a constant that can be freely chosen. This is the classical example of Nirenberg that motivates the classical null condition for nonlinear wave equations that, on a Minkowski spacetime, requires that for a nonlinearity of the form $A^{\mu\nu}\partial_\mu\Phi\partial_\nu\Phi$ the equality $A^{\mu\nu} = \xi_\mu\xi_\nu$ holds for any null vector ξ_μ, as it is discussed in [81]. This model is the simplest among the presented ones, but it is a good start to preparing the code of Section 2.4.1 to solve the non-analytical models reliably.

2.2.4 *Model 2*

Although model 1 from above (2.2.3) is an interesting exercise manipulation of the wave equation, the ultimate interest lies in model equations that appear in physical applications of GR. This Chapter of the manuscript aims to prove that not only the system in GR show the properties of threshold solutions, therefore numerical solutions to semilinear wave models will be computed, being the first of these models a modification of model 1 in which there are two coupled scalar fields described by

$$\begin{aligned} &\Box\phi_1 + A_2 \nabla_a \phi_2 \nabla^a \phi_2 = 0\,, \\ &\Box\phi_2 + B_2 \nabla_a \phi_1 \nabla^a \phi_1 = 0\,. \end{aligned} \tag{2.25}$$

For model 2 analytical solutions are not known, only in the particular case $A_2 = B_2 = A_1$ the model reduces to model 1 of Eq. 2.24 as ϕ_1 and ϕ_2, as well as their derivatives, agree as functions. Hence, for this model the numerical method described in Section 2.4 is used.

2.2.5 *Model 3*

By studying plots of the Choptuik solution, for instance Figs 3 and 4 of [65], one might be reminded of the textbook example the topologists sine curve defined by $f(x) = \sin(1/x)$ where $x \in (0, 1]$. This connection gives the idea of experimenting deformation functions involving periodic functions. Let us then adjust the construction from Ep. 2.20 (also to avoid branch cuts) as

$$\begin{aligned} \phi_1 &= D_1(\varphi) \equiv A_3 \sin\left[A_3^{-1}\log(1+\varphi)\right]\,, \\ \phi_2 &= D_2(\varphi) \equiv A_3 \cos\left[A_3^{-1}\log(1+\varphi)\right]\,. \end{aligned} \tag{2.26}$$

Note that although these deformations are not globally invertible, $D_1''/D_1'^2$ and $D_2''/D_2'^2$ are single-valued functions of both ϕ_1 and ϕ_2.

Following the procedure of Eq. 2.21 it generates the nonlinear coupled model

$$\begin{aligned}\Box\phi_1 + \frac{\phi_1 + A_3\phi_2}{A_3^2 - \phi_1^2}\nabla_a\phi_1\nabla^a\phi_1 = 0\,,\\ \Box\phi_2 + \frac{\phi_2 - A_3\phi_1}{A_3^2 - \phi_2^2}\nabla_a\phi_2\nabla^a\phi_2 = 0\,,\end{aligned} \tag{2.27}$$

that also has the algebraic constraint

$$\phi_1^2 + \phi_2^2 = A_3^2. \tag{2.28}$$

Although Eq. 2.27 gives the system for model 3, its presentation is not ideal for a numerical implementation since it has poles. In order to avoid these poles, the constraint can be treated to give extra information, as follows

$$\nabla_a\phi_1\nabla^a\phi_1 = \nabla_a\sqrt{A_3^2 - \phi_2^2}\nabla^a\sqrt{A_3^2 - \phi_2^2} = \frac{\phi_2^2}{A_3^2 - \phi_2^2}\nabla_a\phi_2\nabla^a\phi_2. \tag{2.29}$$

Now, substituting $\phi_2^2 = A_3^2 - \phi_1^2$ and reorganizing it is possible to arrive at the first equality out of the constraint, that corresponds to Eq. (26) from [69] where a typo was found, being the correct expression

$$\frac{\nabla_a\phi_1\nabla^a\phi_1}{A_3^2 - \phi_1^2} - \frac{\nabla_a\phi_2\nabla^a\phi_2}{A_3^2 - \phi_2^2} = 0\,. \tag{2.30}$$

Applying the D'Alambertian operator to the algebraic constraint allows to compute this second equality that emerges from the constraint

$$\phi_1\Box\phi_1 + \phi_2\Box\phi_2 + \nabla_a\phi_1\nabla^a\phi_1 + \nabla_a\phi_2\nabla^a\phi_2 = 0\,. \tag{2.31}$$

Bringing together Eq. 2.30 and Eq. 2.31 with the system 2.27 it results in

$$\nabla_a\phi_1\nabla^a\phi_1 + \nabla_a\phi_2\nabla^a\phi_2 = A_3^2\frac{\nabla_a\phi_1\nabla^a\phi_1}{A_3^2 - \phi_2^2}. \tag{2.32}$$

Now using this relation in Eq. 2.27 it is clear that model 3, with the algebraic constraint from Eq. 2.28, can be expressed by avoiding the poles as

$$\begin{aligned}\Box\phi_1 + A_3^{-2}\left(\phi_1 + A_3\phi_2\right)\left(\nabla_a\phi_1\nabla^a\phi_1 + \nabla_a\phi_2\nabla^a\phi_2\right) = 0\,,\\ \Box\phi_2 + A_3^{-2}\left(\phi_2 - A_3\phi_1\right)\left(\nabla_a\phi_1\nabla^a\phi_1 + \nabla_a\phi_2\nabla^a\phi_2\right) = 0\,.\end{aligned} \tag{2.33}$$

For the IVP (Cauchy problem), solutions with initial data satisfying Eq. 2.28 will be of the form of Eq. 2.26 and will satisfy the algebraic constraint for all times. As well, for the IBVP, the boundary conditions need to be constraint preserving. It is clear already, that blowup

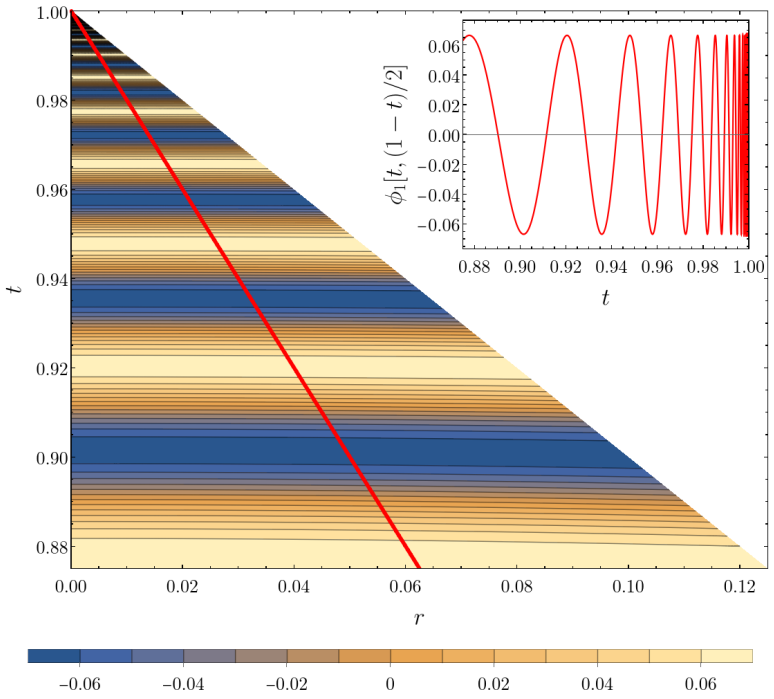

Figure 2.1: A contour plot of a threshold solution of model 3 with $A_3 = 1/15$, see Eq. (2.26). The parameter here was chosen simply for clarity of plotting. This threshold solution blows up in H^1 (and not in L^2) in a DSS fashion at $(t_\star, r_\star) = (1, 0)$. In the inset the solution is plotted along the red curve $t + 2r(t) = 1$ indicated in the main plot. The figure is naturally compared with Fig. 1 of [82]. The colors from the colormap refer to the value of the scalar field.

solutions for this model will be oscillatory in nature. Furthermore, for the interested reader, there is a more succinct way to express model 3 by eradicating either ϕ_1 or ϕ_2 in Eq. 2.27 using the constraint Eq. 2.28, yielding

$$\Box\phi_1 + \frac{\phi_1 + A_3\sqrt{\phi_1^2 - A_3^2}}{A_3^2 - \phi_1^2}\nabla_a\phi_1\nabla^a\phi_1, \tag{2.34}$$

$$\Box\phi_2 + \frac{\phi_2 - A_3\sqrt{\phi_2^2 - A_3^2}}{A_3^2 - \phi_2^2}\nabla_a\phi_2\nabla^a\phi_2, \tag{2.35}$$

for which the equations are decoupled and correspond to two different systems, corresponding to the positive and negative signs of the square root. In Fig. 2.1 a spherical solution associated with this model is plotted at the threshold of blowup in the past light cone of the blowup point, for a specific choice of the parameters.

2.2.6 *Model 4*

As model 2 from Section 2.2.4 might be seen as an extension of model 1 from Section 2.2.3, in this case what it is introduced as model 4 can be seen as an extension to model 3 from Section 2.2.5 by dropping the algebraic constraint Eq. 2.28, therefore the adjusted equations of motion are

$$\begin{aligned}\Box\phi_1 + A_4^{-2}\left(\phi_1 + A_4\phi_2\right)\left(\nabla_a\phi_1\nabla^a\phi_1 + \nabla_a\phi_2\nabla^a\phi_2\right) = 0\,,\\ \Box\phi_2 + B_4^{-2}\left(\phi_2 - B_4\phi_1\right)\left(\nabla_a\phi_1\nabla^a\phi_1 + \nabla_a\phi_2\nabla^a\phi_2\right) = 0\,.\end{aligned} \tag{2.36}$$

Solutions to this system are not known analytically, in general, since it was not obtained from a deformation of the wave equation, but for the specific choice of $A_4 = B_4$ and when the constraint Eq. 2.28 is satisfied, model 3 is recovered. The numerical results for this model are carefully studied in Section 2.4, where it is examined if the oscillatory behavior of model 3 is also present in this model.

2.2.7 *Model 5*

Coming back to the general deformation function, conformal metric can be defined as $\tilde{\eta}_{ab} = \Omega^2\eta_{ab}$ where the inverse conformal metric is denoted as $\tilde{\eta}^{ab}$ and the associated covariant derivative by $\tilde{\nabla}_a$. It is possible then to compute the conformal factor Ω^2 such that the generic deformation equation 2.20 can be rewritten as a wave equation in terms of this conformal metric.

For the wave equation $\Box\varphi = 0$ the associate standard stress-energy tensor is

$$T_{ab}[\varphi] = \nabla_a\varphi\nabla_b\varphi - \frac{1}{2}\eta_{ab}\nabla^c\varphi\nabla_c\varphi, \tag{2.37}$$

and it is covariantly conserved $\nabla^b T_{ab}[\varphi] = 0$. On the other hand, the stress-energy tensor for the scalar field ϕ responds to

$$T_{ab}[\phi] = (D')^2 T_{ab}[\varphi], \tag{2.38}$$

case in which the covariant conservation takes the form $\nabla^b\left[T_{ab}[\phi](D')^2\right]$. Rewritting the latter expression in terms of $\tilde{\nabla}_a$ and $\tilde{\eta}_{ab}$ the following relation appears

$$\tilde{\nabla}^b T_{ab}[\phi] = \tilde{\nabla}_a\phi\left(\tilde{\nabla}^b\phi\tilde{\nabla}_b\phi\right)\left[\ln\frac{\Omega^2}{D'}\right]. \tag{2.39}$$

It is clear now that by choosing $\Omega^2 = D' = \partial_\varphi D$ (please, be aware that in [69] there is a typo in first paragraph of Section G, where it states that $\Omega^{-2} = \partial_\varphi D$) the conformal stress-energy is also convariantly conserved $\tilde{\nabla}^b T_{ab}[\phi] = 0$, therefore, it is possible to rewrite Eq. 2.20 as

$$\tilde{\Box}\phi = \tilde{\eta}^{ab}\tilde{\nabla}_a\tilde{\nabla}_b\phi = 0. \tag{2.40}$$

As a consequence, the deformed wave equation automatically admits the standard stress-energy,

$$T_{ab}[\phi] = \tilde{\nabla}_a\phi\tilde{\nabla}_b\phi - \tfrac{1}{2}\tilde{\eta}_{ab}\tilde{\nabla}^c\phi\tilde{\nabla}_c\phi\,. \tag{2.41}$$

In this way, the original model has been rewritten in a clean geometric manner that results in a quasilinear equation. This reformulation by itself is not of particular help, nevertheless, the conserved energy will be useful in the future to prove the findings of this manuscript rigorously. Furthermore, this construction allows for building more general DSS-type models. Let $\phi = \phi_0$ and take D, the deformation function, as monotonic increasing on its domain. Inspired by 2.27, set

$$\phi_1 = P_1(\phi_0)\,, \qquad \phi_2 = P_2(\phi_0)\,, \tag{2.42}$$

where P_1 and P_2 are any periodic functions that satisfy

$$P_1^2 + P_2^2 = \delta^2\,, \qquad P_1'^2 + P_2'^2 = \varepsilon^2\,, \tag{2.43}$$

with δ and ε positive functions of ϕ_0 uniformly bounded above and below away from 0. Analogous calculations to those for model 3 leading to Eq. 2.33 arrive at the regularized equations of motion for model 5

$$\begin{aligned}
&\tilde{\Box}\phi_1 - \varepsilon^{-2}P_1''(\phi_0)\left(\tilde{\nabla}^a\phi_1\tilde{\nabla}_a\phi_1 + \tilde{\nabla}^a\phi_2\tilde{\nabla}_a\phi_2\right) = 0\,,\\
&\tilde{\Box}\phi_2 - \varepsilon^{-2}P_2''(\phi_0)\left(\tilde{\nabla}^a\phi_1\tilde{\nabla}_a\phi_1 + \tilde{\nabla}^a\phi_2\tilde{\nabla}_a\phi_2\right) = 0\,.
\end{aligned} \tag{2.44}$$

For a complete model, these equations might be solved, together with 2.40. The fields ϕ_1 and ϕ_2 have a combined stress-energy $T_{ab}[\phi_1] + T_{ab}[\phi_2] = \varepsilon^2 T_{ab}[\phi_0]$ that is conserved with $\tilde{\nabla}_a$ after carrying out the analogous conformal transformation to the general ϕ. The disadvantage of this model is that it requires more fields, however, it is more robust than model 3 as it grants a large amount of freedom in the choosing of a compactifying function. A flaw of using Eq. 2.40 with Eq. 2.44 is that the coupling between the fields is one-directional, which, when choosing initial data that violate the various constraints between the different fields, makes it impossible to create nontrivial evolution in ϕ_0 from ϕ_1 and ϕ_2. Nonetheless, a modification can be made to sidestep this weakness. From Eqs. 2.42 and 2.43 it is possible to compute and use

$$\varepsilon^2\tilde{\nabla}^a\phi_0\tilde{\nabla}_a\phi_0 = \tilde{\nabla}^a\phi_1\tilde{\nabla}_a\phi_1 + \tilde{\nabla}^a\phi_2\tilde{\nabla}_a\phi_2\,, \tag{2.45}$$

now, by multiplying by Ω^{-2} Eq. 2.20 it can be expressed as

$$\hat{\Box}\phi_0 - \varepsilon^{-2}\chi\left(\tilde{\nabla}^a\phi_1\tilde{\nabla}_a\phi_1 + \tilde{\nabla}^a\phi_2\tilde{\nabla}_a\phi_2\right) = 0\,, \tag{2.46}$$

where $\hat{\Box}\phi_0 \equiv \tilde{\eta}^{ab}\nabla_a\nabla_b\phi_0$ is the reduced wave operator associated to $\tilde{\eta}_{ab}$, and χ is viewed as a function of ϕ_0. It is remarkably that the combined system from Eq. 2.44 and Eq. 2.46 admits a natural analogy to GR. The fields ϕ_1, ϕ_2 are analogous to some field theory matter and, since it is required in building $\tilde{\eta}_{ab}$, the field ϕ_0 is equivalent to a metric component.

2.3 CRITICALITY, REGULARITY AND THE THRESHOLD OF BLOWUP

In this section, the focus is on nonlinear equations with analytical solutions, as models 1 and 3 from Sections 2.2.3 and 2.2.5, that are generated from a deformation of the wave equation. It is examined the extent to which threshold solutions and those in their neighborhood in phase space display behavior like the one in gravitational collapse. The starting point will be the spherical solutions to afterward move on to more general solutions.

2.3.1 *Bounds and blow up in spherical symmetry*

First of all, let us settle that spherical threshold solutions blow up at the origin. In this context, solutions to the flat wave equation (Eq. 2.15) take the form

$$\varphi = \frac{1}{r}\left[F(t+r) - F(t-r)\right], \tag{2.47}$$

where $F(x)$ is an arbitrary function. Consider a subset $\{\varphi_\star(t,r)\}$ of the solutions Eq. 2.47, such that for $t < t_\star$, $\varphi_\star(t,r) > \xi_\star$, where $\xi_\star$ is some constant, and $\varphi_\star(t_\star, r_\star) = \xi_\star$ is a local minimum. Let us assume the notation that the label $\star$ stands for blowup. As an illustrative example, the point $(t_\star, r_\star)$ is the location of the blowup in the deformed wave equation. Due to spherical symmetry, the minimum must be reached at the origin, therefore $r_\star = 0$. To prove this let us imagine, on the contrary, that $r_\star > 0$. Since $(t_\star, r_\star)$ is a local extremum

$$\begin{aligned} r_\star\left[F'_\star(t_\star + r_\star) + F'_\star(t_\star - r_\star)\right] &= F_\star(t_\star + r_\star) - F_\star(t_\star - r_\star), \\ F'_\star(t_\star + r_\star) &= F'_\star(t_\star - r_\star), \end{aligned} \tag{2.48}$$

which implies that

$$\varphi_\star(t_\star, r_\star) = 2F'_\star(t_\star - r_\star) = \xi_\star. \tag{2.49}$$

On the other hand, using L'Hôpital to compute the limit of Eq. 2.47 when $r \to 0$, at the origin happens

$$\varphi_\star(t,0) = 2F'_\star(t), \tag{2.50}$$

which, by choosing an adequate time $t = t_\star - r_\star$ gives

$$\varphi_\star(t_\star - r_\star, 0) = \varphi_\star(t_\star, r_\star) = \xi_\star. \tag{2.51}$$

By assumption $r_\star > 0$, so this contradicts the assumption that $\varphi_\star(t,0) > \xi_\star$ for $t < t_\star$. Hence $r_\star = 0$ must be always satisfied, which means that the global minimum of a spherical solution to the wave equation always happens at the origin. Let us consider now a compactifying deformation function $D[\varphi] = \mathcal{C}(\varphi)$, as a logarithm for example, with $\mathcal{C}(\varphi)$ defined on $\varphi > \xi_\star$ and such that the blowup

$$\lim_{\varphi \to \xi_\star} \mathcal{C}(\varphi) = \infty. \tag{2.52}$$

Call from Section 2.2 the additional requirement on the deformation function, which in this case translates as $\mathcal{C}(\varphi) \simeq \varphi$ for small φ. For a one-parameter family of initial data, the solutions of Eq. 2.20 at the threshold between global existence and blowup are of the form $\phi_\star(t,r) \equiv \mathcal{C}\left[\varphi_\star(t,r)\right]$, and by the previous discussion must blow up at $(t_\star, 0)$.

2.3.2 *Criticality of spherical threshold solutions*

All the studied models with analytical solutions share the property that the threshold solutions of these deformation models are universal in the sense that the structure of their blowup close to $(t_\star, 0)$ is independent of the initial data. These universal solutions are referred to as *critical solutions*. Please be aware that all critical solutions are threshold solutions but not all threshold solutions are critical, for instance, if a threshold solution depends on the initial conditions it will not be critical. To explain how universality appears let us start by noticing that the original solution to the wave equation satisfies

$$\begin{aligned}\lim_{(t,r)\to(t_\star,0)} \varphi_\star(t,r) \sim \xi_\star &+ \tfrac{1}{2}\partial_t^2\varphi_\star(t_\star,0)\,(t_\star - t)^2 \\ &- \tfrac{1}{2}\partial_t\partial_r\varphi_\star(t_\star,0)\,(t_\star - t)\,r + \tfrac{1}{2}\partial_r^2\varphi_\star(t_\star,0)r^2\,.\end{aligned} \tag{2.53}$$

Moreover, it is easy to show that $\partial_t\partial_r\varphi(t,0) = 0$ and $\partial_t^2\varphi(t,0) = 3\partial_r^2\varphi(t,0) = 2F'''(t)$ for any regular solution (2.18) of the wave equation. The last limit thus becomes

$$\begin{aligned}\lim_{(t,r)\to(t_\star,0)} \varphi_\star(t,r) &\sim \xi_\star + F_\star'''(t_\star)\left[(t_\star - t)^2 + \tfrac{1}{3}r^2\right] \\ &\sim \xi_\star + F_\star'''(t_\star)e^{-2T}\left(1 + \frac{1}{3}X^2\right)\,,\end{aligned} \tag{2.54}$$

where in the last step similarity adapted coordinates were introduced

$$T = -\log(t_\star - t)\,, \qquad X = (t_\star - t)^{-1}r\,, \tag{2.55}$$

and an expansion about $(t_\star, 0)$ was carried out.

Let us give an illustrative example. Pick model 1 from Section 2.2.3 and set $A_1 = 1$. In this case the compactifying function is $\mathcal{C}(\varphi) = \log(1+\varphi)$ and $\xi_\star = -1$, which turns over

$$\lim_{(t,r)\to(t_\star,0)} \phi_\star(t,r) \sim -2T + \log\left(1 + \tfrac{1}{3}X^2\right) + \log\left[F_\star'''(t_\star)\right]\,, \tag{2.56}$$

where the first term is the critical solution. Please, note that in the past light cone of the neighborhood of $(t_\star, r_\star)$, the similarity adapted coordinate $X \leq 1$. The expression Eq. 2.56 is independent of the initial data to leading order, which highlights the universality of blowup of critical solutions, which happens in L^∞. This critical solution is

approximately CSS, centered at the blowup point, and with degree $\nu = 0$ (see Eq. 2.5)

$$\lim_{(t',r)\to(0,0)} \phi_\star(t_\star + \lambda t', \lambda r) \sim \phi_\star(t_\star + t', r)\,. \tag{2.57}$$

2.3.3 *Alternative compactifications*

For a more general class of models with $\xi_\star = -1$, consider

$$\mathcal{C}(\varphi) = \frac{1}{n}\Big(1 - \frac{1}{(1+\varphi)^n}\Big), \tag{2.58}$$

where $n > 0$, and so one has

$$\lim_{(t,r)\to(t_\star,0)} \phi_\star(t,r) \sim \tfrac{1}{n}\left[F_\star'''(t_\star)\right]^{-n}\left(1 + \tfrac{1}{3}X^2\right)^{-n} e^{2nT}\,. \tag{2.59}$$

In this case, the universality of blowup of threshold solutions is weaker, since there is a dependence on the initial conditions through $\partial_t^2\varphi_\star(t_\star, 0)$. However, there is still a universal power $2n$. It is remarkable that the entire freedom within a large function space boils down just to one parameter at the threshold. It is appealing to think of the single remaining parameter as a single hair of "the" critical solution, so that uniqueness can be understood in a parameterized sense as in the standard discussion of stationary BHs with symmetry. The threshold solutions of these models blow up in a CSS form, centered at the blowup point, with $\nu = -2n$ (see Eq. 2.5).

2.3.4 *Deformations using periodic functions*

In this section the target is to express the deformation function as the functional $D[\varphi] \equiv \mathcal{P}\circ\mathcal{C}(\varphi)$ with $\mathcal{P}$ a bounded periodic function with period Λ, satisfying $\lim_{\mathcal{C}\to 0}\mathcal{P}(\mathcal{C}) \sim \mathcal{C}$. Using this construction, solutions to Eq. 2.20 have global existence for small initial data, however, the first derivative of the field must explode up for large initial data. In this setup threshold solutions are the ones at the verge between dispersion and blowup of the first derivative of the solution, with the form $\phi_\star(t,r) \equiv \mathcal{P}\circ\mathcal{C}[\varphi_\star(t,r)]$. Again, for this type of deformation functions the blowup of these threshold solutions occurs at the origin $(t_\star, 0)$ and it is universal. For this type of deformation function the first derivatives are

$$\begin{aligned}
\partial_t\phi_\star(t,r) &= \mathcal{P}'\circ\mathcal{C}[\varphi_\star(t,r)]\,\mathcal{C}'[\varphi_\star(t,r)]\,\partial_t\varphi_\star(t,r)\,,\\
\partial_r\phi_\star(t,r) &= \mathcal{P}'\circ\mathcal{C}[\varphi_\star(t,r)]\,\mathcal{C}'[\varphi_\star(t,r)]\,\partial_r\varphi_\star(t,r)\,.
\end{aligned} \tag{2.60}$$

Model 3 from Section 2.2.5 corresponds to this new class of deformation function, with $\xi_\star = -1$, period $\Lambda = 2\pi$ and

$$\phi_1 = \mathcal{P}\circ\mathcal{C}(\varphi) = A_3 \sin\left[A_3^{-1}\log(1+\varphi)\right]\,, \tag{2.61}$$

which results in the bounded field

$$\lim_{(t,r)\to(t_\star,0)} \phi_{1\star}(t,r) \sim A_3 \sin\left[A_3^{-1}\log\left(F_\star'''(t_\star)e^{-2T}\left[1+\frac{1}{3}X^2\right]\right)\right], \tag{2.62}$$

with the blowup of the first derivatives happening as

$$\lim_{(t,r)\to(t_\star,0)} \partial_t\phi_{1\star}(t,r) \sim \tag{2.63}$$
$$-\frac{6\,e^T}{3+X^2}\cos\left(A_3^{-1}\log\left(F_\star'''(t_\star)e^{-2T}\left[1+\frac{1}{3}X^2\right]\right)\right),$$

and

$$\lim_{(t,r)\to(t_\star,0)} \partial_r\phi_{1\star}(t,r) \sim \tag{2.64}$$
$$\frac{2Xe^T}{3+X^2}\cos\left(A_3^{-1}\log\left(F_\star'''(t_\star)e^{-2T}\left[1+\frac{1}{3}X^2\right]\right)\right).$$

The threshold solutions of model 3 blow up with a universal power. The dependence on the initial data reduces to one number, which is inside the trigonometric function, appearing just as a phase offset. In Section 2.4 numerical results are shown for this model. It is clear that the blowup of $\partial_t\phi_{1\star}$ and $\partial_r\phi_{1\star}$ is DSS, centered at $(t_\star,0)$, with degree $\nu=-1$ and $\lambda_m = e^{-m\Delta} = e^{m\pi A_3}$ (see Eq.2.5)

$$\lim_{(t',r)\to(0,0)} \partial_\mu\phi_{1\star}(t_\star+\lambda_n t',\lambda_n r) \sim \lambda_n^{-1}\partial_\mu\phi_{1\star}(t_\star+t',r)\,. \tag{2.65}$$

Using the construction of model 5, alternative $\mathcal{P}\circ\mathcal{C}$ deformation models can be built. For example, by combining the compactification Eq. 2.58 with the periodic function sin,

$$\phi_1 = \sin\left[\frac{1}{n}\left(1-\frac{1}{(1+\varphi)^n}\right)\right]. \tag{2.66}$$

The threshold solutions of this model have the form

$$\lim_{(t,r)\to(t_\star,0)} \phi_{1\star}(t,r) \sim \quad \sin\left(\tfrac{1}{n}\left[F_\star'''(t_\star)\right]^{-n}\left[(t_\star-t)^2+\tfrac{1}{3}r^2\right]^{-n}\right), \tag{2.67}$$

which is bounded. Their first derivatives blow up with

$$\lim_{(t,r)\to(t_\star,0)} \partial_t\phi_{1\star}(t,r) \sim \quad 2\left[F_\star'''(t_\star)\right]^{-n}\frac{t_\star-t}{\left(\left[t_\star-t\right]^2+\frac{1}{3}r^2\right)^{n+1}}\cos(*)\,, \tag{2.68}$$

and

$$\lim_{(t,r)\to(t_\star,0)} \partial_r\phi_{1\star}(t,r) \sim \quad -\tfrac{2}{3}\left[F_\star'''(t_\star)\right]^{-n}\frac{r}{\left(\left[t_\star-t\right]^2+\frac{1}{3}r^2\right)^{n+1}}\cos(*)\,, \tag{2.69}$$

where $\star$ here denotes the argument of the sin term in Eq. 2.66.

It is clear, by looking at the cos term, that in these coordinates the blowup does not satisfy the symmetry from Eq. 2.5. An appropriate coordinate system, which would imply a DSS blowup, was not found so far, however, this possibility is not excluded. Nevertheless, the power of blowup is still universal, and (as before) it is $2n$. Again, the freedom of the critical solution is reduced to one single parameter. Interestingly, much of the desired phenomenology can be achieved but with threshold solutions of an apparently different character. If one wants to insist on finding alternative models that do have DSS threshold solutions it might be worth trying deformation functions of the form,

$$D(\varphi) \simeq e^{\mathcal{C}(\varphi)}\mathcal{P} \circ \mathcal{C}(\varphi)\,. \tag{2.70}$$

but for this manuscript, it is already enough to count with the simpler option above. All of the power-laws discussed so far appear in physical space. Forward in this section, similar results in phase space $(a - a_\star)$ are discussed.

2.3.5 *Regularity of spherical solutions at blowup*

So far, the focus was only on pointwise blowup, but a proper understanding of the threshold must also include statements about local integrability. Consider first deformation functions that involve only a compactification. As it has already been discussed, with this setup blowup solutions, whether generic or at the threshold, become unbounded pointwise. Therefore by Sobolev embedding (see Eq. 2.14) H^2 must explode, but beneath that, the story is more subtle. By choosing the initial data constant in space for the first time derivative out to some radius and then cutting off, it is clear that solutions can blow up in L^2 for any of the pure compactification deformation functions. But around the threshold, the solutions blow up in a special, localized manner, so that boundedness in L^2 depends on the specific deformation function or compactification. This must also fall in line with the observations made in the previous section about the regularity of self-similar functions. In fact, since the compactification determines also the degree ν, there must exist a relationship between the universal powers and regularity at the threshold. To examine this, it is supposed that the integral is dominated by the values of the integrand at the origin. Expanding then, with the log compactification one finds that

$$\begin{aligned} ||\phi_\star||_{L^2} &\sim e^{-3T/2}T\,, & ||\phi_\star||_{E^1} &\sim e^{-T/2}\,, \\ ||\phi_s||_{L^2} &\sim T\,, & ||\phi_s||_{E^1} &\sim e^{T}\,, \end{aligned} \tag{2.71}$$

for threshold solutions. Here it is used the fact that, at the threshold, the spatial scale on which the solution becomes large pointwise is fixed

in the similarity coordinate X. It is assumed that the blowup of the supercritical solution ϕ_s occurred at the origin with the spatial scale fixed in r, and by setting the slow-time $T = -\log(t_\star - t)$, with $t_\star$ the instant at which the solution explodes, so that $T \to \infty$ at the blowup. Thus this estimate on ϕ_s need not be verified in practice, and indeed it is easy to come up with examples in which $L^2(\phi_s)$ is finite even at blowup. For the alternative compactification Eq. 2.58

$$\begin{aligned} ||\phi_\star||_{L^2} &\sim e^{(2n-3/2)T}, & ||\phi_\star||_{E^1} &\sim e^{(2n-1/2)T}, \\ ||\phi_s||_{L^2} &\sim e^{nT}, & ||\phi_s||_{E^1} &\sim e^{(n+1)T}. \end{aligned} \tag{2.72}$$

Again these naive estimates on ϕ_s need not be satisfied, and serve only as an indication of possible behavior. All of these estimates can be verified numerically and are in agreement with the results in Section 2.1. Moving on to deformation functions involving a periodic function, by construction, obviously solutions can never blow up in L^2. Proceeding as before,

$$||\phi_\star||_{E^1} \sim e^{-T/2}, \qquad ||\phi_s||_{E^1} \sim e^{T}, \tag{2.73}$$

for model 3 and

$$||\phi_\star||_{E^1} \sim e^{(2n-1/2)T}, \qquad ||\phi_s||_{E^1} \sim e^{(n+1)T}, \tag{2.74}$$

with the composite deformation function $\sin \circ \mathcal{C}$ taking again the compactification Eq. 2.58. As mentioned in the discussion above, these predictions are checked in practice by computing numerically norms for different blowup solutions. Some examples are shown in Fig. 2.2. In summary, threshold solutions blow up at $t = t_\star$ in E^1 when $n \geq 1/4$ (that is $\nu \leq -1/2$), and in the CSS setting in L^2 when $n \geq 3/4$ ($\nu \leq -3/2$). The two takeaways are first, that generic blowup solutions are less regular than threshold solutions, and second, that there is a direct relationship between the universal power and the specific level of regularity.

2.3.6 *Aspherical perturbations of spherical critical solutions*

So far it has been established that, in pure spherical symmetry, threshold solutions of the deformation models (models 1 and 3) depend on leading order on only one number from the initial data and are, in this sense, unique. Therefore, according to the usual picture of critical gravitational collapse, considering a one-parameter family of spherically symmetric initial data and tuning this parameter to the threshold of blowup, the critical solution is recovered. Furthermore, simply by continuous dependence on given data, spherical initial data close to the threshold generate solutions that appear like the critical solution for some time in their development. Evidently, the latter statement is true also for nonspherical perturbations of the spherical

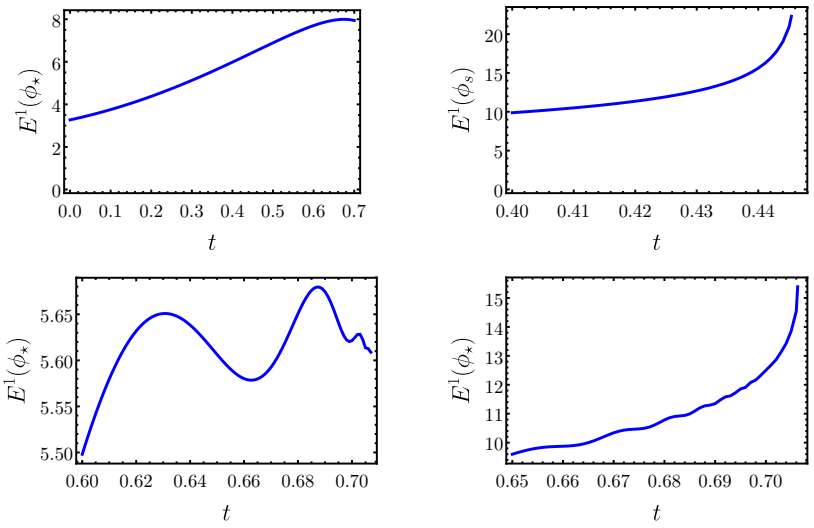

Figure 2.2: Plots of the E^1 norm for spherical solutions of various models up to the time at which some field quantity explodes in L^∞. On the top left there is a threshold solution for model 1. On the top right, a supercritical solution for the same model is shown, demonstrating that a variation of behavior is possible at blowup. On the bottom left there is the result for ϕ_1 from model 3 at the threshold. Finally, in the lower right panel, it is shown the same for the composite deformation function $\sin \circ \mathcal{C}$, with the compactification Eq. 2.58 and $n = 1/4$, which can be used in practice within model 5. These examples are compatible with the consideration of self-similar functions and the previous naive norm estimates.

critical solution. But in fact, a stronger result holds. Take a family of spherical solutions $\phi_a(t,r) = D[a\,\varphi_\star(t,r)]$ normalized so that $a = 1$ corresponds to the threshold solution $\phi_\star = \phi_1$. As discussed above, in the past light cone of the blowup point, $\phi_\star$ is associated with a critical solution by simple Taylor expansion. Let $\tilde{\varphi}$ denote *any* regular partial wave solution Eq. 2.16 with vanishing spherical component $\tilde{\varphi}_{00}$. One may think of this solution as being parameterized by the infinite number of parameters stating how much of each of the individual partial wave solutions $\tilde{\varphi}_{lm}$, each of which also has a fully functional degree of freedom, is present. Consider the perturbed solutions

$$\tilde{\phi}_a = D[a\,(\varphi_\star + \epsilon\,\tilde{\varphi})]\,, \tag{2.75}$$

and observe, crucially, from Eq. 2.18 that $\tilde{\varphi}_{lm}(t,r) = O(r^l)$ near the origin. One can then see that for ϵ sufficiently small $\tilde{\phi}_\star = \tilde{\phi}_1$ is *also* a threshold solution. Starting from $\tilde{\phi}_\star$, within this family, the *only* way to restore global existence is to reduce the strength parameter a. It seems that this result would fit nicely with a perturbative analysis along the lines of that given in [61]. To understand the effect of the $\tilde{\varphi}$ on the asymptotic solution in the past light-cone of the blowup point,

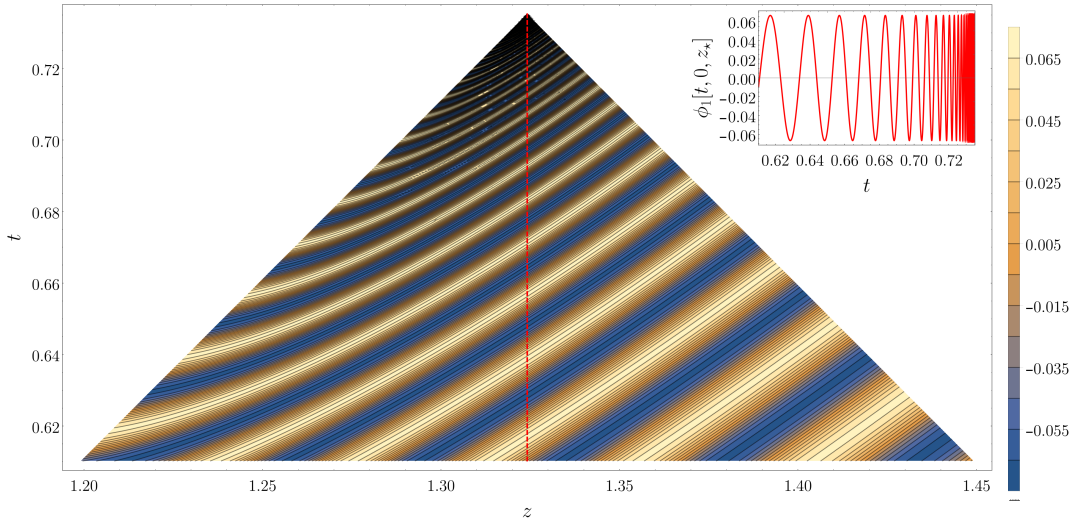

Figure 2.3: A contour plot of an axisymmetric threshold solution for model 3 shown on the symmetry axis. Despite shared attributes with the spherical solution of Fig. 2.1, there are obvious differences too, as the data here leading to blowup is mostly outgoing (as can be seen from the direction of the contours). The colors from the colormap refer to the value of the scalar field. For this model therefore the conjecture that there is in general a unique threshold solution regardless of initial data is false.

a generalization of the spherical Taylor expansion given above is presented below.

2.3.7 *Single-harmonic threshold solutions*

To this point, the behavior exhibited by solutions of the studied models had a direct analog to the standard picture of critical collapse. In moving to consider general nonspherical threshold solutions the way parts from that picture. The discussion here is focused on model 3 from Section 2.2.5, but holds more generally. Let us start by constructing a particular threshold solution from a pure $\ell = 2$, $m = 0$ partial wave solution φ_{20} to the wave equation. Recalling the exact solution Eq. 2.18 and working with the family generated by the Gaussian,

$$F(r) = ae^{-(r+1)^2}\,, \tag{2.76}$$

it is found that the threshold solution $\phi_\star$ is obtained with $a_\star \simeq 1.678$. As observed above, the partial wave vanishes at the origin, and therefore the blowup point occurs elsewhere, in this case at $(t_\star, x_\star, y_\star, z_\star) \simeq (0.735, 0, 0, 1.324)$. This threshold solution is plotted in Fig. 2.3. Although there are qualitative similarities with the spherical threshold solution plotted in Fig. 2.1 for the same model one could hardly claim that the two solutions are the same.

Impressively, even restricting to threshold solutions build from a single spherical harmonic as explained, there is still another distinct branch of threshold solutions. Consider, for instance, the spherical harmonic $Y_{20}(\theta^A)$ as

$$Y_{20}(\theta^A) = \frac{1}{4}\sqrt{\frac{5}{\pi}}\left(3\cos^2\theta^1 - 1\right), \tag{2.77}$$

which has local extrema on the x and z-axes. As the setup is axisymmetric, it is possible to identify x with the cylindrical radial coordinate. Therefore the solution to the wave equation

$$\varphi(t, r, \theta^A) = \varphi_{20}(t, r)Y_{20}(\theta^A) \tag{2.78}$$

giving rise to a solution of the deformed wave equation can explode the compactification in one of two ways,

$$\varphi_{20} = -2\sqrt{\frac{\pi}{5}}, \qquad \varphi_{20} = 4\sqrt{\frac{\pi}{5}}, \tag{2.79}$$

at some point, resulting in the first case in blowup of ϕ on the symmetry axis as plotted in Fig. 2.3, or else *on a ring* in the xy-plane in the second. A snapshot of a solution close to this type of blowup, obtained with the family

$$G(r) = -F(-r), \tag{2.80}$$

with F the Gaussian from before, is shown in Fig. 2.4.

2.3.8 *Blowup amplitudes under perturbations*

The previous example shows that threshold solutions constructed from a generic single harmonic are not unique, and may differ even in the topology of their blowup. In the spherical setting, it has been seen that adding arbitrary small perturbations to the initial data at the threshold nevertheless leaves the same critical amplitude. So an obvious question is whether or not threshold solutions built from a single harmonic, or sum of harmonics are locally unaffected by adding additional harmonics in the same sense. The answer is no. To see this, recall that the mechanism for this outcome in the spherical case was that higher order partial wave solutions vanish at the origin, where blowup is guaranteed to occur with spherical symmetry. In general the support of higher order partial waves includes however possible blowup points induced by another partial wave solution. Therefore a small addition of a higher order partial wave can render a threshold solution small enough to avoid blowup or drive it unambiguously over the threshold. The difference between the spherical and generic setup is illustrated by Fig. 2.5. General threshold solutions are thus described as a sum over all harmonics, with any individual harmonic potentially

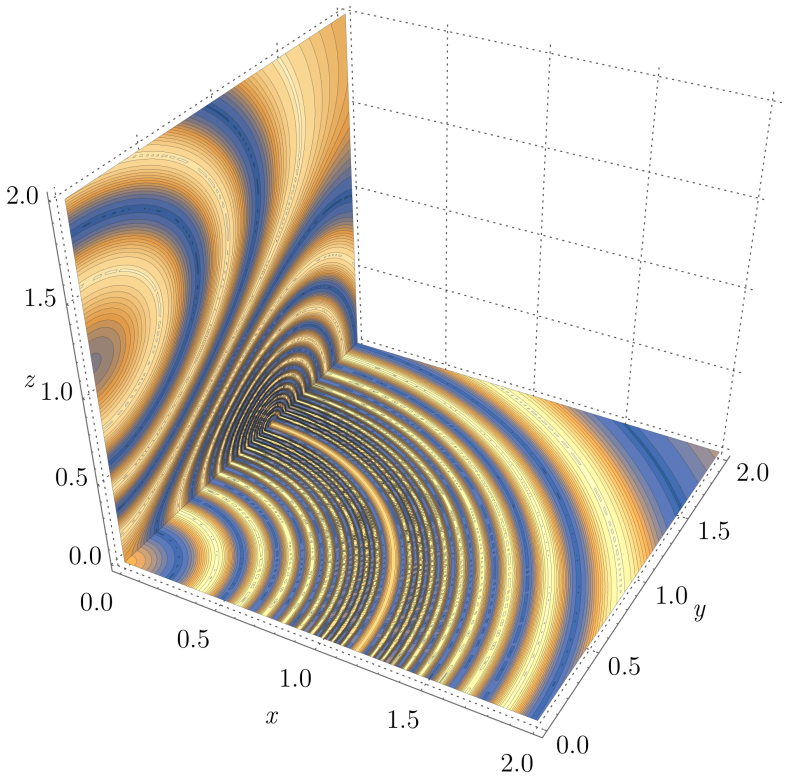

Figure 2.4: Here a pure $l = 2$, $m = 0$ threshold solution for model 3 is plotted shortly before blowup. Special in this case is that the blowup occurs on a ring in the $z = 0$ plane. The colors from the colormap refer to the value of the scalar field. This was achieved with the family Eq. 2.80, which may be thought of as the same data as Eq. 2.76, but evolved backward in time. This shows that away from spherical symmetry, even when building threshold solutions purely from a single harmonic, there exist fundamentally different threshold solutions, although the number of such branches for each harmonic is always presumably finite. This story becomes even more involved with higher harmonics.

playing a role in the blowup, and with different topologies, like the ring of Fig. 2.4, of the singular points possible. This behavior could be sidestepped by re-expanding the solution in terms of translated spherical harmonics centered at the blowup point, or more generally a point in the curve of blowup points, to again recover a basis well-adapted to the solution at hand.

2.3.9 *Self-similarity and generic threshold solutions*

By definition, a generic threshold solution can be obtained through the deformation $\phi_\star = D(\varphi_\star)$, where $\varphi_\star$ is a solution of the flat-space wave equation such that for $t < t_\star$, $\varphi_\star(t, x^i) > \xi_\star$, and $\varphi_\star(t_\star, x^i_\star) = \xi_\star$ is a local minimum. Again, the point $(t_\star, x^i_\star)$ is taken to be the location of blowup of the deformed solution. Because $\varphi_\star$ is a local

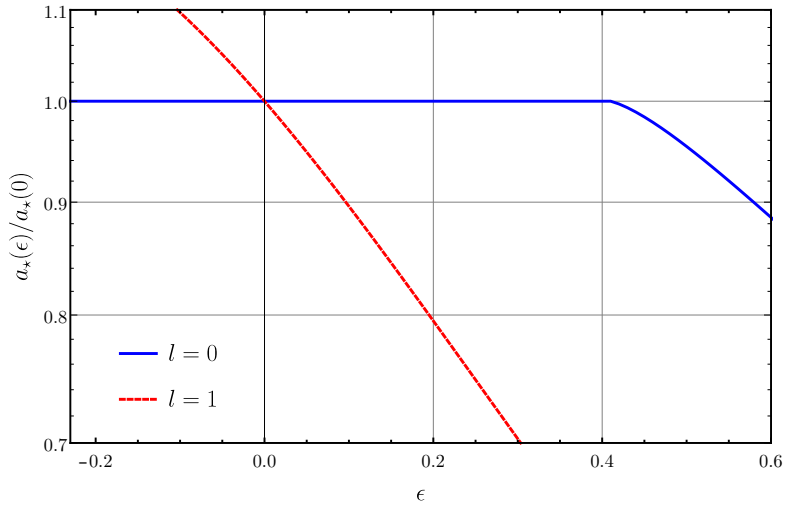

Figure 2.5: Plots of the blowup threshold amplitude starting from either a pure spherical solution (blue curve) or an $l = 1, m = 0$ solution (red dashed curve), and adding in each case by $l = 2, m = 0$ spherical harmonic parameterized by ϵ. See the main text following Eq. 2.75 for details. There is a neighborhood around the spherical solution in which the nonspherical deformation makes absolutely no difference to critical amplitude, although the asymptotic solution in the past light cone of the blowup point is modified. Once the perturbation is sufficiently large however the blue curve does bend away. At this point the threshold solution takes a structure similar to that illustrated in Fig. 2.3. It is expected that when the blue curve is extended to the left, eventually the threshold solution will take the form illustrated in 2.4. In contrast, the pure $l = 1$ threshold amplitude is immediately affected by the perturbation.

minimum at $(t_\star, x^i_\star)$, all first derivatives vanish at this point, and some second derivatives must be positive, like $\partial_t^2\varphi_\star$. However, the second derivatives $\partial_t\partial_i\varphi_\star$ and $\partial_j\partial_i\varphi_\star$ may be zero if the blowup happens on a curve or a surface (as illustrated in Fig. 2.4). It is assumed here that the blowup happens at a point, but the same discussion applies to any point in a curve or surface of blowup, with the caveat that the past light cone of each such point can be treated locally as follows, with a global understanding to be tackled separately. Close to this blowup point, the solution of the original flat-space wave equation is

$$\begin{aligned}\lim_{(t,x^i)\to(t_\star,x^i_\star)} \varphi_\star \sim\ & \xi_\star + \tfrac{1}{2}\partial_t^2\varphi_\star(t_\star - t)^2 \\ & - \partial_t\partial_i\varphi_\star(t_\star - t)(x^i - x^i_\star) \\ & + \tfrac{1}{2}\partial_i\partial_j\varphi_\star(x^i - x^i_\star)(x^j - x^j_\star)\,,\end{aligned} \tag{2.81}$$

with all derivatives evaluated at $(t_\star, x^i_\star)$. Uniqueness of the threshold solution in the spherical case, and the lack thereof in general, can be understood here from the fact that the derivatives in the former case depend only on the $l = m = 0$ partial wave solution, whereas

in general higher harmonics can contribute. To count the number of free-parameters here, first observe that, performing a trace/trace-free decomposition on $\partial_i\partial_j\varphi_\star$, the Laplace piece can be replaced using the wave equation. Then one might count nine free parameters. Introducing a spherical harmonic decomposition of $\varphi_\star$ centered at $x^i_\star$, it follows by the $O(r^l)$ property of the partial waves that only the lowest order (up to $l = 2$) harmonics can contribute, which gives a consistent count of parameters. The first derivatives are

$$\begin{aligned}\lim_{(t,x^i)\to(t_\star,x^i_\star)} \partial_t\varphi_\star &\sim \partial_t^2\varphi_\star(t_\star - t) + \partial_t\partial_i\varphi_\star(x^i - x^i_\star)\,,\\ \lim_{(t,x^i)\to(t_\star,x^i_\star)} \partial_i\varphi_\star &\sim \partial_i^2\varphi_\star(t_\star - t) - \partial_t\partial_i\varphi_\star(t_\star - t)\,.\end{aligned} \tag{2.82}$$

Let us look at the models arising from deformations using periodic functions. Using model 3 from Section 2.2.5, for instance, which has $\xi_\star = -1$, one has

$$\lim_{(t,x^i)\to(t_\star,x^i_\star)} \partial_t\phi_{1\star} \sim \quad - \lim_{(t,x^i)\to(t_\star,x^i_\star)} \cos\left[A_3^{-1}\log(1+\varphi_\star)\right]\frac{\partial_t\varphi_\star}{1+\varphi_\star} \tag{2.83}$$

and

$$\lim_{(t,x^i)\to(t_\star,x^i_\star)} \partial_i\phi_{1\star} \sim \quad - \lim_{(t,x^i)\to(t_\star,x^i_\star)} \cos\left[A_3^{-1}\log(1+\varphi_\star)\right]\frac{\partial_i\varphi_\star}{1+\varphi_\star}\,. \tag{2.84}$$

Close to the point $(t_\star, x^i_\star)$, the denominator $(1+\varphi_\star)$ is quadratic in $(t_\star - t, x^i - x^i_\star)$ and the first derivatives $\partial_t\varphi_{1\star}$ and $\partial_i\varphi_{1\star}$ are linear in the same argument. So, the argument applied to spherically symmetric solutions goes through, the conclusion is that the blowup of $\partial_t\phi_{1\star}$ and $\partial_i\phi_{1\star}$ is DSS, centered at $(t_\star, x^i_\star)$, with $\nu = -1$ and $\lambda_m = e^{-m\Delta} = e^{m\pi A_3}$.

Thus, as a remarkable finding, the CSS and DSS blowup properties of spherically symmetric threshold solutions, and even the non-standard behavior with more general compactifications like in model 5 from Section 2.2.7, can be extended to arbitrary threshold solutions. Now, however, nine parameters rather than one are required to characterize the asymptotic solution in the past-light cone of the blowup point.

2.3.10 *Power-law scaling around general threshold solutions*

So far, power-law behavior that occurs in physical space has been discussed, yet, in critical collapse such behavior is usually viewed in phase space. The focus is on this next, working with the time derivative of the field, since this allows the treatment of both types of model in a unified way. Consider a family of solutions $\phi_a = D[a\,\varphi]$, parameterized by a, with φ a fixed, nontrivial solution of the wave

equation which explodes the deformation function first at $a = a_\star$ as usual. Let $x^\mu(a)$ be the locus of maxima (in amplitude) of $\Pi_a = \partial_t \phi_a$, which defines a curve when $a \lesssim a_\star$, with $a_\star$ the threshold amplitude. Since Π_a attains a local maxima at $x^\mu(a)$,

$$\partial_t \Pi_a = a D'(a\,\varphi)\partial_t^2 \varphi + a^2 D''(a\,\varphi)(\partial_t \varphi)^2 = 0\,, \tag{2.85}$$

which is understood to hold at $x^\mu(a)$, and which it is possible to solve for $(\partial_t \varphi)^2$. Since this equation must hold for all values of a, one can derive in a, and obtain an expression for $t'(a)$ in terms of the other variables. Assuming more regularity on the curve, one can take higher derivatives too. Starting with the general expression for Π_a then

$$\Pi_a(x^\mu(a))^{-2} = \frac{D''(a\,\varphi)}{a D'(a\,\varphi)^3 \partial_t^2 \varphi}\,, \tag{2.86}$$

again understood to hold at $x^\mu(a)$. From here let us split the discussion into two cases. First suppose that $D = \mathcal{C}$ with the compactification Eq.2.58, assuming that $n > 0$. In this case Eq. 2.86 takes the form,

$$\Pi_a(x^\mu(a))^{-2} = -\frac{\mathcal{C}''(a\,\varphi)}{a\mathcal{C}'(a\,\varphi)^3 \partial_t^2 \varphi} = (n+1)\frac{(1+a\,\varphi)^{2n+1}}{a\,\partial_t^2 \varphi}\,. \tag{2.87}$$

Please be aware that in **??** there is a typo in Eq. 78, there is a factor $(n+1)$ missing that here has been corrected.

The objective now is to extract the piece of this that dominates as $a \to a_\star$. Since $\partial_t^2 \varphi$ is generically non-zero at the maximum and non-zero as $a \to a_\star$, it is needed only to consider

$$\frac{\mathcal{C}''(a\,\varphi)}{\mathcal{C}'(a\,\varphi)^3} = -(n+1)(1+a\,\varphi)^{2n+1}\,. \tag{2.88}$$

Raising this to the power $1/(2n+1)$, Taylor expanding at an arbitrary $a = a_0$, plugging in the result for $t'(a)$, and taking the limit $a_0 \to a_\star$ one can conclude that, in the regime $a \lesssim a_\star$,

$$\Pi_a(x^\mu(a)) \simeq (a - a_\star)^{-(2n+1)/2}\,. \tag{2.89}$$

The logarithmic compactification used in Eq. 2.23 is more subtle to treat, but corresponds to the case $n = 0$. In fact for this model the range $-1/2 < n < 0$ may also be interesting to investigate, but this is not done in here. Moving now to the case $D = \mathcal{P} \circ \mathcal{C}$, again for concreteness taking the compactification from (2.58), it is found that Eq. 2.87 is instead replaced by

$$-\Pi_a(x^\mu(a))^{-2} = \frac{\mathcal{P}''}{a\mathcal{P}'^3 \mathcal{C}(a\,\varphi)\partial_t^2 \varphi} + \frac{\mathcal{P}'\mathcal{C}''(a\,\varphi)}{a\mathcal{P}'^3 \mathcal{C}(a\,\varphi)^3 \partial_t^2 \varphi}\,. \tag{2.90}$$

Following from here the same procedure as before, noting that the first of these terms is now the leading piece, and raising to the power $1/(n+1)$, in the regime $a \lesssim a_\star$,

$$\Pi_a(x^\mu(a)) \simeq (a - a_\star)^{-(n+1)/2}\,. \tag{2.91}$$

Again the log compactification can be thought of as $n = 0$. With a little more care it is expected that one could see here also the superposed periodic wiggle. An important message is that power-law behavior may appear even in models for which self-similarity is absent at the threshold, so evidence of both phenomena is needed for a confident diagnosis. In summary, it is found that under mild assumptions on the regularity of $x^\mu(a)$, close to the threshold, all of the models admit universal power-laws regardless of the nature of the threshold solution itself. Nevertheless, some care is needed in interpreting this result. For general data, there may appear multiple "large-data" regions, and the peak of that which ultimately leads to blowup in the limit $a \to a_\star$ may be obfuscated, over some range of a, by another.

2.3.11 *Regularity of threshold vs generic blowup solutions*

Recovering results on the norms of threshold and blowup solutions in the nonspherical setting is trickier than in the previous case. Although the only numerical part of the calculation is in the evaluation of the norm itself, the solutions can be highly oscillatory. Nevertheless in all of the cases that one can reliably verify, which include all of those presented in Fig. 2.2, it is found that the spherical results carry over without any surprises, and that threshold solutions are slightly more regular than generic blowup solutions. In the future it will be interesting to use the geometric reformulation of the models given in Section 2.2 together with the conserved stress-energy to prove these properties beyond doubt.

2.4 NUMERICAL RESULTS

In the previous section, a fairly complete picture of threshold solutions for the models that arise as a deformation of the wave equation was given. To address the obvious criticism that such models may not be qualitatively representative of systems that do not arise as a deformation, in this section numerical evidence that similar phenomenology does occur within the non-deformation models is presented. Presently the results of this manuscript are restricted to spherical symmetry, postponing detailed numerical of generic threshold solutions for future work. First, the used method is briefly explained, before presenting the classification and numerical results for each model. Similar, though more comprehensive, numerical work for alternative models can be found in [74, 76–78, 83].

2.4.1 *Methods*

As presented in Section 2.2, all model equations are second order both in time and space. For the code implementation a reduction of the system to fully first order form is carried out and centered finite differences are used. To do so, the following auxiliary evolved fields are introduced,

$$\Phi = \partial_r \phi \,, \qquad \Pi = \partial_t \phi \,. \tag{2.92}$$

In order to deal with the coordinate singularity at the origin, the Evans method is applied, for any scalar field Ψ and its derivative $\Psi' = \frac{d\Psi}{dr}$, with $p = 2$ [84],

$$\Psi' + \tfrac{p}{r}\Psi = (p+1)\frac{d(r^p\Psi)}{d(r^{p+1})} \,, \tag{2.93}$$

where the differential operator can be expressed in terms of the grid points as,

$$(p+1)\frac{d(r^p\Psi)}{d(r^{p+1})} = (\tilde{D}\Psi)_i = (p+1)\frac{r_{i+1}^p\Psi_{i+1} - r_{i-1}^p\Psi_{i-1}}{r_{i+1}^{p+1} - r_{i-1}^{p+1}}. \tag{2.94}$$

In Section 2.1.2 definitions for the different norms were given, and their blowup for CSS and DSS functions was introduced and related. Below in this section, a classification of the presented models in section 2.2 is made following these criteria. The code itself is based on the method of lines with a Runge-Kutta 4 time integrator where the baseline numerical grid spacing in space is $h = 0.01$. The Courant-Friedrichs-Lewy factor is 0.4, so the time step is $\frac{2h}{5}$. For convergence tests resolution is always doubled for each new member of the convergence series, but for details see Section 2.4.2. The code itself is written in `Python`, and the longest numerical evolutions take just a few hours on a normal desktop machine. To avoid rapid growth of numerical error Kreiss-Oliger artificial dissipation [85] with a small dissipation parameter of order $\sigma = 0.02$ was used. The particular boundary conditions for each model are stated in their corresponding section.

To perform a bisection search to reach the threshold of blowup the first runs are made with the base resolution to obtain crude bounds. Afterward the resolution is doubled and the bisection search is performed, classifying the data as having blown up if $|\Pi(t,0)| > 10^{25}$. In most cases, the resolution was doubled once more and the bisection is redone as a consistency check. Since no surprises were found when increasing resolution like this in the searches, the focus is on the following primarily physical outcome rather than giving strict error-estimates.

2.4.2 *Convergence tests*

To have a trustable code, convergence tests are mandatory for all presented models (and variables of each model), and in particular here, they are performed for the critical amplitude, in the deformed models, or as close as possible to criticality for the remaining models. It is assumed that if the models converge at the critical amplitude (or as close as possibe), this is, in the most extreme regime, they will converge for any smaller initial data. For simplicity, in this section model 3 from Section 2.2.5 is used as an illustrative example, but all results are extended to all models and evolved fields.

2.4.2.1 *Norm convergence*

The objective of the norm convergence test is to check that the defined norm (in this case for Φ but analog for any other variable)

$$L^2_{HM} = \sum_{i=0}^{i=i_{max}} h\left(\Phi_H - \Phi_M\right)^2 \qquad (2.95)$$
$$L^2_{ML} = \sum_{i=0}^{i=i_{max}} h\left(\Phi_M - \Phi_L\right)^2$$

converges. The subscripts in this notation refer to the resolution used in the simulations, where H stands for "high", M for "medium" and L for "low", being typically $h_H = h_M/2 = h_L/4$ and $h = 0.01$. To check the convergence in Fig. 2.6 the logarithm in base 2 of the ratio of these two norms is plotted for the evolved variables Φ_1 and Π_1 of model 3. In this "boring" plot it is possible to see a constant line at the value of 2, which confirms that this code converges very nicely in the norm defined in Eq. 2.95. As said before, this result extends to all models and evolved fields, showing that the used code is robust in terms of norm convergence.

2.4.2.2 *Pointwise convergence*

For this type of convergence test, it is needed to run the code three times, corresponding to "low", "medium", and "high" resolution again as in Section 2.4.2.1. Then, the error corresponding to the difference between these runs $(\Phi_{M(H)} - \Phi_{L(M)})$ is plotted at the grid points corresponding to the "low" resolution for the whole radial domain. In Fig. 2.7 this result is plotted for the field Φ_1 of model 3, where it is possible to observe that the code has second order convergence as the error for the higher resolutions is four times smaller. This result is extended to all the other evolved fields for model 3 and also all the other models.

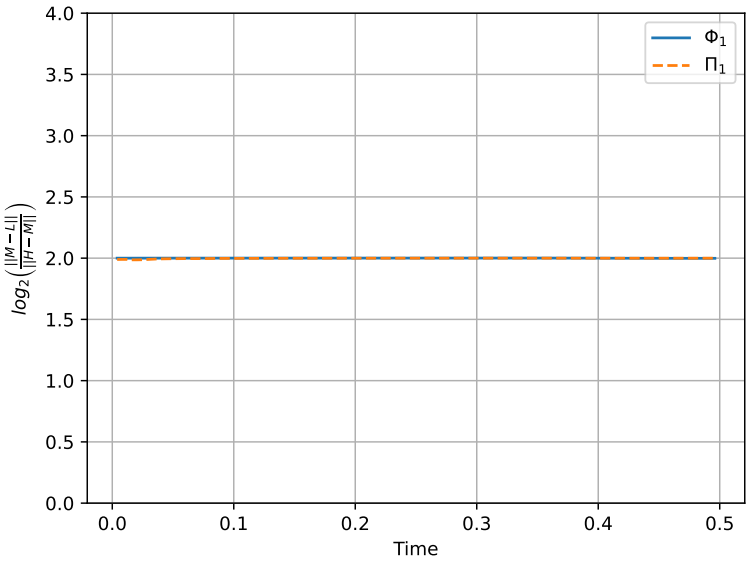

Figure 2.6: Norm convergenge plot for model 3 from Section 2.2.5 for the variables Φ_1 (continuous blue line) and Π_1 (dashed orange line) for the choice $A_3 = B_3 = 1$ and at the critical amplitude $a = -\sqrt{2}$ as an illustrative example.

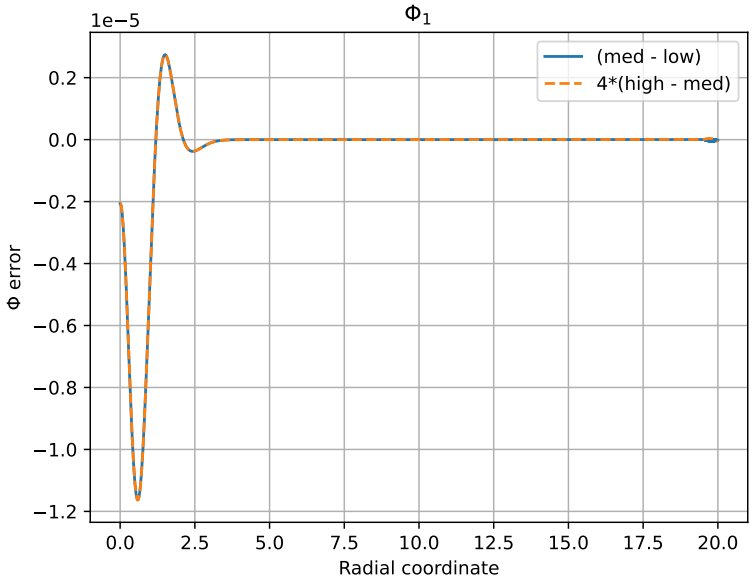

Figure 2.7: Pointwise convergence plot for the variable Φ_1 of model 3 for the choice $A_3 = B_3 = 1$, at time $t \sim 0.496$ and for the critical amplitude $a = -\sqrt{2}$. The continuos blue line is the error of Φ_1 for the runs with medium and low resolution, and the dashed orange line for the runs with high and medium resolution multiplied by 4 for a comparable scaling.

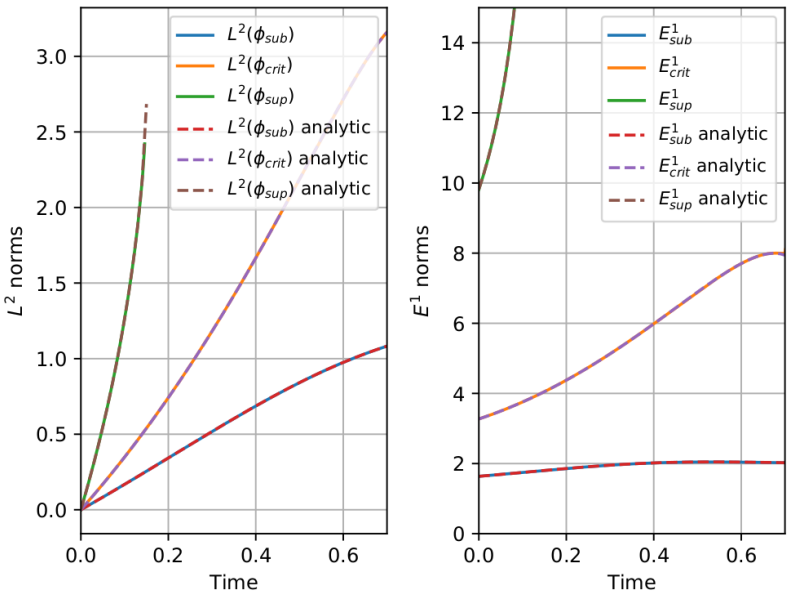

Figure 2.8: L^2 and E^1 for model 1 for subcritical, critical and supercricital data computed from the numerical simulations and the exact solution for model 1 with $A_1 = -1$. The numerical data agree extremely well with the values computed from the exact solution. This indicates that, with suitable care, numerical evolutions can be of real value in determining regularity even at blowup.

2.4.3 *CSS and L^∞ blowup*

2.4.3.1 *Model 1*

The equations of motion for the auxiliary fields are,

$$\begin{aligned} \partial_t \Phi &= \partial_r \Pi\,, \\ \partial_t \Pi &= \partial_r \Phi + \tfrac{2}{r}\Phi + A_1\left(\Phi^2 - \Pi^2\right). \end{aligned} \tag{2.96}$$

and at the outer boundary

$$\partial_t \Pi \mathrel{\hat{=}} -\partial_r \Pi, \tag{2.97}$$

where $\mathrel{\hat{=}}$ refers to the equality only at the boundary. Modulo boundary effects which are negligible in the present study, it is possible to write down closed form solutions for this model, so numerical work constitutes only a code-test. But such work can be highly valuable as it may give confidence in purely numerical studies and highlight algorithmic shortcomings. As observed in section 2.3 this model is an example with approximately CSS threshold behavior. All blowup solutions, including those at the threshold, explode in L^∞, but nevertheless *may* remain finite in L^2 and even in the energy norm E^1. At the threshold solutions are finite in E^1, whereas generically blowup solutions explode in E^1. An important question, therefore, is how well numerical methods can cope with data at these varying levels

of regularity. Pessimistically one might expect that with standard methods when the solution explodes pointwise, the numerical error becomes large so fast that any approximation to L^2 (and so forth) from the numerical data also diverges. Investigating this, it is shown for example in Fig. 2.8, and it was found that the numerics capture the expected behavior well. To quantify the agreement up to blowup, one can observe that in the supercritical data plotted there the blowup occurs at $t \simeq 0.14603$. The numerical evolution was made with a grid-spacing $h = 0.0025$, and the last output is made at $t \simeq 0.146$. At that time the approximation to the L^2 norm is good to about one part in 10^4. In the future, it may be useful to examine the same question for models that have different regularity at blowup, for example by using the parameterized compactification (2.58).

2.4.3.2 *Model 2*

The equations of motion for the reduction variables are

$$\begin{aligned}
&\partial_t \Phi_1 = \partial_r \Pi_1 \,, \qquad \partial_t \Phi_2 = \partial_r \Pi_2 \,, \\
&\partial_t \Pi_1 = \partial_r \Phi_1 + \tfrac{2}{r}\Phi_1 + A_2 \left(\Pi_2^2 - \Phi_2^2\right) \,, \\
&\partial_t \Pi_2 = \partial_r \Phi_2 + \tfrac{2}{r}\Phi_2 + B_2 \left(\Pi_1^2 - \Phi_1^2\right) \,.
\end{aligned} \tag{2.98}$$

At the outer boundary it is imposed

$$\partial_t \Pi_1 \mathrel{\hat{=}} -\partial_r \Pi_1 \,, \qquad \partial_t \Pi_2 \mathrel{\hat{=}} -\partial_r \Pi_2 \,. \tag{2.99}$$

Several families of initial data were evolved and tuned to the threshold of blowup, but here a representative example is discussed, for which the initial data

$$\begin{aligned}
&\Phi_1(0,r) = \Phi_2(0,r) = 0 \,, \\
&\Pi_1(0,r) = \tfrac{2}{5} e^{1/2-r^2} \,, \quad \Pi_2(0,r) = a e^{1/2-r^2} \,.
\end{aligned} \tag{2.100}$$

Experiments choosing the parameters A_2 and B_2 were carried out, but the qualitative behavior of the solutions does not change. Recall that choosing $A_2 = B_2 = A_1$ and setting $\phi_1 = \phi_2$ solutions of model 1 are recovered, making this choice of the parameters is an interesting point to investigate in more detail. In Fig. 2.9 this is done by plotting the logarithm of the maximum of the time derivative of the scalar field at the origin $(\Pi_1(t,0)_{\max}, \Pi_2(t,0)_{\max})$ against the logarithmic distance to the critical point $a_\star$ together with their respective linear least-squares regressions. Note that hereafter a is the only parameter in each family of solutions and $a_\star$ refers to its critical value in each case. Note that there are two lines, one red and one green, but near the threshold, they perfectly overlap and give, as a result, the figures mentioned above. Interestingly, in fact, it was found that for any strong data, with $A_2 = B_2$, the two sets (ϕ_1, Φ_1, Π_1) and (ϕ_2, Φ_2, Π_2) miraculously coincide, and so in fact threshold solutions agree with those of model 1.

This behavior is shown in the bottom panel of Fig. 2.9. Scaling shows that if $A_2 B_2 > 0$ then,

$$A_1^{-1}(A_2 B_2^2)^{1/3}\phi_1\,, \qquad A_1^{-1}(A_2^2 B_2)^{1/3}\phi_2\,, \tag{2.101}$$

solve the same model with fresh constants $A_2' = B_2' = A_1$. This is of course borne out in these simulations. The numerical evidence therefore strongly suggests that all spherical threshold solutions can be constructed directly from model 1. The conclusion is that model 2 does indeed have a unique critical solution in spherical symmetry. Given this, it is perhaps not surprising that experiments indicate the same level of regularity in L^2 and E^1 for this model as seen in Fig. 2.10 as for model 1 in Fig. 2.8 for subcritical, critical and supercritical initial data.

2.4.4 *DSS models and their blowup*

2.4.4.1 *Model 3*

The equations of motion for the third model,

$$\begin{aligned}
\partial_t\phi_1 &= \Pi_1\,, \qquad \partial_t\phi_2 = \Pi_2\,,\\
\partial_t\Phi_1 &= \partial_r\Pi_1\,, \quad \partial_t\Phi_2 = \partial_r\Pi_2\,,\\
\partial_t\Pi_1 &= \partial_r\Phi_1 + \tfrac{2}{r}\Phi_1 \quad + A_3^{-2}(\phi_1 + A_3\phi_2)[\Phi_1^2 + \Phi_2^2 - \Pi_1^2 - \Pi_2^2]\,,\\
\partial_t\Pi_2 &= \partial_r\Phi_2 + \tfrac{2}{r}\Phi_2 \quad + A_3^{-2}(\phi_2 - A_3\phi_1)[\Phi_1^2 + \Phi_2^2 - \Pi_1^2 - \Pi_2^2]\,,
\end{aligned} \tag{2.102}$$

are supplemented with the corresponding boundary conditions,

$$\partial_t\Pi_1 \mathrel{\hat{=}} -\partial_r\Pi_1 - \tfrac{1}{r}\Pi_1\,, \quad \partial_t\Pi_2 \mathrel{\hat{=}} -\partial_r\Pi_2 - \tfrac{1}{r}\Pi_2\,. \tag{2.103}$$

These boundary conditions are modified with respect to those of the previous models simply to avoid code crashes, but in all applications, nevertheless, the boundary is kept causally disconnected from the region at the center, which is an actually interesting one. Like in model 1 the analytical solutions are known, so again this is mainly a code-test. In this spirit, in Fig. 2.11 it is shown again the logarithm of the maximum of the time derivative $\Pi_1(t,0)_{\max}$ against the logarithmic distance to the critical point for a representative family of initial data given by

$$\begin{aligned}
\phi_1(0,r) &= 0\,, & \phi_2(0,r) &= 1\,,\\
\Phi_1(0,r) &= 0\,, & \Phi_2(0,r) &= 0\,,\\
\Pi_1(0,r) &= ae^{1/2-r^2}\,, & \Pi_2(0,r) &= 0\,,
\end{aligned} \tag{2.104}$$

in this instance using $A_3 = 1$. In all the studied cases one clearly observes the expected DSS behavior, which manifests as a straight line plus a periodic wiggle whose period depends on the value of A_3, as

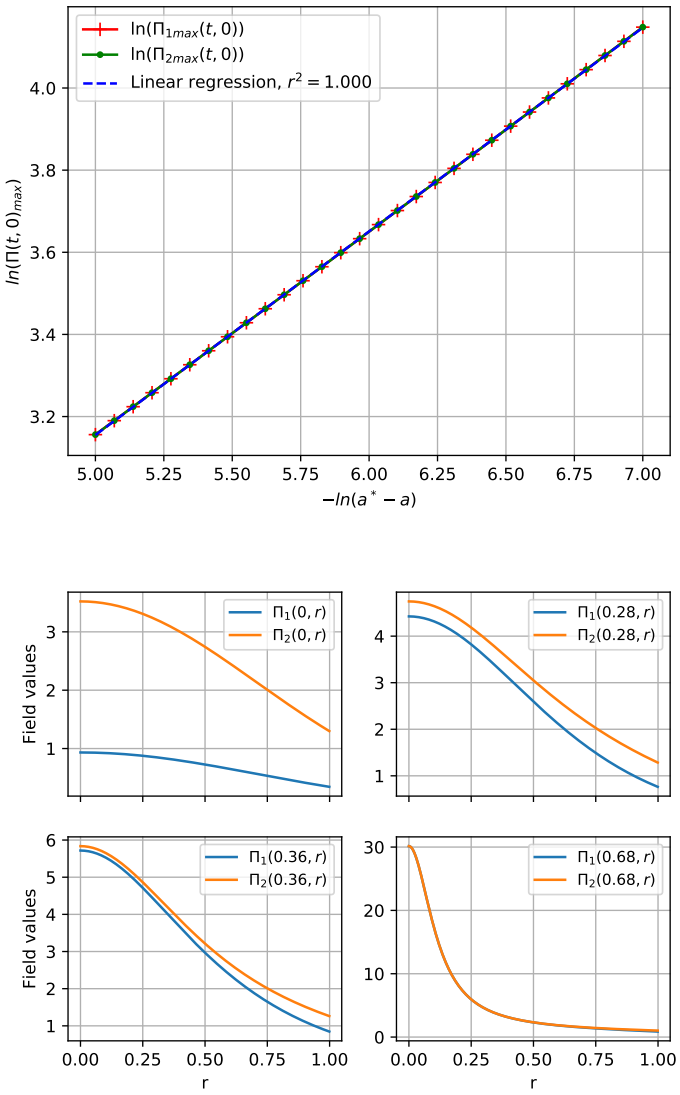

Figure 2.9: In the top panel the scaling law obtained close to the threshold by taking the maximum of the time derivatives of the evolved fields ϕ_1, ϕ_2 for Model 2 is plotted. The chosen parameters are $A_2 = B_2 = -1$, and initial data is as stated in Eq. 2.100. The threshold amplitude $a_\star = 1.5103468$ was obtained by numerical bisection. In the legend r^2 refers to the square of the Pearson correlation coefficient, which is computed using the `Scipy Python` library [86]. A best fit on the data at this resolution returns the gradient 0.49594 with standard error 0.00018. On the bottom, snapshots of the same fields close to blowup for the threshold solution itself are plotted. Observe that the fields lie on top of each other at late times, indicating that the threshold solution is in fact described by the same critical solution of model 1. Identical results are obtained with other families of initial data.

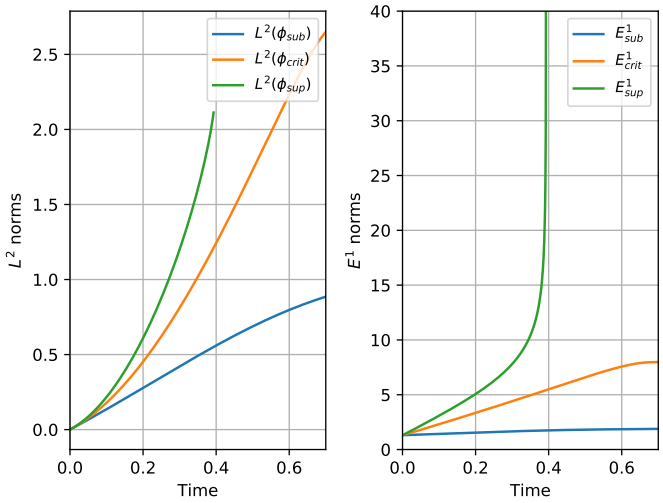

Figure 2.10: L^2 and E^1 for model 2 for subcritical, critical and supercricital data computed from the numerical simulations with $A_1 = B_1 = -1$. For this choice of the parameters the qualitative behavior agrees with Fig. 2.8

.

this constant appears inside the periodic function. Regarding regularity, recall that this model actually has a similar behavior as model 1. Although the solution itself never diverges, first derivatives are divergent for any blowup solution. Solutions are always finite in L^2. At the threshold E^1 is finite, but for all other blowup solutions it diverges. This and its comparison with the numerical result is shown in Fig. 2.12, which agrees perfectly well. The result is similar to the ones obtained for models 1 in Fig. 2.8 and for model 2 in Fig. 2.10, however, now the L^2 norm remains always finite, as expected.

2.4.4.2 *Model 4*

Remember that model 4 from Section 2.2.6 is thought as an extension of model 3 in which the constraint $\phi_1^2 + \phi_2^2 = A_3$ is violated. The equations of motion are

$$\begin{aligned}
\partial_t\phi_1 &= \Pi_1\,, \qquad \partial_t\phi_2 = \Pi_2\,,\\
\partial_t\Phi_1 &= \partial_r\Pi_1\,, \quad \partial_t\Phi_2 = \partial_r\Pi_2\,,\\
\partial_t\Pi_1 &= \partial_r\Phi_1 + \tfrac{2}{r}\Phi_1 \quad + A_4^{-2}(\phi_1 + A_4\phi_2)[\Phi_1^2 + \Phi_2^2 - \Pi_1^2 - \Pi_2^2]\,,\\
\partial_t\Pi_2 &= \partial_r\Phi_2 + \tfrac{2}{r}\Phi_2 \quad + B_4^{-2}(\phi_2 - B_4\phi_1)[\Phi_1^2 + \Phi_2^2 - \Pi_1^2 - \Pi_2^2]\,.
\end{aligned} \tag{2.105}$$

In this case, the two scalar fields of the model are not, *a priori*, related to each other because solutions do not arise from a deformation of the wave equation. In Fig. 2.13 the logarithm of the maximum of the time derivative $\Pi_1(t,0)_{\max}$ against the logarithmic distance to the critical

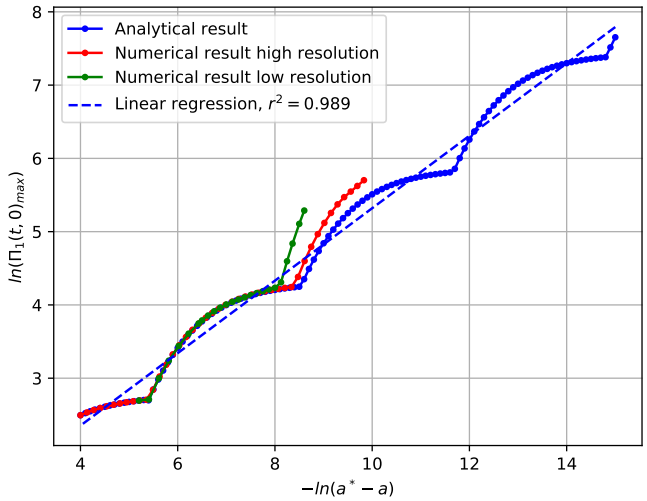

Figure 2.11: Scaling plot for $\Pi_1(t,0)_{\max}$ for model 3 with $A_3 = 1$ for the family of initial data of Eq. 2.104. The threshold amplitude for this family is $a_\star = -\sqrt{2}$. For comparison, the analytic result is also given. The drift between the numerical and analytic curves is caused by numerical error, but does converge away with resolution, as can be understood from the higher resolution data. In the legend r^2 again refers to the square of Pearson correlation coefficient, which was computed from the lower resolution data and is close to unity. Linear regression on the numerical data gives the gradient 0.4945, with standard error 0.0049, close to the expected value $1/2$ seen in Sec. 2.3.

point is plotted. One can observe that this model, despite violating the constraint and not coming from a deformation of the wave equation, exhibits DSS behavior too. In this particular plot $A_4 = B_4 = 1$ were chosen, and the family of initial data,

$$\begin{aligned} \phi_1(0,r) &= 0\,, & \phi_2(0,r) &= \tfrac{1}{2}\,, \\ \Phi_1(0,r) &= 0\,, & \Phi_2(0,r) &= 0\,, \\ \Pi_1(0,r) &= ae^{1/2-r^2}, & \Pi_2(0,r) &= 0\,. \end{aligned} \tag{2.106}$$

tuned to the threshold $a_\star = -2.4122175$ by numerical bisection. In this case, as in model 3, one can regulate the period by choosing the value of A_4 and B_4, as one can see in Fig. 2.14. As choosing different constants would make different models to be solved, having different periods is not in contradiction. An interesting fact that arose experimentally is that comparing the values of the constants from 2.14 and the new critical amplitudes, it turns out that when choosing $A_4 = B_4 = 1/3$, the new critical amplitude is three times the one when the constants are equal to the unit. Same for the case in which $A_4 = B_4 = 2$, where the new critical amplitude is the half of the $A_\star$ corresponding to $A_4 = B_4 = 1$. It was also experimentally found that

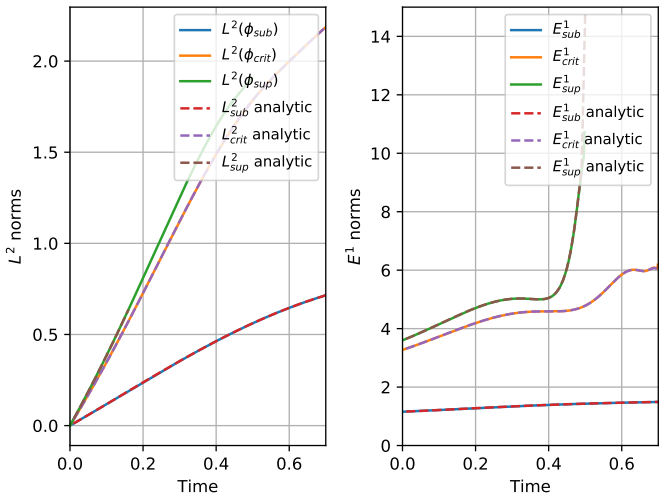

Figure 2.12: L^2 and E^1 for model 3 for subcritical, critical and supercricital data computed from the numerical simulations and the exact solution for model 3 with $A_1 = 1$. The numerical data agree extremely well with the values computed from the exact solution. In this case, the L^2 norm remains always finite.

the period of the superimposed wiggle in the scaling relation also depends on the constants A_4 and B_4. See Fig. 2.14. This behavior was also experimentally found for model 3, and although intuitively it should be an analytical relation, it is not computed in this manuscript.

Similar to model 2, close to the threshold it is possible to observe that, at least for the families of data that were tested, the "constraint" is in fact small close to criticality. Similar behavior is observed for any blowup solution, but it is most pronounced at the threshold. This is illustrated in the second plot of Fig. 2.13. Note, however, that this behavior is not as striking as in model 2, where the "constraint" seems identically satisfied over an entire region, rather than just being small as in this case. Concerning regularity, at the threshold the raw fields ϕ_1 and ϕ_2 remain finite (and thus the solution remains finite in L^2), but as shown in the discussion above first derivatives do explode. This data suggest that the energy norm E^1 is finite at the threshold but diverges for supercritical solutions (see Fig. 2.15), in agreement with model 3. Having examined several different families of initial data, the numerical evidence again suggests that in spherical symmetry model 4 has a unique critical solution in the same sense as the other models.

2.5 CONCLUSIONS AND CLOSING OF THE CHAPTER

The cosmic censorship conjectures are perhaps the most important open problems in strong-field gravity. In looking for evidence either

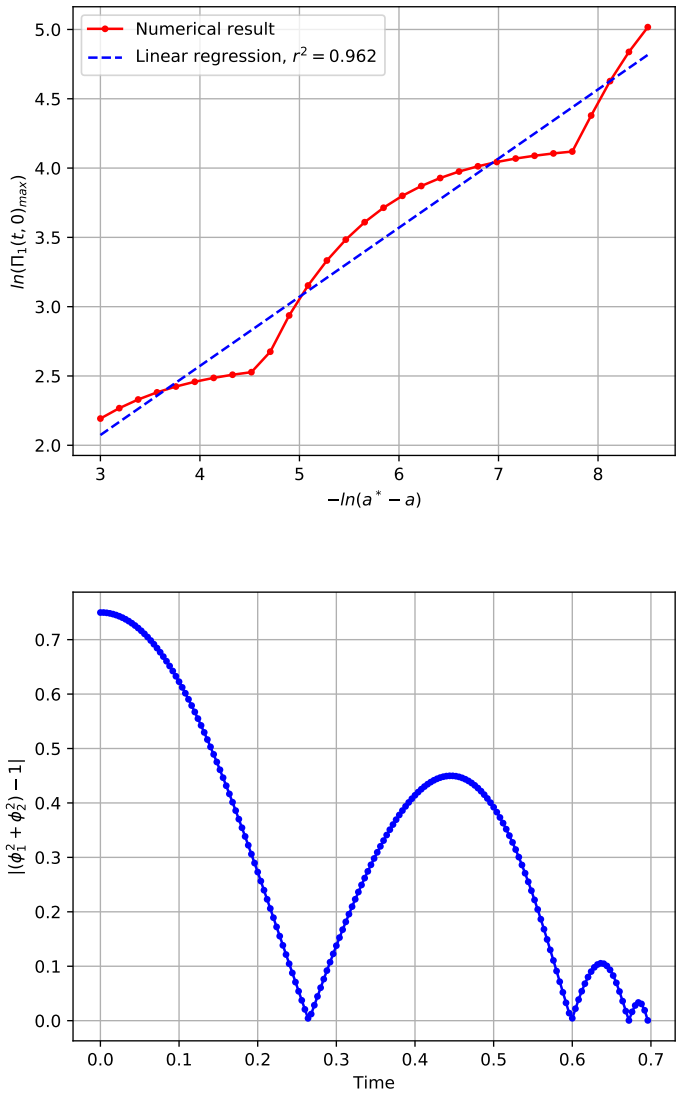

Figure 2.13: Representative plots obtained with model 4 with $A_4 = B_4 = 1$ and the initial data family of Eq. 2.106. This is obtained with $a_\star \simeq -2.4122$. On the top panel, it is shown the now familiar scaling plot for Π_1. As in model 3 the curve looks like a straight line plus a periodic wiggle, indicating that this is a DSS regime. Linear regression on the numerical data gives a slope 0.499, with standard error 0.019. On the bottom panel, the maximum of the absolute value at the origin of the quantity that serves as a constraint in model 3 is plotted. In fact, this quantity is small in a neighborhood around the origin, so that near the threshold, solutions of model 4 are close to solutions of model 3.

for or against them it is imperative to examine extreme regions of the solution space. Combining such considerations with numerical approximation, critical phenomena in gravitational collapse have been discovered. The standard picture of critical collapse is that, considering

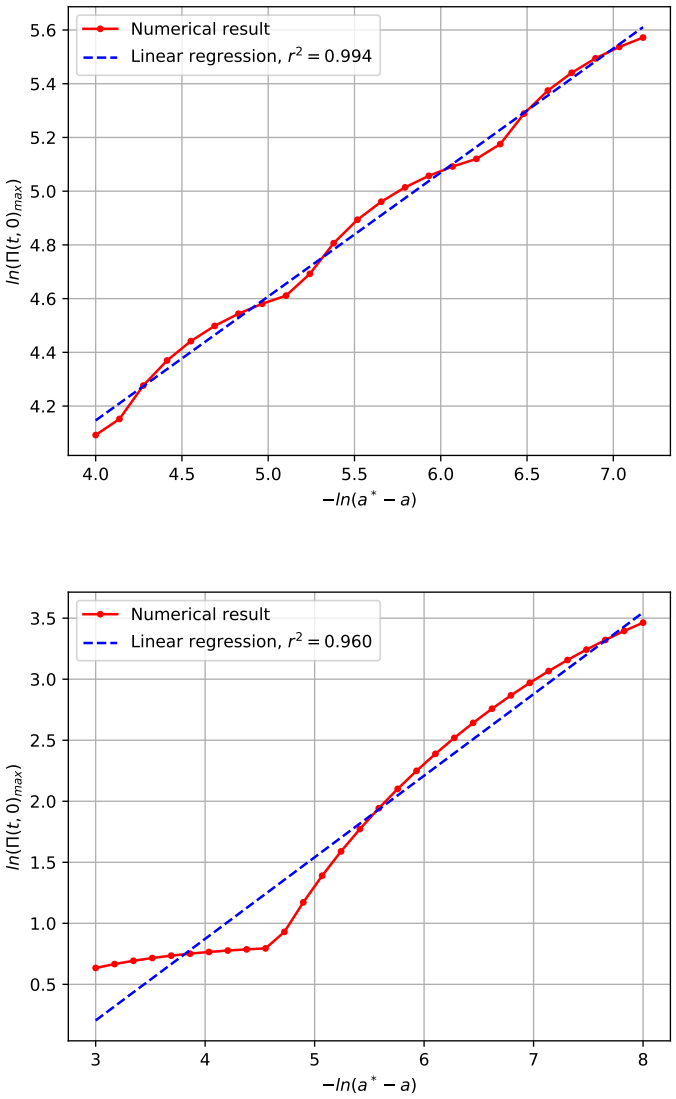

Figure 2.14: Representative plots of the scaling of Π_1 obtained with model 4 and their linear regressions. Linear regression on the numerical data gives a slope 0.461, with standard error 0.0076. On the top panel $A_4 = B_4 = 1/3$ and the initial data family of Eq. 2.106. This is obtained with $a_\star \simeq -7.2366$. The bottom panel corresponds to $A_4 = B_4 = 2$ with the same initial data and with $a_\star \simeq -1.2061$. Linear regression on the numerical data gives a slope 0.668, with standard error 0.026. As in model 3 and in Fig. 2.13 the curve looks like a straight line with a wiggle of different periods, indicating that this is still a DSS regime and that the parameters of the model regulates the period. Note that the differences in the slopes when doing the linear regression are due to the lack of enough periods to have a far fitting. This might be achieved with better and more accurate simulations that would require more computing resources.

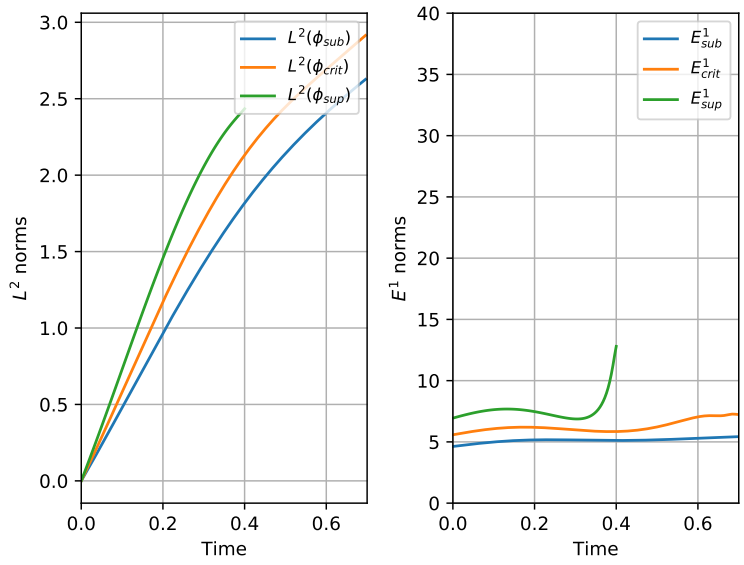

Figure 2.15: L^2 and E^1 for model 4 for subcritical, critical and supercricital data computed from the numerical simulations with $A_1 = B_1 = 1$. In this case, the L^2 norm remains always finite, as in Fig. 2.12.

any one-parameter family of initial data and tuning that parameter to the threshold of BH formation, then as it heads towards blowup the resulting threshold solution will approximate ever more closely, in the strong-field region, a unique self-similar *critical* solution which has a naked singularity. In suitable coordinates data within the family, but close to the threshold, approach the critical solution for some time interval $\sim -\gamma^{-1} \log |a - a_\star|$ before either dispersing or collapsing, with γ a universal parameter independent of the particular family. Examining solutions parametrically in a neighborhood of the threshold reveals that the curvature scalars, BH masses and so forth display power-law behavior, with power γ, in $a_\star - a$.

In spherical symmetry numerical evidence in favor of this picture is pristine, and there is even a proof [82] that the Choptuik critical solution, with the posited DSS, exists. Part of this phenomenology remains robustly without symmetry, but cracks have appeared in the picture. Prominent examples are given by the variability of the scaling parameters and apparent contradiction of uniqueness of the critical solution in scalar field collapse when large aspherical perturbations are present [62, 65], the seeming absence of a unique self-similar critical solution in the collapse of the electromagnetic fields [67, 68] and the consistent challenge in treating threshold solutions in vacuum gravity [34, 51, 57, 58] and so in recovering the results of [49]. In all of these cases however, the edge of what is possible with present numerical methods is close, so there are arguments against adjusting the standard picture until numerical error could be reliably controlled.

The present study is, therefore, a way to side-step these difficulties by constructing the absolute simplest *school-boy* model that could capture the qualitative behavior of interest. The presented models are based on a trick of Nirenberg, admit a small-data global existence result, and in most cases can be solved analytically, making interpretation of threshold solutions unambiguous, regardless of symmetry. These are referred to as deformation models in this manuscript. In contrast with earlier models, they also have the advantage, at least from the point of view of gravitation, that their nonlinearity appears in first derivatives of the fields, just as in GR nonlinearities are of the form of a linear combination of "Γ^2". To the best of my knowledge, here it is also the first such model that admits DSS solutions. (Other examples with such solutions are known [87] but require a large number of fields). Although the models can be reformulated in a natural way that introduces a non-trivial spacetime metric, they are nevertheless fundamentally tied to the flat-metric, and so should not be thought of as a model for WCC. Rather, at best one can hope to capture the properties required for SCC in terms of regularity at blowup and of course those of critical collapse. To summarize the findings of this Chapter, let us split them in the following three categories.

2.5.1 *Spherical symmetry*

Restricting to *pure* spherical symmetry, the obvious analog of the standard picture of critical collapse was completely vindicated for all of the presented models, regardless of how they arose. For the deformation models, simple Taylor expansion shows that generically *at most* one number from the initial data survives to parameterize the threshold solution near the blowup point. In fact there is a measure-0 special case in which this parameter vanishes, but this has not been investigated in detail. In this work this one-parameter family of Taylor expanded threshold solutions is *defined* to be the critical solution. In that one parameter remains, it is unique in the same sense the Schwarzschild is the unique static vacuum solution. Extracting this parameter in any numerical setup seems impractical, however. For models that do not arise as a deformation of the wave equation, the spherical setting was treated numerically and evidence compatible with this picture was found. With either type of model it is found that universal power-law behavior, for example in the maximum of any divergent field quantity, like the energy density, was manifest. This was shown analytically for the deformation models. Moving on to consider small aspherical perturbations, to avoid having to perform more costly numerics only the deformation models are studied. One finding was that the critical amplitude remains fixed, and that the blowup itself is still dominated by the lowest spherical harmonic. This is a simple consequence of the fact that aspherical partial wave solutions all vanish

at the origin. Nevertheless the asymptotic threshold solution, which maintains the scale-symmetry from the spherical setting, is deformed as perturbations are added, perhaps in contradiction expectations, so that a larger number of parameters are needed for its description. Power-law scaling in this regime, both in the physical and phase space pictures, also remains universal. The agreement with the standard picture of critical collapse in the regime in which numerical results are unambiguous, is striking. This gives the confidence that these models do capture qualitatively the phenomena of interest, and potentially do have predictive power for GR.

2.5.2 *Strong cosmic censorship*

As mentioned at the beginning of this Chapter, the SCC conjecture might be thought of as the requirement that for generic initial data the resulting solution, when maximally extended, is unique. In the context of blowup, typically in the context of BH interiors as in [88, 89], this is taken to mean that at a Cauchy horizon, or more generally in the limit towards any the end-point of any incomplete geodesic, the metric should lose enough regularity that the solution can not be extended beyond the blowup. If this fails to be the case, perhaps by choosing fresh data at the singular surface, one may obtain many inequivalent extensions and so violate global uniqueness. The specific requirement in GR [48] is that there exist no coordinates in which the Christoffel symbols are locally L^2. The natural analog for the presented models is the requirement that, at blowup, solutions explode in the energy norm E^1. The conclusion from these models is that for each type of model there exists a direct, specific, relationship between the physical and phase space power-law parameters ν and γ, and the regularity of data at blowup. It was found that threshold solutions are more regular than generic blowup solutions, and so depending on the values of these parameters solutions could be extended beyond the blowup point. This was not investigated in detail in here, and this result may have no *direct* counterpart in GR, but if it does it will permit numerical simulations a new say on SCC in a variety of scenarios.

2.5.3 *The threshold of blowup*

The departure from the standard picture of critical phenomena emerges when considering either aspherical deformations of spherical threshold solutions or general threshold solutions. So far, from the experimental point of view, the presented results in this Chapter are compatible with the numerical results in GR. First, power-law scaling persists both in physical space near the blowup point, and also in phase space as the threshold is approached. In GR there is evidence, in scalar field collapse, that power-law rates deviate from their values in spherical

symmetry as large asphericity appears [62, 65] so this is a possible difference to the models. That said, it is not obvious that the available numerical data are sufficiently fine-tuned to recover the limiting rates, and the interactions of multiple fields complicate the interpretation. If spherical data for the models are perturbed by a sufficiently large asphericity, blowup occurs away from the origin, with the solution appearing very differently than the spherical critical solution in the past light cone of the blowup point, in contradiction with the expectation that there exist a unique *critical solution* in the general setting. This may manifest, for example by the formation of multiple nonspherical centers away from the origin. The latter has been observed in GR in both scalar field [62, 65] and vacuum collapse [58]. As illustrated in Fig. 2.4 blowup can even occur on curves rather than points, an important possibility to be investigated in the gravitational context and what motivates the choice of the initial data in Chapter 4 further in this manuscript. Depending on the model, general threshold solutions may exhibit self-similarity, but require several parameters to describe them as they approach blowup. In GR, by analogy, the existence of a single critical solution would be a red-herring in general. Instead, the threshold of collapse should be characterized by power-law scaling, and, crucially, additional regularity with respect to general blowup solutions. Recalling that some of the models display these features, but do not satisfy the formal definition of self-similarity at the threshold, and the lack of *exact* self-similarity in nonspherical numerical work for GR, one can conjecture that in the past light cone of a blowup point, threshold solutions in GR can still be described by a finite number of parameters. In this way, one can still use the language *critical solution*, but that solution must now be thought of as a parameterized family, whose specific nature is, for now, uncertain.

2.5.4 *Final comment and future work*

The work done in this Chapter shows that in these models, when departing from spherical symmetry, some of the understanding about the standard picture of critical phenomena needs to be changed. A priori, there is no reason why these features should not be translated into GR, despite its more complicated nature. This work, therefore, leaves some open doors to further investigate. First, as a direct follow up, it is highly desirable to develop tools that allow to study the models without symmetry restrictions numerically and check whether or not the solution space of GR exhibits the same properties. Moreover, regarding these models, it is still a question if it can be rigorously proven, without using the exact solutions, the properties of the solutions that are not covered in here and satisfactory explain what are the structural conditions that determine either CSS or DSS at the threshold. So far, it is only possible to speculate that it has to do with the

factor attached to the nonlinearity, but this is, however, pure intuition. The final comment for future work is that as these models have the shortcoming of being purely semilinear, no notion of BH formation is possible. Hence, developing other more sophisticated models that avoid this is still remaining in the possible paths that can follow this manuscript.

Part II

GRAVITATIONAL WAVES IN VACUUM

3

COMPARISON OF LINEAR BRILL AND TEUKOLSKY WAVES

As seen in the introduction in Sections 1.3.1 and 1.5, understanding critical phenomena in gravitational collapse becomes more complicated once one drops spherical symmetry. In this scenario, the natural question is to ask what happens with GWs in vacuum, since they resemble pure gravity and since there are no spherical dynamical GWs. The first attempt to evolve such a setting was done by Abrahams and Evans [49], where the authors were using what is called Teukolsky waves [90] to explore the critical phenomena of GWs in vacuum. However, and despite numerous other attempts (see Table 1.1) reproducing their results has proven difficult. Some of these issues might be purely numerical, nevertheless, other features could be inherent from the lack of spherical symmetry [69].

To study the collapse of GWs in vacuum different authors use different types of initial data, being these divided between Brill [91] and Teukolsky waves [90]. The former are used in the recent studies [58, 60] and in Chapter 4 of this manuscript. The latter are used (together with Brill waves) in [51]. For Brill waves it is only necessary to solve one elliptic equation whose solution provides a nonlinear vacuum solution to Einstein's constraint equations. On the other hand, Teukolsky waves are quadrupolar, linear perturbations of Minkowski spacetime which can be "dressed up" in different manners to yield nonlinear solutions to the Einstein constraint equations. It is important to notice that both, Brill and Teukolsky waves, have their seed function, for which many authors choose Gaussian profiles, letting some freedom in the choice of the initial data.

Many authors have claimed that the numerical behavior of Brill and Teukolsky waves is different, even compromising numerical stability in the case of the first ones. In [51] they report that the most difficult families to tune towards criticality were the Brill wave families, finding the numerical stability as the limit to their bisection search. The authors of [57] wonder, literally, why it is so difficult to evolve Brill wave data. In my personal experience with `bamps` (see Chapter 4), in agreement with [51], the limiting factor when evolving Brill waves is, in some sense, numerical stability together with the peculiar shapes of the AHs. Moreover, it is needed to say that both [51] and Chapter 4 conclude

that different families of initial data lead to different scaling exponents γ and therefore, presumably, different threshold solutions. More detail about these two types of initial data will be given in Sections 3.1.1 and 3.1.2.

Among the attempts to understand the critical phenomena beyond spherical symmetry there are the studies [67] and [68] where the critical gravitational collapse of electromagnetic waves is investigated. In this case, the initial data are linear by construction as an electromagnetic spherical wave of a given multipole ℓ is adopted at a moment of time symmetry and then used to solve Einstein's equations. It might be expected that the different nonlinearities of Einstein's equations coupled to the different multipoles, however, it is expected that the evolution is dominated by the linear "seed" data. These studies conclude that initial data for different multipoles yield qualitatively different threshold solutions, threatening the uniqueness of the critical solution. Let us take, as an illustrative example, the dipole data with $\ell = 1$. In this case in [67] a unique center of collapse, at the origin, was found. In contrast, for quadrupole data $\ell = 2$, in [68] two separate centers of collapse along the symmetry axis were found, in agreement with [58], [51] and Chapter 4.

The last observation suggests an explanation for the different behavior of Brill and Teukolsky waves as they have, a priori, different multipole moments. These multipole moments would couple to different parts of Einstein's equations giving different results as it happens with the critical gravitational collapse of electromagnetic waves. As electromagnetic waves are linear, in the sections below analytical linear solutions of brill waves are compared directly with Teukolsky waves in three different ways: i) Comparing the data by transforming the Brill waves to the Transverse-Traceless (TT) gauge, ii) by computing the gauge-invariant Moncrief function for the different multipoles and iii) by computing the respective Kretschmann scalars.

3.1 LINEAR GRAVITATIONAL WAVE INITIAL DATA

In this section a deeper description of the two types of initial data that are analyzed, Brill and Teukolsky waves, is given, so that the reader can follow and understand the discussion of this Chapter. For more details on the initial data, I suggest the original papers of Brill [91] and Teukolsky [90] together with Chapter 9 of [10] for a textbook explanation of linearized GWs in a notation close to that used here.

3.1.1 *Teukolsky waves*

Teukolsky waves are commonly referred as quadrupolar gravitational-wave solutions to the linearized Einstein's equations (see [92] for a

generalization to higher multipoles). The metric is in the Transverse Traceless gauge (TT), and using natural units $c = 1$ is as follows:

$$\begin{aligned} ds^2 = &-dt^2 + dr^2\left\{1 + Af_{rr}\right\} + r\,drd\theta\left\{2Bf_{r\theta}\right\} + \\ &r\sin(\theta)\,drd\phi\left\{2Bf_{r\phi}\right\} + r^2\,d\theta^2\left\{1 + Cf^{(1)}_{\theta\theta} + Af^{(2)}_{\theta\theta}\right\} + \\ &r^2\sin(\theta)\,d\theta d\phi\left\{2(A-2C)f_{\theta\phi}\right\} + \\ &r^2\sin^2(\theta)\,d\phi^2\left\{1 + Cf^{(1)}_{\phi\phi} + Af^{(2)}_{\phi\phi}\right\}, \end{aligned} \tag{3.1}$$

where the f_{ij} are angular functions for $\ell = 2$ and $m = 0$ listed in the appendix A. The coefficients A, B and C can be constructed from a seed function $F(t, r)$ being a common choice a linear superposition of Gaussians at a moment of time symmetry at $t = 0$:

$$F(t,r) = \mathcal{A}_T\lambda^4\Big((t-r)\,e^{-((r-t)/\lambda)^2} - (r+t)\,e^{-((r+t)/\lambda)^2}\Big), \tag{3.2}$$

The notation in 3.2 is that $\mathcal{A}_T$ corresponds to the amplitude of the wave, λ is a constant with units of length that determines the wavelength. Taking this seed function, $m = 0$ due to the axisymmetry and going through the needed calculations (see Appendix A) the coefficients A, B and C take the following form:

$$A^T = -24\mathcal{A}_T e^{-(r/\lambda)^2}, \tag{3.3a}$$

$$B^T = \frac{8\mathcal{A}_T}{\lambda^2}e^{-(r/\lambda)^2}(2r^2 - 3\lambda^2), \tag{3.3b}$$

$$C^T = \frac{8\mathcal{A}_T}{\lambda^4}e^{-(r/\lambda)^2}(r^4 - 4r^2\lambda^2 + 3\lambda^4), \tag{3.3c}$$

and the metric, evaluated at $t = 0$, becomes

$$\begin{aligned} ds^2 = &-dt^2 + dr^2\Big\{1 + \mathcal{A}_T\left(72\sin^2(\theta) - 48\right)e^{-(r/\lambda)^2}\Big\} + \\ &r^2d\theta^2\Big\{1 + 24\mathcal{A}_T\left(\sin^2(\theta)\left(-\frac{r^4}{\lambda^4} + \frac{4r^2}{\lambda^2} - 3\right) + 1\right)e^{-(r/\lambda)^2}\Big\} + \\ &rd\theta dr\Big\{48\mathcal{A}_T\sin(\theta)\cos(\theta)\left(3 - 2\frac{r^2}{\lambda^2}\right)e^{-(r/\lambda)^2}\Big\} + \\ &r^2\sin^2(\theta)d\phi^2\Big\{1 + 24\mathcal{A}_T\left(\sin^2(\theta)\left(\frac{r^4}{\lambda^4} - \frac{4r^2}{\lambda^2}\right) + 1\right)e^{-(r/\lambda)^2}\Big\}. \end{aligned} \tag{3.4}$$

Earlier before, when beginning this Chapter, it was said that the Teukolsky waves are already linear perturbations of the Minkowski spacetime that later on need to be "dressed up" in order to have nonlinear solutions to Einstein's equations. This means that Teukolsky waves are linear before solving the Hamiltonian and Momentum constraints, which can be done in different ways to have the nonlinear solution. In this case, the metric 3.4 is a vacuum solution at a moment of time symmetry, being the Momentum constraint automatically satisfied. Therefore, only the Hamiltonian constraint needs to be solved

to have nonlinear solutions to Einstein's equations, however in this work, the focus is only on the linear perturbation,

$$h_{ij}^T = \gamma_{ij}^T - \eta_{ij}, \tag{3.5}$$

where γ_{ij}^T is the spatial Teukolsky metric that can be read from 3.4, and η_{ij} is the Minkowski metric. The nonvanishing initial metric perturbations in the TT gauge in spherical polar coordinates are written in the form

$$h_{rr} = Af_{rr}, \tag{3.6a}$$
$$h_{r\theta} = rBf_{r\theta}, \tag{3.6b}$$
$$h_{\theta\theta} = r^2(Cf_{\theta\theta}^{(1)} + Af_{\theta\theta}^{(2)}), \tag{3.6c}$$
$$h_{\phi\phi} = r^2\sin^2\theta(Cf_{\phi\phi}^{(1)} + Af_{\phi\phi}^{(2)}), \tag{3.6d}$$

where the coefficients take the particular expression of 3.3. Please, be aware that now, due to notation purposes, the coefficients are renamed as A^T, B^T and C^T to refer to Teukolsky wave coefficients. This is done in order to avoid future confusions with Brill wave coefficients when analyzed in the gauge transformation of Section 3.2.1.

3.1.2 *Brill waves*

The construction of Brill waves, fully nonlinear, axisymmetric vacuum gravitational-wave initial data [91], is simpler than the construction of Teukolsky data. In this case, the line element in a moment of time symmetry corresponds to

$$\gamma_{ij}dx^i dx^j = \psi^4\left(e^{2q}(dr^2 + r^2d\theta^2) + r^2\sin^2(\theta)d\varphi^2\right), \tag{3.7}$$

where $q = q(r,\theta)$ is the seed function. Many authors choose a Gaussian profile for this function, including Holz *et al.* [93] which gives to this choice the name of "Holz seed function"

$$q(r,\theta) = \mathcal{A}_B r^2\sin^2(\theta)\sigma^{-2}e^{-(r/\sigma)^2} = \mathcal{A}_B\rho^2\sigma^{-2}e^{-(\rho^2+z^2)/\sigma^2}, \tag{3.8}$$

where $\mathcal{A}_B$ is the amplitude of the Brill wave and σ a constant with dimensions of length which is a measure of the wavelength, and ρ corresponds to the cylindrical radial coordinate. However, it is possible to rewrite this seed function expressing the angular part in terms of the spherical harmonics $Y_{00}(\theta,\phi)$ and $Y_{20}(\theta,\phi)$ as

$$q(r,\theta) = q_{00}(r)Y_{00}(\theta) + q_{20}(r)Y_{20}(\theta), \tag{3.9}$$

where

$$q_{00}(r) = \sqrt{\pi}\,\frac{4\mathcal{A}_B}{3}\left(\frac{r}{\sigma}\right)^2 e^{-(r/\sigma)^2} \tag{3.10a}$$
$$q_{20}(r) = -\sqrt{\frac{\pi}{5}}\,\frac{4\mathcal{A}_B}{3}\left(\frac{r}{\sigma}\right)^2 e^{-(r/\sigma)^2}. \tag{3.10b}$$

This simple rewriting might seem trivial at first, however, it is giving some extra information. First of all, only the spherical harmonics with $m = 0$ appear on the expression due to the axisymmetry that naturally comes with the Brill waves, nevertheless, it is noticeable that the only angular component, that depends on θ, is the contribution from $Y_{20}(\theta, \phi)$, which means that this seed function is purely quadrupolar with $\ell = 2$. Teukolsky waves are purely quadrupolar as well, and this seems, at first, a strong indication that for this specific choice of the Holz seed function it might also be the case for the Brill wave. In any case, let us not anticipate and continue with the development of the facts.

Regarding the constraints, the Hamiltonian constraint is the only one that is needed to be solved. Since this is a moment of time symmetry the Momentum constraint is automatically satisfied. The Hamiltonian constraint then takes the form

$$\nabla^2 \psi = -\frac{\psi}{4}\tau, \tag{3.11}$$

where the function $\tau = \tau(r, \theta)$ is given by

$$\tau \equiv \frac{\partial^2 q}{\partial \rho^2} + \frac{\partial^2 q}{\partial z^2} \tag{3.12}$$

and where ∇^2 is the flat Laplace operator. For the specific choice 3.8

$$\tau(r,\theta) = \frac{2\mathcal{A}_B}{\sigma^6} e^{-(r/\sigma)^2} \left(2r^4 - 6r^2\sigma^2 + \sigma^4 - 2r^2(r^2 - 3\sigma^2)\cos^2(\theta)\right). \tag{3.13}$$

Again, the angular part of the function $\tau(r, \theta)$ can be expressed in terms of the spherical harmonics only with a quadrupolar contribution as follows

$$\tau(r,\theta) = \tau_{00}(r)Y_{00}(\theta) + \tau_{20}(r)Y_{20}(\theta) \tag{3.14}$$

where the coefficients take the form

$$\tau_{00}(r) = \sqrt{\pi}\frac{4\mathcal{A}_B}{3\sigma^6} e^{-(r/\sigma)^2} \left(4r^4 - 12r^2\sigma^2 + 3\sigma^4\right) \tag{3.15a}$$

$$\tau_{20}(r) = -\sqrt{\frac{\pi}{5}}\frac{16\mathcal{A}_B}{3\sigma^6} e^{-(r/\sigma)^2} \left(r^4 - 3r^2\sigma^2\right). \tag{3.15b}$$

This is a special case. Usually, the Hamiltonian constraint needs to be solved numerically since there is not an analytical solution. However, since the purpose is the comparison with the already linear Teukolsky waves, considering only the linear part of the solution is sufficient. For this purpose, the conformal factor Ψ is rewritten as

$$\psi = 1 + u, \tag{3.16}$$

and the Hamiltonian constraint in order to be linear in the amplitude $\mathcal{A}_B$ takes the form

$$\nabla^2 u = -\frac{1}{4}\tau. \tag{3.17}$$

The line element becomes, to linear order:

$$\begin{aligned}\gamma_{ij}dx^i dx^j = {} & dr^2 + r^2(d\theta^2 + \sin^2\theta d\varphi^2) + \\ & (4u + 2q)(dr^2 + r^2 d\theta^2) + 4ur^2\sin^2(\theta)d\varphi^2.\end{aligned} \tag{3.18}$$

Now, it is possible to use the Green function $G(\mathbf{r}, \mathbf{r}') = 1/|\mathbf{r} - \mathbf{r}'|$ to write the solution to the linear Hamiltonian constraint

$$u(r, \theta, \varphi) = \frac{1}{16\pi}\int \frac{\tau(r', \theta', \varphi')d^3x'}{|\mathbf{r} - \mathbf{r}'|}. \tag{3.19}$$

It is important to consider the expansion of this Green function in terms of the spherical harmonics, where $r_<$ is the greater and $r_>$ is the smaller of the two radii r and r'

$$\frac{1}{|\mathbf{r} - \mathbf{r}'|} = \frac{4\pi}{r_>}\sum_{\ell,m}\frac{1}{2\ell + 1}\frac{r_<^\ell}{r_>^\ell}Y^*_{\ell m}(\theta', \varphi')Y_{\ell m}(\theta, \varphi). \tag{3.20}$$

Writing everything in terms of the spherical harmonics in 3.19, this is, inserting the expansion 3.20 and the function 3.14 one can find

$$\begin{aligned}u(r, \theta, \varphi) = {} & \frac{1}{4}\int \Big(\tau_{00}(r')Y_{00}(\theta', \varphi') + \tau_{20}(r')Y_{20}(\theta', \varphi')\Big) \\ & \sum_{\ell,m}\frac{1}{2\ell + 1}\frac{r_<^\ell}{r_>^{\ell+1}}Y^*_{\ell m}(\theta', \varphi')Y_{\ell m}(\theta, \varphi)d^3x'.\end{aligned} \tag{3.21}$$

The next step is to write the volume element as $d^3x' = r'^2 dr' d\Omega'^2$ and integrate the angular part using the orthogonality of the spherical harmonics,

$$\int Y^*_{\ell m}(\theta', \varphi')Y_{\ell' m'}(\theta', \varphi')d\Omega'^2 = \delta_{\ell,\ell'}\delta_{m,m'}. \tag{3.22}$$

After this procedure the result is, again, a pure quadrupole for $u(r, \theta)$ as well, that will propagate into the metric as it depends linearly on $u(r, \theta)$,

$$u(r, \theta) = u_{00}(r)Y_{00} + u_{20}(r)Y_{20} \tag{3.23}$$

with

$$u_{00}(r) = \frac{1}{4}\int_0^\infty \frac{\tau_{00}(r')\, r'^2 dr'}{r_>} \tag{3.24a}$$

$$u_{20}(r) = \frac{1}{4}\int_0^\infty \frac{r_<^2\tau_{20}(r')\, r'^2 dr'}{r_>^3}. \tag{3.24b}$$

Please, be aware that due to the existence of $r_<$ and $r_>$, the integrals in 3.24 have to be split into two parts for the cases when r' is smaller or greater than r, for instance

$$u_{00}(r) = \frac{1}{4r}\int_0^r \tau_{00}(r')\, r'^2 dr' + \frac{1}{4}\int_r^\infty \tau_{00}(r')\, r' dr'. \tag{3.25}$$

Now, `Mathematica` [94] is used to carry out the integral, where the coefficients expressed as 3.15 are inserted, arriving at the result

$$u_{00}(r) = -\frac{\sqrt{\pi}}{6\sigma^2}\mathcal{A}_B e^{-(r/\sigma)^2}\left(2r^2+\sigma^2\right) \tag{3.26a}$$

$$u_{20}(r) = -\sqrt{\frac{\pi}{5}}\frac{\mathcal{A}_B}{24r^3\sigma^2}\Big(3\sqrt{\pi}\sigma^5 \mathrm{erf}\left(\frac{r}{\sigma}\right) - 2re^{-(r/\sigma)^2}\left(2r^2\sigma^2+4r^4+3\sigma^4\right)\Big), \tag{3.26b}$$

where the definition of the error function $\mathrm{erf}(z)$ is

$$\mathrm{erf}(z) \equiv \frac{2}{\sqrt{\pi}}\int_0^z e^{-t^2} dt. \tag{3.27}$$

One may wonder if the coefficient $u_{20}(r)$ remains finite when $r \to 0$, nevertheless it is enough to look at the leading-order terms in the Taylor expansion of the error function about $z = 0$

$$\mathrm{erf}(z) = \frac{2}{\sqrt{\pi}}\left(z - \frac{z^3}{3}\right) + \mathcal{O}(z^5), \tag{3.28}$$

to realise that, indeed, $u_{20}(r)$ remains finite.

To finish assembling the metric, it is needed to insert 3.9 and 3.23 in the line element 3.18. Here it is possible to read the spatial metric γ^B_{ij}, however, the focus is again in the wave perturbation

$$h^B_{ij} = \gamma^B_{ij} - \eta_{ij}, \tag{3.29}$$

that in explicit form reads as

$$h_{rr} = \frac{\mathcal{A}_B}{8r^3\sigma^2}\Big(-\sqrt{\pi}\sigma^5\left(3\cos^2(\theta)-1\right)\mathrm{erf}\left(\frac{r}{\sigma}\right) - 2re^{-\frac{r^2}{\sigma^2}}\left(\cos^2(\theta)\left(-2r^2\sigma^2+4r^4-3\sigma^4\right)+2r^2\sigma^2-4r^4+\sigma^4\right)\Big), \tag{3.30a}$$

$$h_{\theta\theta} = \frac{\mathcal{A}_B}{8r\sigma^2}\Big(-\sqrt{\pi}\sigma^5\left(3\cos^2(\theta)-1\right)\mathrm{erf}\left(\frac{r}{\sigma}\right) - 2re^{-\frac{r^2}{\sigma^2}}\left(\cos^2(\theta)\left(-2r^2\sigma^2+4r^4-3\sigma^4\right)+2r^2\sigma^2-4r^4+\sigma^4\right)\Big), \tag{3.30b}$$

$$h_{\phi\phi} = \frac{\mathcal{A}_B}{8\sigma^2}\Big(e^{-\frac{r^2}{\sigma^2}}\left(\cos(2\theta)\left(2r^2\sigma^2+4r^4+3\sigma^4\right)-2r^2\sigma^2-4r^4+\sigma^4\right) - \frac{\sqrt{\pi}\sigma^5}{r}\left(3\cos^2(\theta)-1\right)\mathrm{erf}\left(\frac{r}{\sigma}\right)\Big). \tag{3.30c}$$

As a final comment, just to remark that using the Holz seed function 3.8, which appears to be purely quadrupolar, transfers to the metric perturbation that, for this special case, is as the Teukolsky perturbation, a pure $\ell = 2$ mode. This fact makes the comparison between both fairer since the goal is to find what makes the difference in the behavior of Brill and Teukolsky waves during evolution. It is a good sign that the starting point is two sets of initial data that are as similar as possible. Moreover, taking into account that the Holz seed function is a very common choice among the authors, this adds the value of studying what is, probably, the most common option.

3.2 COMPARISONS

In this section, the comparison between linear Brill and Teukolsky waves is made, in particular, in three different ways. Naively, one can try to make a direct comparison of both perturbations at first, noticing that in the case of Brill the component $h^B_{r\theta} = 0$ meanwhile in Teukolsky it does not vanish. However, it is important to be aware that this direct comparison is meaningless since both metrics are expressed in different gauges. This is the reason why the (fair) comparison has to follow a different path, writing both metrics in the same gauge or using an artifact that is gauge-invariant, as the Moncrief formalism that will soon be introduced in Section 3.2.2, or the Kretschmann scalar in Section 3.2.3.

3.2.1 *Gauge transformation*

As the metric of Teukolsy waves is expressed in the TT gauge, in this first section a gauge transformation is carried out to write the Brill waves in TT gauge as well, which, for a purely spatial perturbation h_{ij} it means that

$$\eta^{ij} h_{ij} = 0, \tag{3.31a}$$

$$\partial^j h_{ij} = 0. \tag{3.31b}$$

In order to pursue this gauge transformation, cartesian coordinates are used, meaning $\eta_{ij} = diag(1, 1, 1)$, and that the covariant derivatives associated with η_{ij} become partial derivatives. Let us assume that $h^{B'}_{ij}$ is the Brill wave perturbation in the new gauge, this is in the TT gauge. Then the linearized spatial gauge freedom depends on the one-form generator ξ_i and can be written as

$$h^{B'}_{ij} = h^B_{ij} - 2\partial_{(i}\xi_{j)}. \tag{3.32}$$

Now let us use 3.31b as follows

$$\partial^j h^{B'}_{ij} = 0 \Rightarrow \partial^j \partial_j \xi_i + \partial_i \partial^j \xi_j = \partial^j h^B_{ij}. \tag{3.33}$$

To solve this equation ξ_i is decomposed in the following manner

$$\xi_i = \hat{\xi}_i + \partial_i \varphi \,, \tag{3.34}$$

with

$$\partial^i \partial_i \varphi = \frac{1}{2} h^B \,, \tag{3.35a}$$

$$\partial^j \partial_j \hat{\xi}_i = \partial^j h^B_{ij} - \partial_i h^B \tag{3.35b}$$

where $h^B \equiv \eta^{ij} h^B_{ij}$ is the trace.

Now it is needed to remind the expression for the linearized vacuum Hamiltonian constraint, that both, Brill and Teukolsky waves satisfy:

$$\partial^i \partial^j h_{ij} - \partial^i \partial_i h^k{}_k = 0 \,. \tag{3.36}$$

With this in mind, it is easy to see that the divergence of 3.35b vanishes

$$\partial^j \partial_j (\partial^i \hat{\xi}_i) = \partial^i \partial^j h_{ij} - \partial^i \partial_i h^k{}_k = 0 \,, \tag{3.37}$$

and that, with the suitable boundary conditions, the divergence of $\hat{\xi}_i$ also vanishes everywhere

$$\partial^i \hat{\xi}_i = 0. \tag{3.38}$$

The fact that the divergence of $\hat{\xi}_i$ is also null means that 3.34 is the decomposition of the transverse and longitudinal parts in the Fourier space.

Finally, it is needed to prove that this gauge transformation satisfies the TT conditions 3.31a and 3.31b. In the first place let us take the trace of 3.32

$$h^{B'} = h^B - 2\partial^i \xi_i = h^B - 2\,\partial^i \partial_i \varphi = 0, \tag{3.39}$$

where it is clear that it satisfies the first condition 3.31a of the TT gauge. In second place, let us apply 3.31b to 3.32 and carry out the full computation

$$\begin{aligned} \partial^i h^{B'}_{ij} &= \partial^i h^B_{ij} - \partial^i \partial_i (\hat{\xi}_j + \partial_j \varphi) - \partial^i \partial_j (\hat{\xi}_i + \partial_i \varphi) \\ &= \partial^i h^B_{ij} - \partial^i h^B_{ij} + \partial_j h^B - \partial_j (\partial^i \partial_i \varphi) - \partial_j (\partial^i \hat{\xi}_i) - \partial_j (\partial^i \partial_i \varphi) \\ &= \partial_j h^B - \partial_j h^B = 0, \end{aligned} \tag{3.40}$$

where 3.35a and 3.35b were used.

Once the change of gauge it is clear it is time to carry out the explicit calculation to solve equations 3.35a and 3.35b. Let us start for the first one, which has a very familiar form, resembling 3.17, and consequently it is possible to use the same Green function as before, $G(\mathbf{r}, \mathbf{r}') = 1/\mid \mathbf{r} - \mathbf{r}' \mid$:

$$\varphi = -\frac{1}{8\pi} \int \frac{h^B}{\mid \mathbf{r} - \mathbf{r}' \mid} dx^3. \tag{3.41}$$

It is possible to use again the Green's function expansion 3.20, but this time for the trace of the Brill perturbation

$$h^B = \frac{\mathcal{A}_B}{16r^3\sigma^2}\left(2re^{-\frac{r^2}{\sigma^2}}\left(\cos(2\theta)\left(6r^2\sigma^2-4r^4+9\sigma^4\right)\right.\right. \\ \left.\left.-6r^2\sigma^2+4r^4+3\sigma^4\right)-3\sqrt{\pi}\sigma^5(3\cos(2\theta)+1)\operatorname{erf}\left(\frac{r}{\sigma}\right)\right) \tag{3.42}$$

Using again `Mathematica` [94] to solve this integral, the result might be expressed in terms of the spherical harmonics $Y_{00}(\theta,\phi)$ and $Y_{20}(\theta,\phi)$

$$\varphi = \frac{1}{6}\sqrt{\pi}\mathcal{A}_B\sigma^2 e^{-\frac{r^2}{\sigma^2}}Y_{00}(\theta) \\ + \sqrt{\frac{\pi}{5}}\frac{\mathcal{A}_B\sigma^2}{48r^3}e^{-\frac{r^2}{\sigma^2}}\left(-3\sqrt{\pi}\sigma e^{\frac{r^2}{\sigma^2}}\left(\sigma^2-2r^2\right)\operatorname{erf}\left(\frac{r}{\sigma}\right)\right. \\ \left.-8r^3+6r\sigma^2\right)Y_{20}(\theta), \tag{3.43}$$

or substituting their explicit expression

$$\varphi = \frac{\mathcal{A}_B\sigma^2}{64r^3}\left(-\sqrt{\pi}\sigma\left(3\cos^2(\theta)-1\right)\left(\sigma^2-2r^2\right)\operatorname{erf}\left(\frac{r}{\sigma}\right)\right. \\ \left.-2re^{-\frac{r^2}{\sigma^2}}\left(\cos^2(\theta)\left(4r^2-3\sigma^2\right)-4r^2+\sigma^2\right)\right). \tag{3.44}$$

The next step is to solve the equation for $\hat{\xi}_i$, for which the same procedure is applied but with subtlety. This time the equation is solved for the three Cartesian components, this is for $(\hat{\xi}_x,\hat{\xi}_y,\hat{\xi}_z)$, however, the integration is over the Green function using the spherical polar coordinates. To do this, the Jacobian J is used to transform from the spherical polar coordinates to Cartesian coordinates

$$(\hat{\xi}_x,\hat{\xi}_y,\hat{\xi}_z) = J(\hat{\xi}_r,\hat{\xi}_\theta,\hat{\xi}_\phi), \tag{3.45}$$

where the Jacobian and the inverse Jacobian are written in terms of (r,θ,ϕ)

$$J = \begin{pmatrix} \sin(\theta)\cos(\phi) & \sin(\theta)\sin(\phi) & \cos(\theta) \\ \frac{\cos(\theta)\cos(\phi)}{r} & \frac{\cos(\theta)\sin(\phi)}{r} & -\frac{\sin(\theta)}{r} \\ -\frac{\csc(\theta)\sin(\phi)}{r} & \frac{\csc(\theta)\cos(\phi)}{r} & 0 \end{pmatrix}, \tag{3.46}$$

$$J^{-1} = \begin{pmatrix} \sin(\theta)\cos(\phi) & r\cos(\theta)\cos(\phi) & -r\sin(\theta)\sin(\phi) \\ \sin(\theta)\sin(\phi) & r\cos(\theta)\sin(\phi) & r\sin(\theta)\cos(\phi) \\ \cos(\theta) & -r\sin(\theta) & 0 \end{pmatrix}. \tag{3.47}$$

The right hand side of equation 3.35b in spherical polar coordinates is

$$
\begin{aligned}
(\partial^j h^B_{ij} - \partial_i h^B)_r &= \frac{\mathcal{A}_B}{8r^4}(3\cos(2\theta)+1)e^{-\frac{r^2}{\sigma^2}}\left(-3\sqrt{\pi}\sigma^3 e^{\frac{r^2}{\sigma^2}}\operatorname{erf}\left(\frac{r}{\sigma}\right)\right. \\
&\quad \left. + 4r^3 + 6r\sigma^2\right), \qquad (3.48)\\
(\partial^j h^B_{ij} - \partial_i h^B)_\theta &= \frac{\mathcal{A}_B}{4r^3\sigma^2}\sin(2\theta)e^{-\frac{r^2}{\sigma^2}}\left(-3\sqrt{\pi}\sigma^5 e^{\frac{r^2}{\sigma^2}}\operatorname{erf}\left(\frac{r}{\sigma}\right)\right. \\
&\quad \left. + 4r^3\sigma^2 + 4r^5 + 6r\sigma^4\right), \qquad (3.49)\\
(\partial^j h^B_{ij} - \partial_i h^B)_\phi &= 0,
\end{aligned}
$$

and after applying the Jacobian, the right hand side in Cartesian coordinates but expressed in terms of (r,θ,ϕ) is

$$
\begin{aligned}
(\partial^j h^B_{ij} - \partial_i h^B)_x &= \frac{\mathcal{A}_B}{8r^4\sigma^2}\sin(\theta)\cos(\phi)\left(2re^{-\frac{r^2}{\sigma^2}}\left(\cos(2\theta)\left(10r^2\sigma^2+4r^4+15\sigma^4\right)\right.\right. \qquad (3.50)\\
&\quad \left.\left. + 6r^2\sigma^2 + 4r^4 + 9\sigma^4\right) - 3\sqrt{\pi}\sigma^5(5\cos(2\theta)+3)\operatorname{erf}\left(\frac{r}{\sigma}\right)\right),\\
(\partial^j h^B_{ij} - \partial_i h^B)_y &= \frac{\mathcal{A}_B}{8r^4\sigma^2}\sin(\theta)\sin(\phi)\left(2re^{-\frac{r^2}{\sigma^2}}\left(\cos(2\theta)\left(10r^2\sigma^2+4r^4+15\sigma^4\right)\right.\right.\\
&\quad \left.\left. + 6r^2\sigma^2 + 4r^4 + 9\sigma^4\right) - 3\sqrt{\pi}\sigma^5(5\cos(2\theta)+3)\operatorname{erf}\left(\frac{r}{\sigma}\right)\right),\\
(\partial^j h^B_{ij} - \partial_i h^B)_z &= \frac{\mathcal{A}_B}{8r^4\sigma^2}\cos(\theta)e^{-\frac{r^2}{\sigma^2}}\left(-3\sqrt{\pi}\sigma^5(5\cos(2\theta)-1)e^{\frac{r^2}{\sigma^2}}\operatorname{erf}\left(\frac{r}{\sigma}\right)\right.\\
&\quad \left. + \cos(2\theta)\left(20r^3\sigma^2 + 8r^5 + 30r\sigma^4\right) - 2r\left(2r^2\sigma^2 + 4r^4 + 3\sigma^4\right)\right).
\end{aligned}
$$

Here again, `Mathematica` [94] is used to carry out the following integral, where now the index i runs along (x,y,z)

$$
\hat{\xi}_i = -\frac{1}{4\pi}\int \frac{(\partial^j h^B_{ij} - \partial_i h^B)}{\mid \mathbf{r} - \mathbf{r}' \mid} dx^3, \qquad (3.51)
$$

resulting, in terms of the spherical harmonics

$$
\begin{aligned}
\hat{\xi}_x &= -\sqrt{\frac{\pi}{3}}\frac{\mathcal{A}_B\sigma^2}{140r^4}e^{-\frac{r^2}{\sigma^2}}\left[\left(7\sqrt{2\pi}r^2\sigma e^{\frac{r^2}{\sigma^2}}\operatorname{erf}\left(\frac{r}{\sigma}\right) - 14\sqrt{2}r^3\right)(Y_{1-1} - Y_{11})\right. \qquad (3.52)\\
&\quad \left. + \left(\operatorname{erf}\left(\frac{r}{\sigma}\right)\sqrt{7\pi}e^{(r/\sigma^2)}\left(15\sigma^3 - 6r^2\sigma\right) - 8\sqrt{7}r^3 - 30\sqrt{7}r\sigma^2\right)(Y_{3-1} - Y_{31})\right],
\end{aligned}
$$

$$
\begin{aligned}
\hat{\xi}_y &= i\sqrt{\frac{\pi}{3}}\frac{\mathcal{A}_B\sigma^2}{140r^4}\left[\left(14\sqrt{2}r^3 - 7e^{r^2/\sigma^2}\sqrt{2\pi}r^2\sigma\operatorname{erf}\left(\frac{r}{\sigma}\right)\right)(Y_{1-1} + Y_{11})\right. \qquad (3.53)\\
&\quad \left. + \left(\sqrt{7\pi}e^{r^2/\sigma^2}\operatorname{erf}\left(\frac{r}{\sigma}\right)\left(6r^2\sigma - 15\sigma^3\right) + 30\sqrt{7}r\sigma^2 + 8\sqrt{7}r^3\right)(Y_{3-1} + Y_{31})\right],
\end{aligned}
$$

$$\hat{\xi}_z = \frac{\sqrt{\pi}\mathcal{A}_B\sigma^2}{420r^4}e^{-\frac{r^2}{\sigma^2}}\left[\left(28\sqrt{3\pi}r^2\sigma e^{\frac{r^2}{\sigma^2}}\operatorname{erf}\left(\frac{r}{\sigma}\right) - 56\sqrt{3}r^3\right)Y_{10}\right. \tag{3.54}$$
$$\left. + \left(\sqrt{7\pi}e^{r^2/\sigma^2}\operatorname{erf}\left(\frac{r}{\sigma}\right)\left(18r^2\sigma - 45\sigma^3\right) + 24\sqrt{7}r^3 + 90\sqrt{7}r\sigma^2\right)Y_{30}\right].$$

The next lines are not strictly needed here, but for the curious reader, applying the inverse jacobian J^{-1} 3.47 it is possible to compute the components of $\hat{\xi}_i$ in spherical polar coordinates as follows

$$\hat{\xi}_r = \frac{\mathcal{A}_B\sigma^3}{32r^4}(3\cos(2\theta)+1)e^{-\frac{r^2}{\sigma^2}}\left(\sqrt{\pi}e^{\frac{r^2}{\sigma^2}}\left(2r^2-3\sigma^2\right)\operatorname{erf}\left(\frac{r}{\sigma}\right) + 6r\sigma\right), \tag{3.55a}$$

$$\hat{\xi}_\theta = -\frac{\mathcal{A}_B\sigma^2}{8r^3}\sin(\theta)\cos(\theta)e^{-\frac{r^2}{\sigma^2}}\left(3\sqrt{\pi}\sigma^3 e^{\frac{r^2}{\sigma^2}}\operatorname{erf}\left(\frac{r}{\sigma}\right) - 4r^3 - 6r\sigma^2\right), \tag{3.55b}$$

$$\hat{\xi}_\phi = 0. \tag{3.55c}$$

However, what is indeed necessary is to calculate ξ_i, for which first 3.35b is applied to conserve the calculation that was done in Cartesian coordinates, and only after, applying the inverse Jacobian the wanted result will come out.

$$\begin{aligned}\xi_r &= (J^{-1})^i_r\hat{\xi}_i + \partial_r\varphi \\ &= \frac{\mathcal{A}_B}{128r^4}\left(3\sqrt{\pi}\sigma^3(3\cos(2\theta)+1)\left(2r^2-3\sigma^2\right)\operatorname{erf}\left(\frac{r}{\sigma}\right)\right. \\ &\left. +2re^{-\frac{r^2}{\sigma^2}}\left(\cos(2\theta)\left(8r^4+27\sigma^4\right) - 8r^4 + 9\sigma^4\right)\right),\end{aligned} \tag{3.56}$$

$$\begin{aligned}\xi_\theta &= (J^{-1})^i_\theta\hat{\xi}_i + \partial_\theta\varphi \\ &= -\frac{3\mathcal{A}_B\sigma^2}{32r^3}\sin(\theta)\cos(\theta)e^{-\frac{r^2}{\sigma^2}}\left(\sqrt{\pi}\sigma e^{\frac{r^2}{\sigma^2}}\left(2r^2+3\sigma^2\right)\operatorname{erf}\left(\frac{r}{\sigma}\right)\right. \\ &\left. - 8r^3 - 6r\sigma^2\right),\end{aligned} \tag{3.57}$$

$$\xi_\phi = (J^{-1})^i_\phi\hat{\xi}_i + \partial_\phi\varphi = 0. \tag{3.58}$$

The important part is almost in there. After assembling ξ_i it is possible to compute the transformation to TT gauge of the Brill initial data for the Holz seed function 3.8, and it is here where also the beauty happens, since it is possible to rewrite the Brill perturbation $h^{B'}_{ij}$ in the

same form as the Teukolsky perturbation was originally written in 3.6a, which it is recalled in here

$$h_{rr} = A f_{rr}, \tag{3.59a}$$
$$h_{r\theta} = rB f_{r\theta}, \tag{3.59b}$$
$$h_{\theta\theta} = r^2 (C f^{(1)}_{\theta\theta} + A f^{(2)}_{\theta\theta}), \tag{3.59c}$$
$$h_{\phi\phi} = r^2 \sin^2\theta (C f^{(1)}_{\phi\phi} + A f^{(2)}_{\phi\phi}). \tag{3.59d}$$

Nevertheless, the difference relies on the particular expression of the coefficients, which for the Brill wave are written as

$$A^B = \frac{\mathcal{A}_B \sigma^2}{8r^5}\left[2re^{-(r/\sigma)^2}\left(4r^2+9\sigma^2\right) + \sqrt{\pi}\sigma\left(2r^2-9\sigma^2\right)\operatorname{erf}\left(\frac{r}{\sigma}\right)\right], \tag{3.60a}$$

$$B^B = -\frac{\mathcal{A}_B}{12r^5}\left[2re^{-(r/\sigma)^2}\left(4r^4+6r^2\sigma^2+9\sigma^4\right) - 9\sqrt{\pi}\sigma^5\operatorname{erf}\left(\frac{r}{\sigma}\right)\right], \tag{3.60b}$$

$$C^B = \frac{\mathcal{A}_B}{96r^5\sigma^2}\left[2re^{-\frac{r^2}{\sigma^2}}\left(16r^6+36r^2\sigma^4+63\sigma^6\right)\right. \tag{3.60c}$$
$$\left. + 3\sqrt{\pi}\sigma^5\left(2r^2-21\sigma^2\right)\operatorname{erf}\left(\frac{r}{\sigma}\right)\right].$$

In Fig. 3.1 these coefficients for both Brill and Teukolsky are compared with a suitable rescaling of the amplitudes $\mathcal{A}_T = \mathcal{A}_B/80$. The qualitative features of both sets of initial data, for the given seed functions, indeed appear quite similar. Moreover, for the interested reader, in Fig. E.1 from Appendix E all the non-vanishing components of the perturbation h_{ab} for Brill and Teukolsky in TT gauge are shown.

It is important to note, however, that the transformation of the linearized Brill wave initial data to TT gauge results in a purely quadrupolar Teukolsky wave only for the specific angular dependence of the Holz seed function 3.8. In general, linearized Brill wave initial data are a superposition of waves with different multipole moments, as it might seem obvious, but for this special choice 3.8 all multipoles different from $\ell = 2$ are suppressed.

3.2.2 *Gauge-invariant Moncrief formalism*

As a second approach to computing the Teukolsky and Brill data, the gauge-invariant Moncrief formalism is employed (see [95] and also [96] for a review as well as Section 9.4.1 in [10] for a textbook treatment). In general, the Moncrief formalism assumes that the spacetime metric can be decomposed into a background metric, g^B_{ab}, given by the Schwarzschild metric and a perturbation h_{ab}. In this specific case, the background metric is flat and hence corresponds to a zero-mass Schwarzschild spacetime. The perturbation h_{ab} is then decomposed into scalar, vector, and tensor spherical harmonics of even and odd

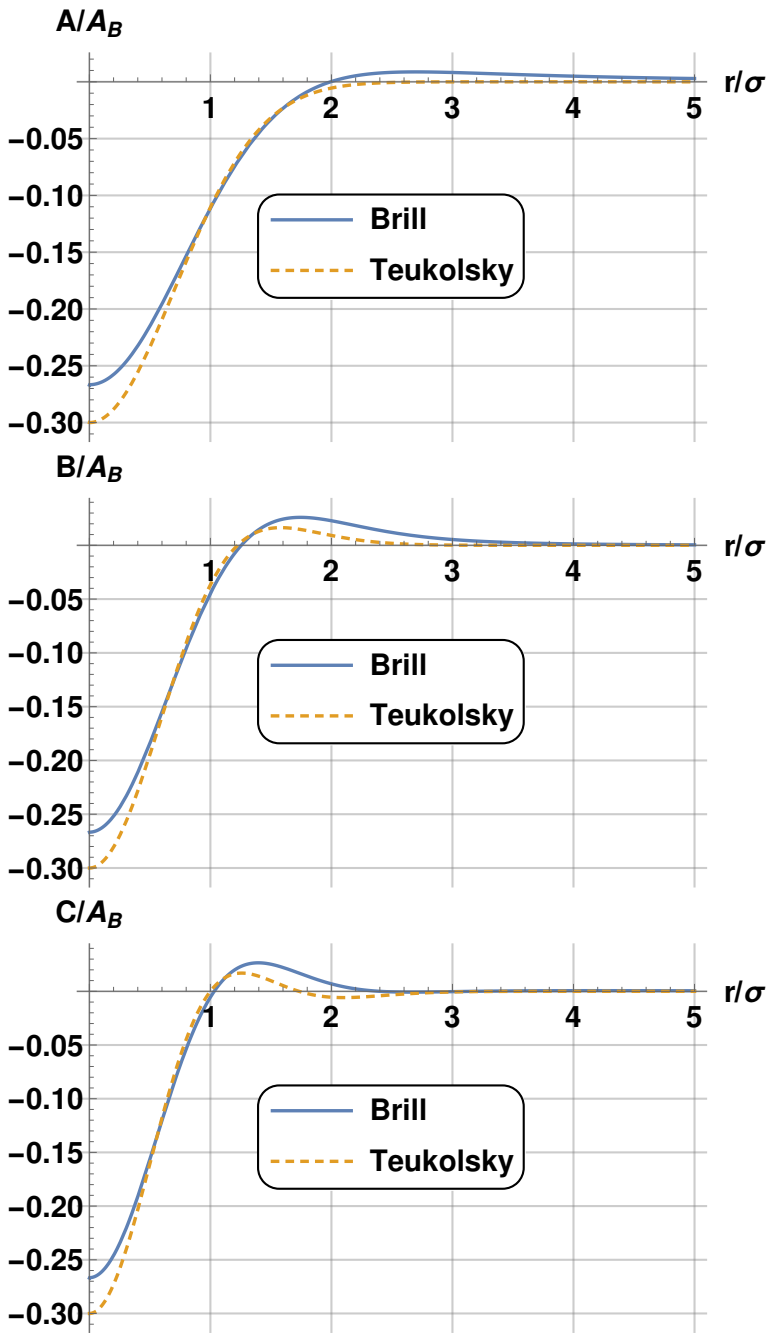

Figure 3.1: Comparisons of the functions A (top panel), B (middle panel, and C (bottom panel) for Teukolsky waves and Brill waves, both expressed in TT gauge. From these functions, which are listed in Eqs. 3.3 and 3.60, respectively, the initial spatial metric γ_{ij} can be computed from Eq. 3.6a. For the purposes of these comparisons $\mathcal{A}_T = \mathcal{A}_B/80$ and $\sigma = \lambda$ are adopted, and show the functions A, B, and C divided by $\mathcal{A}_B$ for both sets of data.

parity, from which the gauge-invariant Moncrief functions $R_{\ell m}$ can be computed for each mode ℓ and m.

For both the Teukolsky and the Brill data, only even-parity contributions enter the decomposition of the perturbative metric, for which the prescription starting with Eq. (9.77) in [10] might be followed. Specifically, for both the Teukolsky data γ^T_{ij} and the Brill data γ^B_{ij}, the projections $H_{2\ell m}$, $h_{1\ell m}$, $K_{\ell m}$, and $G_{\ell m}$ from Eqs. (9.78) through (9.81) are computed. In these integrals, the components of the tensor spherical harmonics can be expressed in terms of functions $W_{\ell m}$ and $X_{\ell m}$, which are listed in Appendix C.1. For instance, $G_{\ell m}$ is computed from

$$G_{\ell m} = \frac{1}{2(\ell-1)\ell(\ell+1)(\ell+2)} \frac{1}{r^2} \int \gamma_- W^*_{\ell m} \, d\Omega \tag{3.61}$$

(where $\gamma_- \equiv \gamma_{\theta\theta} - \gamma_{\phi\phi}/\sin^2\theta$, and where $\gamma_{\theta\phi} = 0$ is assumed).

In the next step, the functions $k_{1\ell m}$ and $k_{2\ell m}$ from (9.88) and (9.89) in [10] need to be found. Finally, these functions can be combined into the gauge-invariant Moncrief functions $R_{\ell m}$ as in (9.87) in [10].

For the Teukolsky waves of section 3.1.1, all the intermediate results are listed in the appendix C.1.1 with corresponding figures.

Since these data are constructed as an axisymmetric, purely quadrupolar wave, it is not surprising that the only non-vanishing terms are those with $\ell = 2$ and $m = 0$. The final result for the gauge-invariant Moncrief function R^T_{20} is

$$R^T_{20} = -\sqrt{\frac{\pi}{5}} \frac{8\mathcal{A}_T}{\lambda^4} r^3 e^{-(r/\lambda)^2} \left(2r^2 - 7\lambda^2\right). \tag{3.62}$$

The Brill waves of Section 3.1.2, on the other hand, are not purely quadrupolar by construction. In Section 3.2.1 it was already shown that, for the special choice of the Holz seed function (3.8), a transformation of the data to TT gauge again results in a purely quadrupolar Teukolsky wave. It is therefore not surprising that, in this case again, the only non-zero Moncrief function is that with $\ell = 2$ and $m = 0$. Alternatively, the Moncrief formalism to the Brill wave in its original gauge of Section 3.1.2 may be applied. In this case, the intermediate results for the projections $H_{2\ell m}$, $h_{1\ell m}$, $K_{\ell m}$, and $G_{\ell m}$ as well as the functions $k_{1\ell m}$ and $k_{2\ell m}$ are listed in Appendix C.1.2 with corresponding figures. The Moncrief function R_{20} is, by construction, independent of gauge, and given by

$$R^B_{20} = \sqrt{\frac{\pi}{5}} \mathcal{A}_B \left[\frac{1}{6r\sigma^2} e^{-(r/\sigma)^2} \left(4r^4 + 2r^2\sigma^2 + 3\sigma^4\right) - \frac{\sqrt{\pi}}{4} \frac{\sigma^3}{r^2} \operatorname{erf}\left(\frac{r}{\sigma}\right) \right]. \tag{3.63}$$

Both (3.62) and (3.63) can also be written in the form

$$R_{20} = \frac{r}{6}\sqrt{\frac{\pi}{5}} \left(r\partial_r A - 6A - 6B + 12C\right), \tag{3.64}$$

with the functions A, B, and C given by (3.3) for Teukolsky waves, and by (3.60) for Brill waves (see also exercise 9.7 in [10]).

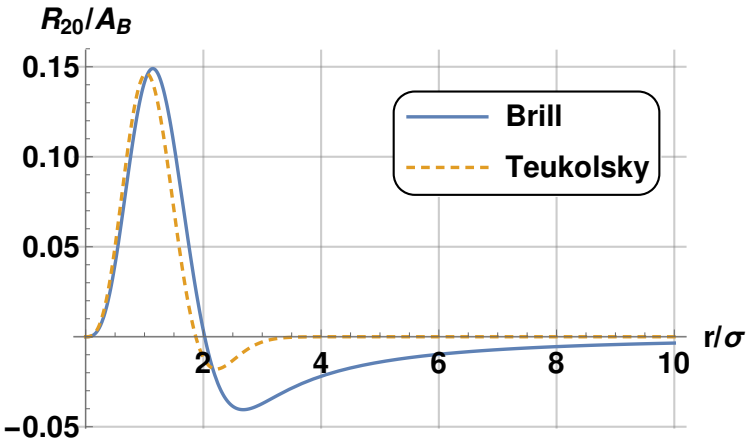

Figure 3.2: The gauge-invariant Moncrief function $R_{20}/\mathcal{A}_B$ for Teukolsky (orange dashed line) and Brill (blue continuous line) waves. As in Fig. 3.1 $\mathcal{A}_T = \mathcal{A}_B/80$ is chosen as well as $\lambda = \sigma$ and plot both functions in units of the amplitude $\mathcal{A}_B$.

In Fig. 3.2 the Moncrief functions (3.62) and (3.63) are compared. While the two results for Teukolsky and Brill wave evidently differ quantitatively, their general qualitative features are, indeed, quite similar, which is consistent with the findings of Section 3.2.1. It is important to note, however, that the only gauge-invariant function is R_{20}, therefore, the only one that can serve for a fair comparison. In the figures from Appendix C it can be observed that all the other intermediate projections do not agree, neither qualitatively, but at the end when used to compute R_{20}, the final result is quite similar for both Brill and Teukolsky.

Finally, it is instructive to consider multipole moments with $\ell > 2$ for the Brill wave initial data. Starting with these data in the gauge of Section 3.1.2, the projections $H_{2\ell m}$, $h_{1\ell m}$, and $K_{\ell m}$ must all vanish identically for $\ell > 2$, but $G_{\ell m}$, given by Eq. 3.61, could be nonzero. To evaluate this term for Brill waves it is observed that, from Eq. 3.18, $\gamma_- = 2q$, which contains both monopole and quadrupole terms (see Eq. 3.9). Note also that the functions $W_{\ell 0}$ can be written as a linear combination of spherical harmonics $Y_{\ell' 0}$ with $\ell' \leq \ell$ (see Appendix D). Using Eq. D.12, the integral in Eq. 3.61 may therefore be written as

$$\begin{aligned} \frac{1}{r^2}\int \gamma_- W^*_{\ell 0}\, d\Omega &= 4\sqrt{2\ell+1}\int q(\sqrt{5}Y_{20} + Y_{00})\, d\Omega \\ &= 4\sqrt{2\ell+1}\left(\sqrt{5}\, q_{20} + q_{00}\right), \qquad (\ell > 2 \text{ even}) \end{aligned} \tag{3.65}$$

where the decomposition from Eq. 3.9 was employed in the last step. In general, this integral will therefore *not* vanish, and will instead give rise to multipole moments higher in order than $\ell = 2$. For the seed function from Eq. 3.8, however, $q_{20} = -q_{00}/\sqrt{5}$ (see Eqs. 3.10), leads to an exact cancellation in Eq. 3.65, and therefore to a vanishing of all higher-order multipole moments. This result is consistent with

the finding in Section 3.2.1 that, when transformed to TT gauge, Brill waves become purely quadrupolar if the seed function has the angular dependence of Eq. 3.8.

3.2.3 *Kretschmann scalar*

As a third way to compare the Teukolsky and Brill initial data the Kretschmann scalar is computed

$$I = {}^{(4)}R^{abcd}\,{}^{(4)}R_{abcd}, \tag{3.66}$$

where ${}^{(4)}R_{abcd}$ is the (four-dimensional) spacetime Riemann tensor of the spacetime. In the case of time-symmetric vacuum data, as this is, the Kretschmann scalar might be expressed in terms of the (three-dimensional) spatial Ricci tensor R_{ij} only,

$$I = 8\,\gamma^{ij}\gamma^{kl}R_{ik}R_{jl}. \tag{3.67}$$

The Kretschmann scalar (I) is computed for both the Teukolsky data from Section 3.1.1 and the Brill data from Section 3.1.2 to leading order (i.e. quadratic) in the amplitude. In Fig. 3.3 the results are compared, and as in the previous comparisons, it is possible to see that the qualitative features are very similar.

There is, however, a more direct way of comparing both Kretschmann scalars I_T and I_B, by looking at their ratio in Fig. 3.4. Once again, the adopted ratio between both amplitudes $\mathcal{A}_B$ and $\mathcal{A}_T$ is $\mathcal{A}_T = \mathcal{A}_B/80$. As one can observe in Fig. 3.4 some variations appear on the ratio, rather than be just a constant surface, showing that the Kretschmann scalars I_B and I_T are qualitatively similar but indeed quantitatively different.

3.3 SUMMARY AND DISCUSSION

Two common approaches in the construction of GW initial data have been compared at the linear level, particularly those called Teukolsky waves [90] (Section 3.1.1) and Brill waves [91] (Section 3.1.2). Both approaches use a seed function for which, as other authors do, Gaussian profiles 3.2 and 3.8 were chosen. While the Teukolsky waves are constructed as purely quadrupolar ($\ell = 2$) waves, the Brill waves, in general, are not.

The objective was to compare both sets of initial data, however, as they appear in different gauges a direct comparison was not possible. Instead, three different ways were adopted to compare the data: the Brill data was transformed into the TT gauge of Teukolsky (Section 3.2.1), the gauge-invariant Moncrief functions $R_{\ell m}$ were computed (Section 3.2.2) and the Kretschmann scalars for both cases were evaluated (Section 3.2.3).

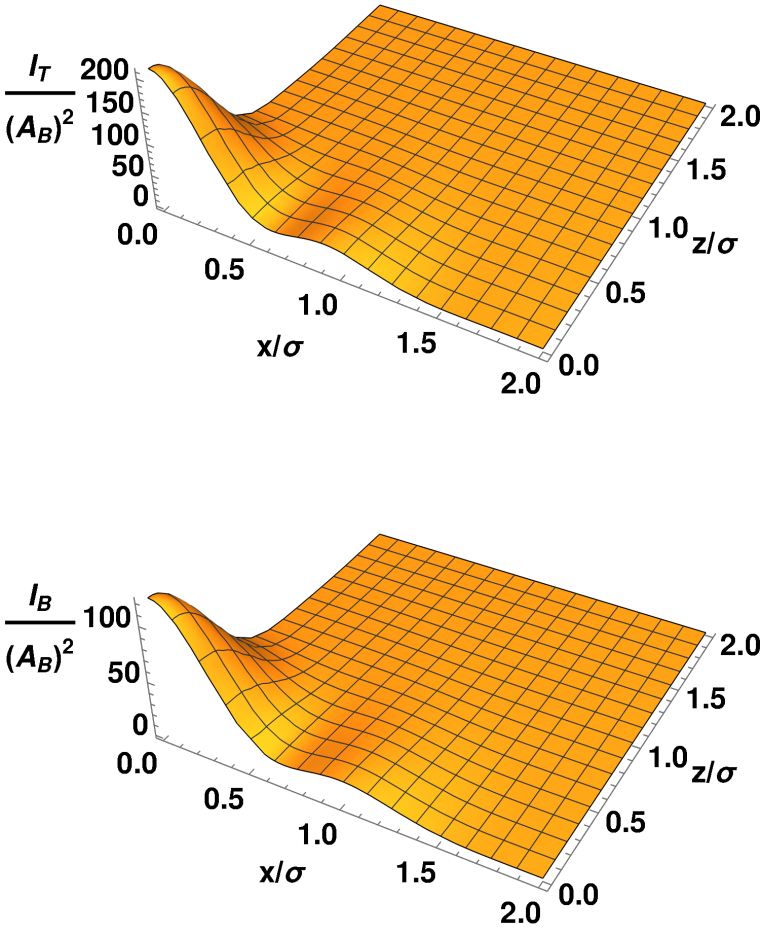

Figure 3.3: The Kretschmann scalar I for both Teukolsky waves (top panel) and Brill waves (bottom panel) divided by the square of the amplitude ${\mathcal{A}_B}^2$. As in Figs. 3.1 and 3.2 $\mathcal{A}_T = \mathcal{A}_B/80$ and $\lambda = \sigma$ are adopted.

Surprisingly, it was found that, while linearized Brill waves will, in general, *not* be purely quadrupolar, and will be instead superpositions of waves with different multipole moments, for the special choice of the Holz seed function 3.8, that has a very concrete angular dependence, all higher-order moments cancel out exactly, casting the Brill waves as purely quadrupolar waves. Meanwhile, these waves are not identical to Teukolsky waves with the seed function 3.2, both share many qualitative features in all the three comparisons.

Teukolsky and Brill wave initial data play an important role in the context of vacuum gravitational critical collapse, where they have been often adopted by several different authors as [58] or [51] in their recent works as well as in Chapter 4 from this manuscript. As it is known that the two types of initial data appear to have different

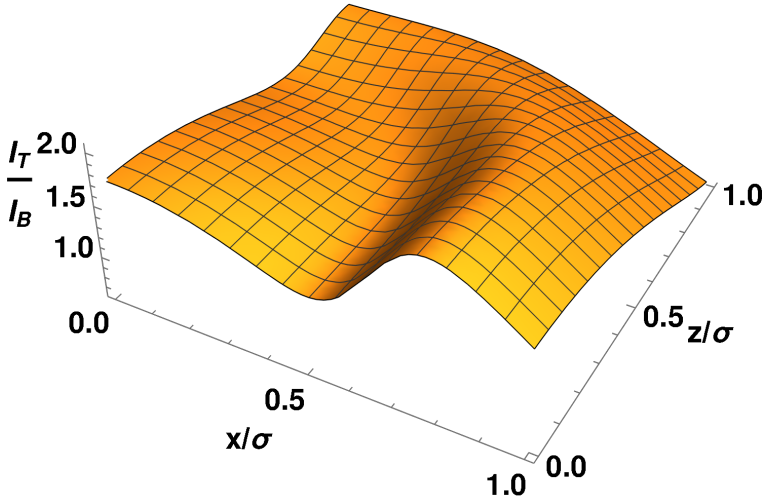

Figure 3.4: The ratio I_T/I_B between the Kretschmann scalars for Teukolsky and Brill waves. As in the previous figures $\mathcal{A}_T = \mathcal{A}_B/80$ and $\lambda = \sigma$ are adopted.

threshold solutions (i.e. different critical exponents γ) and to behave numerically differently. Nevertheless, the works [67] and [68], where initial data with different multipole moments lead to qualitatively different threshold solutions in the critical collapse of electromagnetic waves, suggest that higher-order multipole moments present in the Brill data may result in the observed differences in their evolution from those of Teukolsky, as these different multipoles would couple to different parts of the non-linearities of the Einstein's equations, giving a hypothesis to proof during the present work. However, as discussed above, for precisely the seed function often used for Brill waves Eq. 3.8 those higher-order multipole moments are exactly suppressed. The conclusion is, therefore, that the multipole structure of Brill waves cannot be held responsible for the observed differences.

It is important to remark, however, that for these choices of the seed functions despite the data being similar, they are not identical. As discussed before, the Brill data is in a different gauge, but even if transformed to TT gauge from Teukolsky data, both sets still correspond to different seed functions. While it may well be worth exploring whether either one of these differences is related to the observed differences in the evolution of the data, it is also possible that the latter is related to nonlinear effects, which are ignored in the analysis here.

4

EVOLUTION OF BRILL WAVES WITH AN ADAPTIVE PSEUDOSPECTRAL METHOD

In this Chapter a psudospectral adaptive code, `bamps`, is used to evolve twist-free, axisymmetric GWs in vacuum close to the threshold of collapse. This setup resembles pure gravity and it is beyond spherical symmetry since there are not spherical dynamical GWs. It is clear so far that critical phenomena in gravitational collapse in spherical symmetry match the full picture of critical phenomena, however, as it was summarized in the historical recapitulation of Section 1.5 and also seen in Chapter 2, once spherical symmetry is dropped the phenomenology becomes more complicated. The three main features of critical phenomena are universality of the critical solution, scale-invariance and power-law behavior of the order parameter with universal exponent. It is already known that in gravity the power-law behavior manifests both in the supercritical and subcritcail regimes. In the supercritical regime the mass of the formed BH follows Eq. 1.40, which it is remind here as

$$M_{BH} \simeq |p - p_\star|^\gamma, \tag{4.1}$$

where M_{BH} is the mass of the formed BH, p is the independent parameter on the family of initial data, $p_\star$ is the critical value and γ is the scaling exponent. In the subcritical regime, the maximum of any invariant curvature scalar, as argued in [37], satisfies the power-law behavior. In Section 1.1, it was already seen that when working in vacuum the stress-energy tensor vanishes $T_{\mu\nu} = 0$, and consequently does the Ricci scalar $R = R^\mu{}_\mu$. The relevant invariant curvature scalar for this work, whose maximum should follow a power-law of the form of Eq. 1.41 is the Kretschmann scalar

$$I = R_{abcd}R^{abcd}, \tag{4.2}$$

where R_{abcd} is the four dimensional Riemann tensor. For the purpose of smooth reading, let us recall the scaling relation for the maximum of such a curvature scalar

$$I_{max}^{-1/4} \simeq |p - p_\star|^\gamma. \tag{4.3}$$

Recall that in here the Kretschmann scalar is to the power of $-1/4$ such that the quantity $I^{-1/4}$ has dimensions of length and it scales

with γ and not a multiple of such a exponent. Moreover, arguments of [97, 98] suggest that if the critical spacetime is DSS, then this power-law from Eq. 4.3 should happen with a periodic wiggle superimposed. The above properties (scale-invariance, universality and power-law behavior with universal exponent) have been repeatedly verified for the spherical massless scalar field for many different families of initial data. In spherical symmetry, other alternative models have been considered and even though details such as the particular type of self-similarity differ, the basic structure prevails. See Section 1.5 for a compilation of different studies and [35, 36] for reviews.

Less clear, however, is the precise extent to which critical phenomena extend beyond spherical symmetry. The simplest scenario in which dynamical GWs happen is the axisymmetric setup. This composition is of special interest in GR as working in vacuum one can try to understand the aspects of critical collapse determined by pure gravity. Previous studies of this system have considered two main types of vacuum initial data: Brill waves [91], which refer to a solution of the constraint equations in axisymmetric vacuum at a moment of time symmetry, and Teukolsky waves, constructed first by Teukolsky [90] and generalized afterwards by Rinne [92], which are general solutions to the linearized Einstein field equations in TT gauge. For a comparison of these two types of waves at the linear level see Chapter 3 or [70]. It is worth commenting that as linearized solutions, Teukolsky wave initial data need to be dressed up to construct solutions of the constraint equations of GR. See [49, 50, 57, 99] for some strategies.

Concerning vacuum time evolutions, although it was already mentioned in Section 1.5, let us give credit again here to Abrahams and Evans [49, 50] who were the first to study GWs near the threshold of collapse already in the early 1990s. In summary, they evolved members of one-parameter families of (constraint solved) Teukolsky waves without moment of time symmetry and tuned to the threshold. The authors observed that the BHs masses also follow the power-law 4.1. Since then, numerous authors (see Table 1.1) have evolved GWs to explore the threshold of collapse, nevertheless, none have unambiguously recovered this early success. Two of these studies deserve additional mention here. First, in [58], which is the direct precursor of this Chapter, the authors evolved a single family of Brill waves. In qualitative agreement with other axisymmetric simulations [62, 65, 67, 68], near the verge of BH formation global maxima of the curvature form away from the origin as a consequence of large spikes appearing in the curvature. In collapse spacetimes, a separate pair of horizons were found along the symmetry axis around the greatest of the curvature spikes. In this study, although tentative evidence for the power-law scaling with a periodic wiggle was found (there were not periods enough for a solid evidence) for the Kretschmann scalar, nothing could be concluded about universality as the authors evolved just one family. In a

second important and recent work that also deserves to be mentioned here, Ledvinka and Khirnov [51] directly confirmed the findings of Hilditch *et. al.* [58] using an independent code and a different gauge, where they also tuned to a comparable vicinity of the threshold. Investigating several families of initial data, the authors also found pairs of disjoint AHs for (constraint solved) Teukolsky waves. Once again, also in qualitative agreement with other studies in axisymmetry, they report too that although power-law scaling does appear in their families, the scaling exponent does not seem to be universal. Therefore, it does not seem to be a universal threshold solution. However, the most important finding of [51] is the existence of repeated curvature features which do appear to be universal despite not happening in a strictly DSS manner.

The main hardship in both [58] and [51] was tuning p to $p_\star$. For instance, in spherical symmetry simulations, either by employing Adaptive Mesh Refinement (AMR) as in [17] or by using well-chosen coordinates as in [100, 101], it is frequently possible to tune to machine precision $|p - p_\star| \sim 10^{-15}$. In axisymmetric evolutions values such as $|p - p_\star| \sim 10^{-9}$ are usually viable, whereas the best that could be managed in [58] was $|p - p_\star| \sim 10^{-5}$. There are certain reasons for this. With less symmetry restrictions the numerical cost to reach a certain level of accuracy is inevitably higher. Despite of using a pseudospectral numerical method adapted to axisymmetry [34, 102], the computational cost of the evolutions rapidly grew near the threshold of collapse as finer curvature features form and more resolution is required. As a quantitative argument, in [58] about 10^6 core hours were used for a single family. As one will see, the current efficiency of the code `bamps` that was used for this work is much better. Besides that, an additional complication was that near the threshold, spacetime could not be classified as collapsing or dispersing because the evolution would fail before an AH could be found. It was unclear whether this was caused by a lack of resolution, coordinate singularities or the constraint violation rendering the solution unphysical.

Currently, this work returns to the problem of vacuum critical collapse using the same code as in [58], `bamps`, however, the code had a major redisign since then to improve the efficiency related to computational cost by using AMR. Through this Chapter the reader will see that six different families of Brill initial data are evolved and compared both among them and with previous work. As was previously done, two families of prolate and oblate centered Brill waves are evolved together with four completely new prolate and oblate off-centered Brill wave families.

4.1 FORMULATION AND NUMERICAL SETUP

NR is the tool used in this Chapter to evolve GWs in vacuum. The time evolution of the different sets of initial data were performed using the adaptive pseudospectral `bamps` code. In contrast to the spherical 3+1 code used in Chapter 2 where finite differences were used for the spatial derivatives with a second order convergence, `bamps` can evolve in full-3d and uses a pseudospectral approach for the spatial domain, which has the advantage of having an exponential spatial convergence (which dominates the convergence, at least in test cases [34]). To evolve the spacetime the code uses a first order reduction of the GHG formulation [33] of the Einstein equations 1.8, with the gauge choices described in [34]. Introducing the variables Φ_{iab} and Π_{ab} the field equations are (see Section 1.1 and Section 1.2 for definitions)

$$\begin{aligned}
\partial_t g_{ab} &= \beta^i \partial_i g_{ab} - \alpha \Pi_{ab} + \gamma_1 \beta^i C_{iab} \\
\partial_t \Phi_{iab} &= \beta^j \partial_j \Phi_{iab} - \alpha \partial_i \Pi_{ab} + \gamma_2 \alpha C_{iab} \\
&\quad + \frac{1}{2} \alpha n^c n^d \Phi_{icd} \Pi_{ab} + \alpha \gamma^{jk} n^c \Phi_{ijc} \Phi_{kab} \\
\partial_t \Pi_{ab} &= \beta^i \partial_i \Pi_{ab} - \alpha \gamma^{ij} \partial_i \Phi_{jab} + \gamma_1 \gamma_2 \beta^i C_{iab} \\
&\quad + 2\alpha g^{cd} \left(\gamma^{ij} \Phi_{ica} \Phi_{jdb} - \Pi_{ca} \Pi_{db} - g^{ef} \Gamma_{ace} \Gamma_{bdf} \right) \\
&\quad - 2\alpha \left(\nabla_{(a} H_{b)} + \gamma_4 \Gamma^c{}_{ab} C_c - \frac{1}{2} \gamma_5 g_{ab} \Gamma^c C_c \right) \\
&\quad - \frac{1}{2} \alpha n^c n^d \Pi_{cd} \Pi_{ab} - \alpha n^c \gamma^{ij} \Pi_{ci} \Phi_{jab} \\
&\quad + \alpha \gamma_0 \left(2 \delta^c{}_{(a} n_{b)} - g_{ab} n^c \right) C_c \,. \qquad (4.4)
\end{aligned}$$

Here spacetime components are denoted by Latin letters $a, b, c...$, the spatial components are denoted by the Latin letter $i, j, k...$, and the standard notation, coherent with Section 1.2, for the lapse, shift spatial metric and spacetime metric is used. The reduction constraint associated with the first order reduction is given by $C_{iab} = \partial_i g_{ab} - \Phi_{iab}$. The harmonic constraint C_a is expressed as a combination of the evolved variables $g_{ab}, \Phi_{iab}, \Pi_{ab}$, (see [33]). The constraint damping parameters were taken to be $\alpha\gamma_0 = \gamma_2 = 2\gamma_4 = 2\gamma_5 = 1$ throughout. The GHG formulation comes with the freedom to choose gauge source functions H^a, in this case

$$\begin{aligned}
n_a H^a &= -\eta_L \log(\gamma^{p/2}/\alpha) \,, \\
\gamma^i{}_a H^a &= -\eta_S / \alpha^2 \beta^i \,, \qquad (4.5)
\end{aligned}$$

with free scalar functions η_L, η_S. The free parameters were initially lifted from the best results of [58] and adjusted as seemed appropriate from there. As such the starting values were $p = 1, \eta_L = \bar{\eta}_L/\alpha^2 = 0.4/\alpha^2$ and $\eta_S = 6$. At the outer boundary radiation controlling, constraint preserving boundary conditions described in [103] are employed with the adjustments described in [34].

Brill wave initial data (see Section 3.1.2 from Chapter 3 and Section 4.2.1 from the present Chapter) was constructed externally and then interpolated onto the computational domain. In the treatment of such axisymmetric data one spatial dimension is suppressed using the cartoon-method [104], however the implementation follows the approach of [105], so that only two dimensional data on the x-z-plane is evolved, and the Killing vector is used to compute the missing derivatives. Furthermore, only regions where $x > 0$ and $z > 0$ are considered due to the symmetry of the problem.

The time evolution is performed with the method of lines, using a standard $RK4$ timestepping algorithm. Within `bamps`, the computational domain is divided into patches in a cubed-ball manner (see Fig. 4.1), forming a ball comprised of deformed cubes, each being represented internally as a unit cube $(u, v, w)^T \in [-1, 1]^3$ in the patch-local-coordinates.

These patches are further divided into smaller grids, which contained between 21 to 31 points in each dimensions in the present work. Within each grid, the numerical solution is represented by a nodal spectral representation in a Chebyshev basis, using Gauss-Lobatto collocation points in each dimension. The grids are coupled to each other using a penalty method as described in [106–108].

The division of the patches into individual grids is driven by the AMR system, which divides and combines grids based on heuristics that estimate the quality of the data representation. This h-refinement is implemented subject to a 1:2 condition as illustrated in Fig. 4.2. p-refinement functionality, in which the number of points per individual grid is increased is also implemented, but was not employed in this work. For most of the simulations, an estimate of the truncation error of the spectral series corresponding to the nodal data representation was used as the refinement indicator, ensuring a grid-local relative truncation error on the order of no more than 10^{-9} throughout the domain, at least up to the maximum number of refinement levels permitted (19 in the present work). A thorough technical description of this AMR setup is in preparation.

All computations are parallelized at the grid level, using MPI to distribute computational work across processes. An integrated load balancing system is used to ensure an even distribution of both computations and memory usage across all processes, redistributing grids as needed whenever AMR operations cause a change in the grid structure.

4.2 THE PHYSICAL MODEL

In this section, the type of initial data that is bisected, Brill waves, is recalled (see also Section 3.1.2). Then the bisection, the process that allows the estimation of the threshold amplitude within each

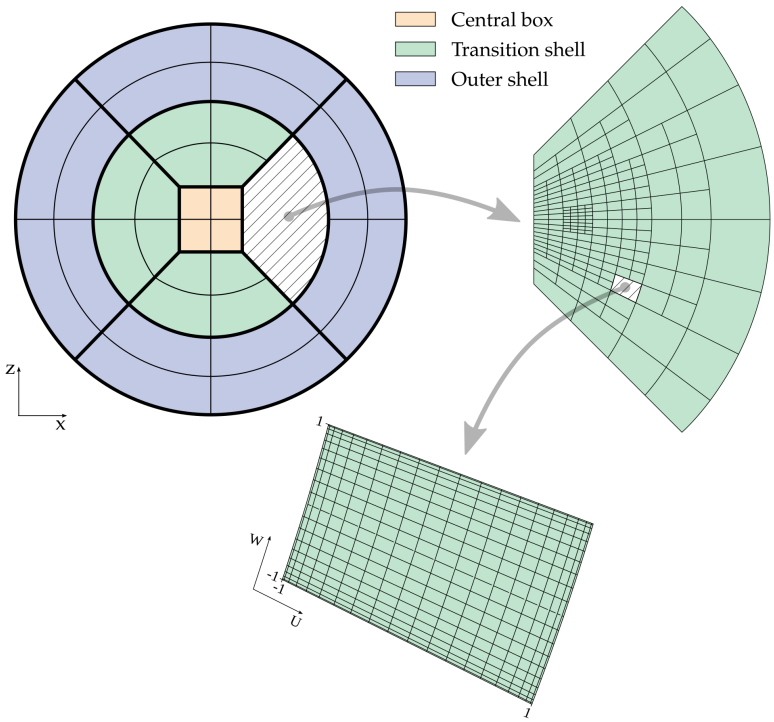

Figure 4.1: In the left part it is represented a two dimensional diagram of the `bamps` cubed-ball grid layout. The ball is built up of several transformed cubes. These patches can further be divided in subpatches using the AMR as shown on the right. In the bottom side is shown that each subpatch is covered by Gauss-Lobatto grids ranging from -1 to 1 in local coordinates.

of the evolved families is described. Finally, it is described the post-processing tools that enabled this estimation.

4.2.1 *Brill waves as initial data*

As seen in Section 3.1.2 from Chapter 3, Brill wave initial data are a GW solution to vacuum Einstein constraint equations. Following the procedure of Brill [91], it is possible to construct axisymmetric non-linear initial data, where the metric takes the form of Eq. 3.7, which it is recalled here

$$dl^2 = \gamma_{ij} dx^i dx^j = \Psi^4 \left[e^{2q} \left(d\rho^2 + dz^2 \right) + \rho^2 d\phi^2 \right] . \tag{4.6}$$

As the data are taken to be at a moment of time symmetry, the extrinsic curvature vanishes identically and, as a consequence, the momentum constraint (Eq. 1.31) gets automatically satisfied. For the seed function a general Gaussian is always chosen

$$q(\rho, z) = A\rho^2 e^{-\left[(\rho-\rho_0)^2/\sigma_\rho^2 + (z-z_0)^2/\sigma_z^2\right]} , \tag{4.7}$$

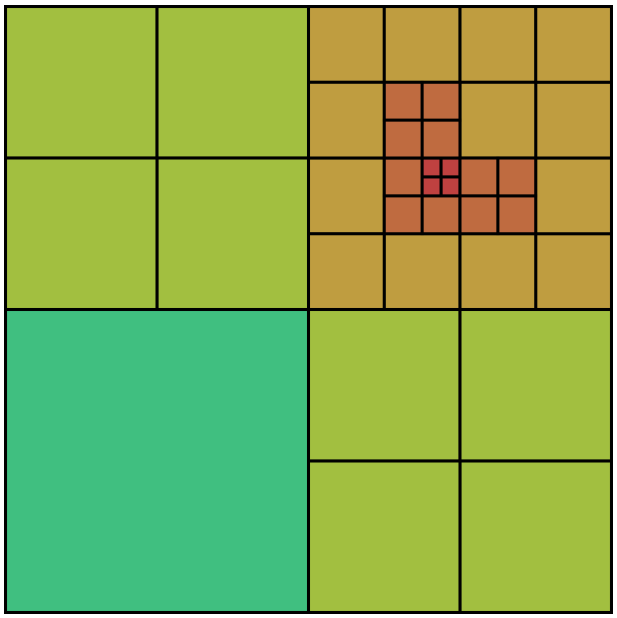

Figure 4.2: Schematic example of a recursively refined grid structure, of the type `bamps` uses obeying a 1:2 condition. This example corresponds to 5 levels of refinement.

whose parameters vary depending on the studied family. In the present Chapter the focus will be on six different families always with $z_0 = 0$, $\sigma_\rho = \sigma_z = 1$ covering centered ($\rho_0 = 0$) and off-centered ($\rho_0 = 4, 5$) Gaussians both geometrically prolate ($A > 0$) and oblate ($A < 0$).

Of these six families, the first (prolate $A > 0$, $\rho_0 = 0$) is best studied in the literature, see for example [51–53, 58, 93]. In [51] the centered oblate family ($A < 0$, $\rho_0 = 0$) was also treated, and so these two families serve as a point of reference. Khirnov and Ledvinka conclude that these centered families are more difficult to treat numerically than their off-set (constraint solved) Teukolsky wave initial data, which motivates the current use of off-center Brill wave data. (See [55] for constrained evolution of alternative Brill wave initial data, which would also be interesting to compare with in the future).

4.2.2 *Parameter search*

In order to study phenomena near the threshold of collapse, the first step is to identify that threshold as precisely as one can. In the case of one-parameter families, this means identifying the value of such parameter at the threshold. In the present work, the parameter varying within a family is the amplitude, A, in Eq. 4.7. Modifying A allows the classification of initial data depending on the outcome of its evolution. Initial data whose evolution leads to dispersion of the

fields are classified as subcritical, on the other hand, data that yields a BH is labelled as supercritical

$$A_{\text{subcritical}} < A_\star < A_{\text{supercritical}} \tag{4.8}$$

and similarly for families with $A < 0$.

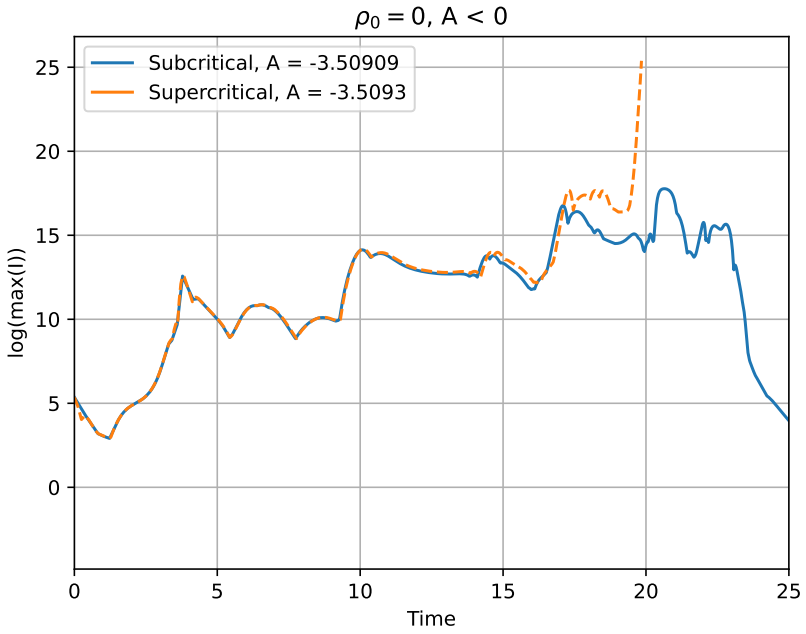

Figure 4.3: An illustrative figure to show the different behavior of two close sets of initial data. The chosen family is a centered oblate Brill wave $\rho_0 = 0$ with $A < 0$. One can see that in the case of the orange dashed line, corresponding to a supercritical amplitude $A = -3.50930$, the maximum of the Kretschmann scalar diverges meanwhile on the other hand in the case of the subcritical amplitude $A = -3.50909$ the Kretschmann's maximum decreases as the wave disperses.

In Fig. 4.3 one can see how the maximum of the Kretschmann scalar compares between a subcritical and a supercritical run. This plot illustrates how similar the evolutions of data from the same family can be, up to final times where the one parameter that discerns them makes all the difference between dispersal and collapse. It is clear evidence that for two sets of initial data that are infinitesimally close in the parameter space they have completely different outcomes, exemplifying the definition of a phase transition.

Working with `bamps` and an AH locator (see Section 4.2.3) enables the classification as follows. First, at least down to a neighborhood of the threshold, `bamps` is able to evolve subcritical data until they disperse. One can confidently classify the set of initial data as subcritical just by looking at all the fields dispersing by the end of each evolution. For instance, the blue line from Fig. 4.3 shows the field dispersal of

a subcritical run. Second, likewise in Fig. 4.3 one can see how the orange dashed line blows up, corresponding to a supercritical run, and stops before time 20. In these evolutions excision of the trapped region is not executed, therefore, in the case of BH formation `bamps` can only evolve for a short time after trapped surface formation. With this limitation, the procedure is looking for AHs as a post-processing step. Only when an AH is found a set of initial data is confidently classified as supercritical.

Categorizing the data as just explained one can estimate that the threshold amplitude lies in the regime between the highest subcritical amplitude and the lowest supercritical one. The process of classifying the evolved initial data proceeds in stages, each increasing the precision of the estimation of the threshold, thereby tuning closer to $A_\star$.

The bisection started with a trivial guess of weak and strong data. After the limits of the threshold regime are confirmed, data within them to further tune those bounds at each stage. The precision of such bounds is increased as far as the method allows. More specifically, at each stage the threshold regime was divided into 10 subregimes. When successful, this method manages to add a decimal point per stage to the limiting amplitudes. This approach furthermore has the advantage that the data necessary for scaling-plots (like Fig. 4.8) is already prepared directly at the end point of bisection without having to go back and resample.

4.2.3 *Apparent horizon locator*

To conclusively classify a set of initial data as supercritical, the AH finder `ahloc3d` [109], which is specifically designed for use with `bamps` AMR data is used. `ahloc3d` replaces the AH finder employed in [34, 58], which had no functionality with AMR data nor parallelization. During the development of `ahloc3d` thorough consistency checks were made with the results of the older code.

`ahloc3d` uses a Strahlkörper representation to describe test surfaces as

$$r = h(\theta, \phi) \tag{4.9}$$

relative to a single center point, and evaluates the expansion

$$\Theta = D_i s^i + K_{ij} s^i s^j - K\,, \tag{4.10}$$

where s_i is the outward pointing normal vector on the test surface and K is the extrinsic curvature of the spacetime slice under consideration, according to the algorithm described in [110]. Using two separate search methods, it first obtains a rough estimate employing a flow method using the expansion flow [111] to shrink a large test surface until an approximate AH is found, i.e. Θ is very small. It then refines

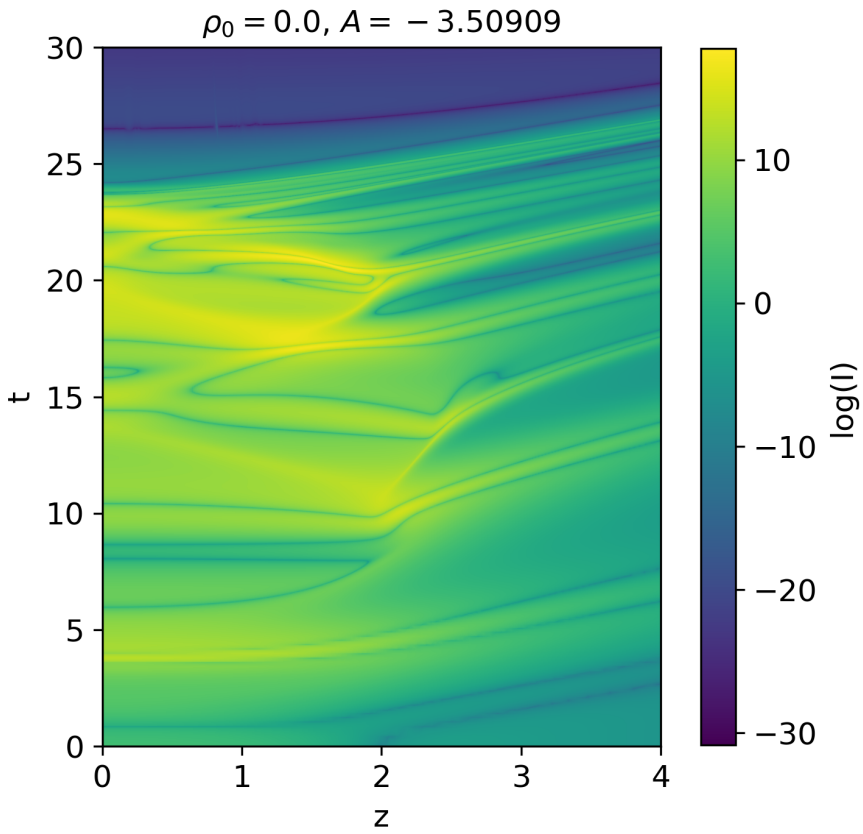

Figure 4.4: In this figure a color map of the logarithm of the Kretschmann scalar along the symmetry axis Z and trough time is shown for the oblate centered family $A < 0$, $\rho_0 = 0$, for the subcritical amplitude $A = -3.50909$.

this estimate using a Newton-Raphson iteration to locate the AH ($\Theta = 0$) with high accuracy. The search algorithm is fully parallelized using MPI. Its main limitation is the Strahlkörper representation of the test surfaces, which makes it unable to find AHs that are not radially convex. As it will be discussed further below (see Section 4.4), this has prevented the further fine-tuning of several families of initial data, as the found AHs approach such non-convex shapes.

4.3 NUMERICAL RESULTS

In this section it follows the discussion of the outcome from the bisection search described in Section 4.2.2 for each of the six families.

4.3.1 *Dynamics and threshold amplitudes*

Basic evolution within each of the families is similar and follows the behavior observed in [58] for the centered $A > 0$ family. Very weak data disperse rapidly, but as the strength of the data increases

the dynamics become more interesting. If one considers the simplest non-vanishing curvature scalar in this setup, the Kretschmann scalar, it possesses wave-like propagation together with large spikes when waves land on the symmetry axis and oscillate there. In comparison with the centered families, the off-center data tend to create these peaks further from the origin, probably because the curvature propagates further in the $\pm z$-directions before landing on the symmetry axis. This difference would have made the evolutions of the off-center families extremely expensive without AMR. To illustrate the dynamics qualitatively, in Fig. 4.4 a 2D plot of the logarithm of the Kretschmann scalar against the symmetry axis z and coordinate time is shown for a set of initial data close to criticality ($A = -3.50909$) for the oblate ($A < 0$) centered ($\rho_0 = 0$) family. Be aware that the region shown is relatively small but big enough to see that the several peaks of the curvature scalar occur away from the origin but along the symmetry axis before they disperse. The results for all of the other families are similar, with more and more off-centered peaks in the Kretschmann scalar appearing as the threshold of BH formation is approached. In the Appendix F similar plots for the rest of the families are presented. Note that this time the region of interest is bigger since the maximum spikes of the Kretschmann scalar happen further away in the symmetry axis. This result will be relevant for Section 4.3.2.

The small initial data that lead to dispersion and the strong initial data that yields a BH have a clear distinction. The classification of the data as supercritical ($A > A_\star$) is made if and only if a reliable AH is found with the `ahloc3d` tool. For an example of a reliable AH found by `ahloc3d` see Fig. 4.5. On the other hand, a set of initial data is classified as subcritical ($A < A_\star$) if complete dispersion is seen (with these inequalities flipped for the $A < 0$ families). This is a conservative approach but, given the challenge these extreme spacetimes face and the unfortunate occasional disagreement between different numerics, it is important to step with some care and responsibility to compare rigorously with the literature. The results of the bisection search are summarized in Table 4.1, where the highest subcritical amplitude and the lowest supercritical amplitude that were confidently classified with the `ahloc3d` are stated. After finding such bounds for the threshold the `ahloc3d` started to fail to find AHs in near threshold simulations. The limits found in the present work for the centered families threshold amplitudes are compatible with previous works [58] and [51].

4.3.2 *Disjoint apparent horizons*

With the setup of `ahloc3d` and the evolved data coming from `bamps`, after an AH is found for first time for a given supercritical member of a family, then it is also possible to find it in the several next time-steps. In [51, 58] the authors found a pair of disjoint AHs. In agreement with

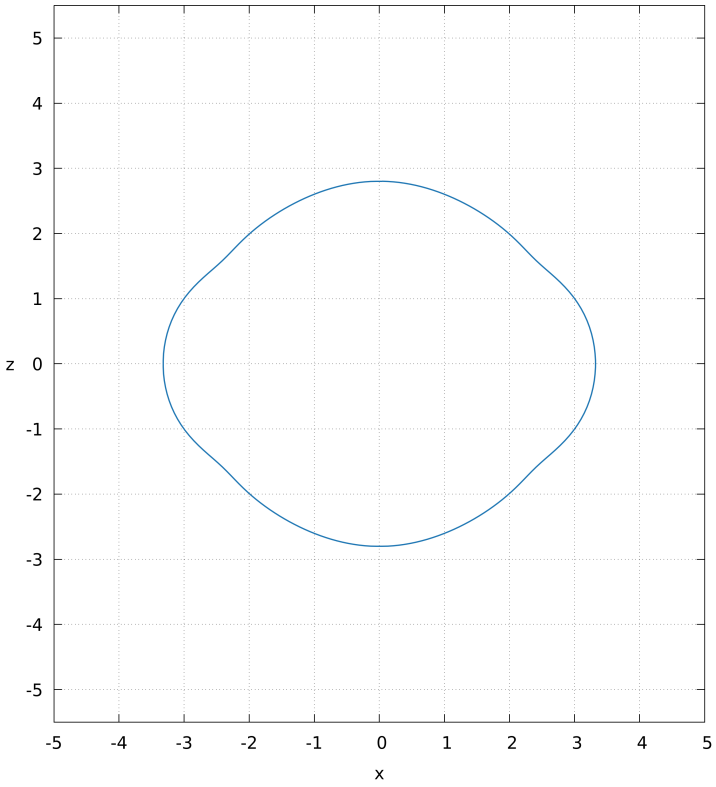

Figure 4.5: In this figure an AH found by the `ahloc3d` is shown. This corresponds to the off-center $\rho_0 = 4$, oblate ($A < 0$) family for an amplitude of $A = -0.0780$ at time $t \simeq 13.90$.

	ρ_0	A_{sub}	A_{sup}
Prolate ($A > 0$)	0	4.69667	4.69680
	4	0.09795	0.09870
	5	0.0641	0.0645
Oblate ($A < 0$)	0	-3.50909	-3.50930
	4	-0.07546	-0.07570
	5	-0.04878	-0.04900

Table 4.1: In this table the limits of the bisection search are shown. The highest subcritical (A_{sub}) and lowest supercritical (A_{sup}) amplitudes for each family are displayed, defining the bounds of the threshold amplitudes.

such result in the present study is found that close to the threshold for the oblate ($A < 0$) off-center families a separated pair of horizons also appears. These AHs are situated approximately around the two biggest peaks of the Kretschmann scalar along the symmetry axis and form (forming a binary BH spacetime if the event horizon shows two components, but event horizons are not investigated in this work). In

Fig. 4.6 this behavior is shown for the oblate ($A < 0$), off-centered family $\rho_0 = 4$ with amplitude $A = -0.0757$. Note that such a feature only appears when tuning close enough to the threshold. As proof look at Fig. 4.5, corresponding to the same family as Fig. 4.6 but further from the threshold, with amplitude $A = -0.0780$. In that case, a single AH formed situated at the origin and coinciding with the largest peak of the Kretschmann scalar for such evolution. This is evidence that the dynamics change as one approaches to the threshold of collapse. Due to the reflection symmetry of the initial data, the two horizons from Fig. 4.6 are perfect copies, symmetric about the equator.

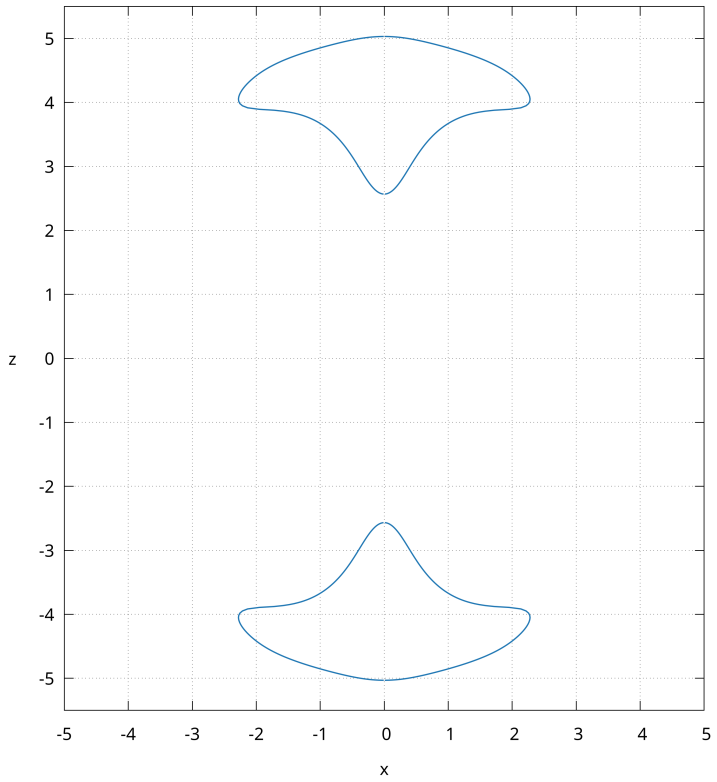

Figure 4.6: In this figure the bifurcation of an AH found by `ahloc3d` is shown. The horizontal axis represents the x direction and the vertical axis represents the symmetry axis, z. This is for the specific oblate off-centered family $A < 0$, $\rho_0 = 4$ with amplitude $A = -0.07570$ at time $t \simeq 25.8$. Comparing, for example, with Fig. 4 of [58] one can see that the AHs are off-set by a greater coordinate distance.

For the interested reader, in Appendix G there are shown the AHs corresponding to the other off-center families as close to the threshold as possible, corresponding to the values of the amplitude from Table 4.1. There one can see that in the case of the prolate ($A > 0$) off-center data there is a single AHs centered at the origin. To see a pair of AHs as one approaches the threshold, the `ahloc3d` software needs to be run close enough to the time of formation of the AH, as shortly after trapped surface formation the code will fail, making a difficult post-

processing task to hit the right time to search. In the present work explicit evidence of two disjoint AHs forming in the prolate off-center families is not given, however, strong indications are suggesting that this is a common feature for all the six studied families. Close enough to the threshold the global peak of the Kretschmann scalar always occurs, both for subcritical and supercritical cases, away from the origin and along the symmetry axis. Furthermore, as it is shown in Fig. 4.7, when facing difficulties with `ahloc3d` some abnormal shapes that are not trustworthy as AH were found, however, such a shape seems to indicate that a bifurcation is about to occur. This limitation is a clear sign that the software needs improvement. It is worth commenting here as well, that presumably, if one chooses initial data that does not have reflection symmetry and then tunes well enough to the threshold, a single AH could form away from the origin along the symmetry axis. Nevertheless, this option needs further investigation.

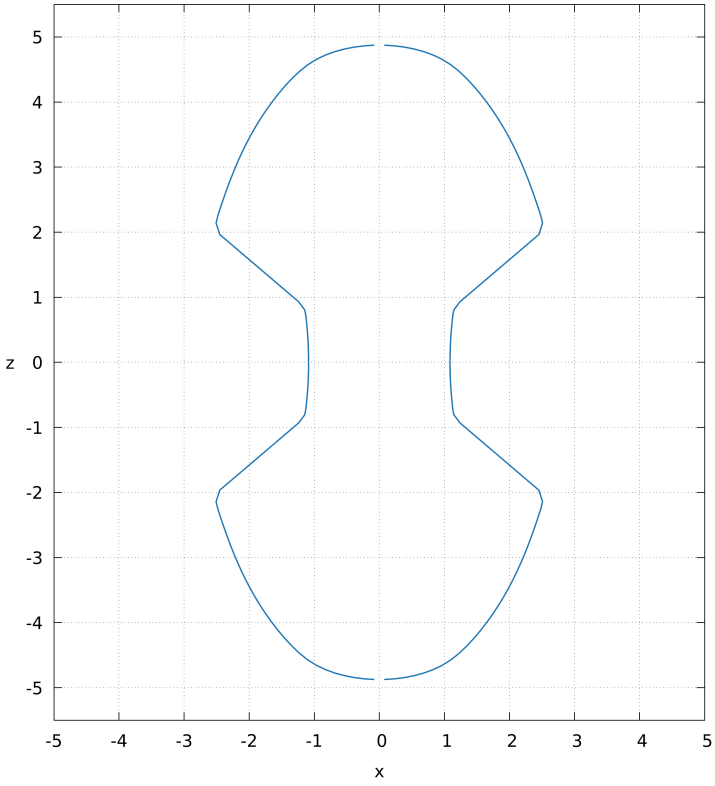

Figure 4.7: In this figure an abnormal shape for the output of the software `ahloc3d` is shown. The horizontal axis represents the x direction and the vertical axis represents the symmetry axis, z. This is for the specific prolate off-centered family $A > 0$, $\rho_0 = 4$ with amplitude $A = 0.09860$ at time $t \simeq 21.56$. This outcome it is not considered as a trustworthy AH due to lack of resolution in the curve.

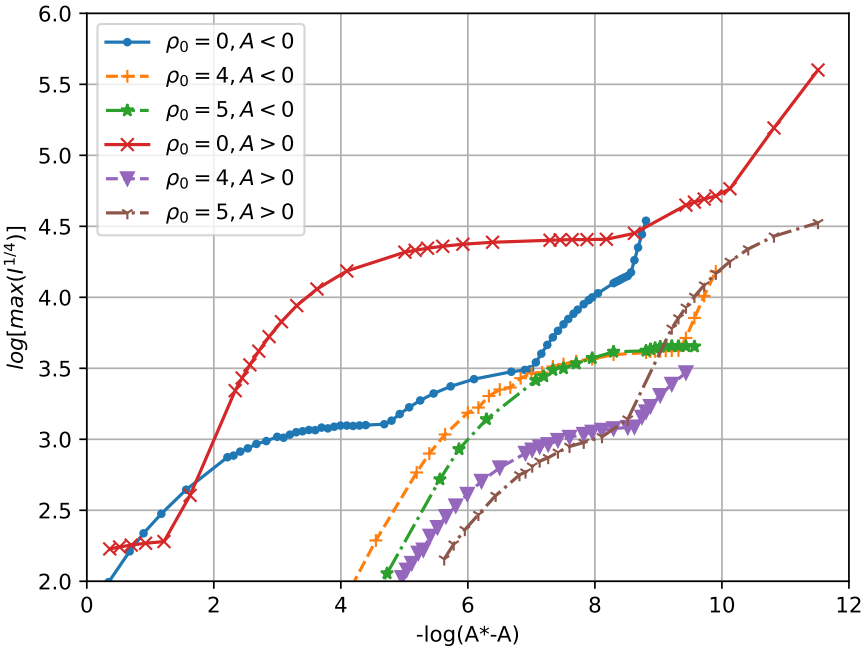

Figure 4.8: The scaling of the Kretschmann scalar for all the studied families is shown. In the horizontal axis the logarithmic distance to the critical point is represented and in the vertical axis there is the logarithm of the maximum of the Kretschmann as $I^{(1/4)}$ in units of length. The red curve compares with Fig. 4 of [58] and the blue with the green in Fig. 1 of [51].

4.3.3 *Scaling*

According to [37], if critical phenomena are present in the collapse of GWs in vacuum, any curvature scalar invariant should show universal power-law scaling like 4.2 in the subcritical regime. As this setup corresponds to vacuum the Ricci scalar vanishes, therefore the argument above applies to the Kretschmann scalar. In Fig. 4.8 a plot of the Kretschmann scalar as $I^{1/4}$ against the logarithmic distance to the critical point is shown. First, it is clear that the maximum value that the Kretschmann scalar attains depends on the amplitude of the initial data for each family. Second, for each family this result is compatible with the power-law behavior from Eq. 4.2, and agrees very well with [51, 58] for the two centered families. There is, however, no evidence of a universal exponent. A priori, this result is compatible with each family having a different exponent, but, extending these lines further to the right (which is very computationally expensive and challenging) would be necessary to make a conclusive statement about universality. If the exponents were truly different, one could wonder whether there exists a finite number of such exponents, leading to a new paradigm of universality, or else, if there are simply as many exponents as families

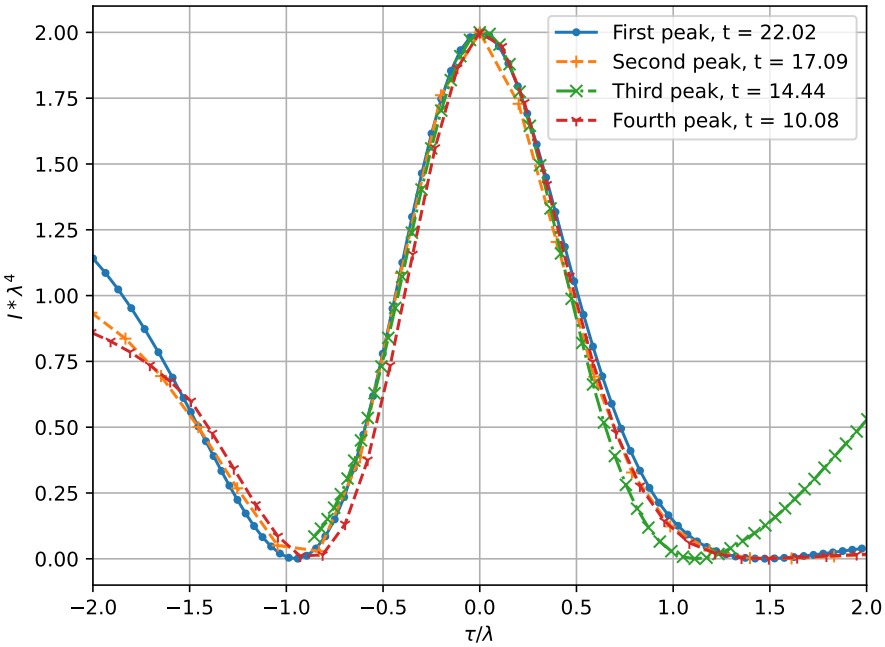

Figure 4.9: In this figure four echoes for the family of initial data $A < 0$, $\rho_0 = 0$ with $A = -3.50909$ are shown. Each echo corresponds to a peak of the maximum of the Kretschmann scalar which happens at different times against the proper time. Both axes are rescaled for each curve by a constant λ which is chosen such that the maximum will correspond to 2 in the plot. The largest ratio of λ's across such curves is ~ 3.

of initial data. Evidently, more investigation is needed. Referring to DSS, only one family (the blue curve in Fig. 4.8) shows enough periods for claiming that it behaves as *approximately*-DSS and more periods are needed in the other families. This is also the reason why treating the errors is postponed and the interpretation of this result as qualitative for now.

4.3.4 *Echoes and universality*

In the case of a minimally coupled real massless scalar field collapse in spherical symmetry [17], the critical solutions show DSS behavior, however, in the axisymmetric collapse of GWs in vacuum the picture is more complicated. As discussed above, it is observed that for a near threshold evolution $A \lesssim A_\star$ (flipped for oblate $A < 0$ families), several large local peaks in the Kretschmann scalar occur along the symmetry axis before the data eventually disperse. In Fig. 4.9 these peaks are plotted against the proper time along timelike curves (the integral curves of the unit normal vector n^a) that pass through the

maxima (one curve per peak), and compare them by rescaling them with a constant λ so that dimensionless quantities are plotted in both axes. Due to the coordinates that are used in the present work the shift is non-zero, and in order to calculate the integral curve of n_a

$$\begin{aligned} \dot{\tau}(t) &= \alpha(x^\mu(t)) + constant, \\ \dot{x}^i(t) &= -\beta^i(x^\mu(t)), \end{aligned} \tag{4.11}$$

needs to be solved, where $\tau(t)$ is the proper time, α is the lapse, β^i is the shift (see Section 1.2 for definitions) and x^i the integral curve parametrized by t. In Fig. 4.9 the oblate ($A < 0$) centered family $\rho_0 = 0$ is taken as it is the one in which the highest number of echoes was found. In Appendix H the analogous plots are shown for the rest of the families. As one can see, the agreement is not as clear as in Fig. 4.9 for the rest of the families, however, given that $A - A_\star$ has no absolute meaning, one can argue that for the other families the data is not as close to the threshold solution to show as good results as Fig. 4.9. This is consistent with Fig. 4.8 where the family displaying a larger number of periods is also the prolate ($A > 0$) centered one. In these figures it is allowed the freedom to flip individual curves to take care of features propagating up or down the z-axis. The agreement of the four curves in Fig. 4.9 is striking, especially given that the values of λ for each of the curves vary by a factor of ~ 3, corresponding to a little less than two orders of magnitude in the Kretschmann scalar itself. Four echoes were found for four different times, in agreement with [51]. It is important to remark, again, that this feature is exclusive to near threshold evolutions. Serve as proof that fewer echoes are appearing for the other families as shown in Appendix H and that for small initial data only one peak of the Kretschmann scalar occurs, and no such repeated feature appears. On the symmetry axis, the scalar quantity studied by Ledvinka and Khirnov in [51] is directly related to the Kretschmann scalar. One might expect their profiles agree with the ones shown here, but, the normal vector associated with the foliation of [51] does not coincide with the one considered in the present work. Thus, the integral curves along which the plot is made do not coincide either. A detailed comparison is then postponed. It was not possible to identify whether these repeated features correspond to true DSS behavior. In the chosen coordinates they appear with no regular time intervals, and the curvature scaling plots from Fig. 4.8 do not indicate universal power-laws nor uniformly periodic wiggles, so there is no reason to expect them to correspond to true DSS. Yet, this is clear evidence of phenomenology familiar from the spherical setting, where the standard picture of critical phenomena applies, carrying over.

In order to compare the spacetime behavior among families, in Fig. 4.10 the profile of the Kretschmann scalar against the proper time along a timelike curve that passes through the maxima is shown for near critical data. Such an integral curve of n_a is build in a neigh-

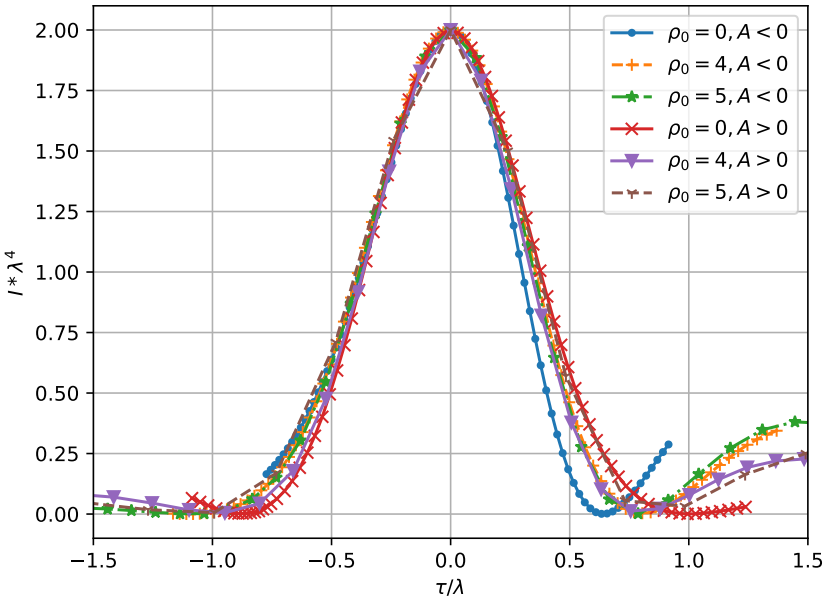

Figure 4.10: In this figure the largest peak of the Kretschmann scalar, for the highest subcritical amplitude of Table 4.1, for each of the six studied families, against the proper time along the integral curve of n^a is shown. As in Fig. 4.9, both the proper time and Kretschmann scalar are rescaled by a constant λ chosen such that the maximum of the Kretschmann scalar occurs at 2 in the plot. For these curves the largest ratio of λ's is around 10, corresponding to a ratio 10^4 in the peak of the Kretschmann itself. The data for the prolate ($A > 0$) off-centered families and for the oblate ($A < 0$) centered family have been flipped along the vertical axis for a better match.

borhood of each large peak. This representation is similar to Fig. 4.9 but now for the largest peak within the best-tuned data within each family (see Table 4.1). Each of these lines corresponds to the most right placed point of Fig. 4.8 for each family, being as close to the threshold solution as possible. Again, the shapes around the peaks agree, showing a common feature that appears when evolving initial data with amplitude $A \simeq A_\star$ independently of the chosen family of initial data, and again, in concordance with [51].

4.4 SUMMARY AND DISCUSSION

The precursor of this work on GW collapse with `bamps` [58] was severely restrained by the rapidly increasing computational cost of the evolutions near the threshold. With an allocation of around 10 million core hours the authors were able to tune just a single family to the threshold of collapse. That is the main reason with since then `bamps`

has undergone a major rebuild, and now it fully supports AMR (which details will appear soon in an independent report). In the present work, with a similar allocation it was possible to tune six families within a comparable distance to the threshold of collapse. Be aware that so far this is the work in which more families of initial data are investigated.

There is an obvious question to make here. If now there exists this additional efficiency why it is not pushed already one (or more) families closer to the threshold? The answer is that there are still other complications. During the development of this work difficulties were encountered in the bisection, and in particular, classifying spacetimes close to the threshold. The main two reasons for this are, first, it is not possible to prevent the formation of coordinate singularities, which no amount of AMR could overcome. These coordinate singularities would prevent classification if they appear before trapped surface formation. The choice of the gauge parameter η_S as defined in Eq. 4.5 appears to be highly important. Related to this there is the presence of constraint violation, which gets worse in the strong-field regime and especially when fine features appear, but this is not likely to be the leading problem in the present data. As expected, the evolutions near the threshold of collapse are numerically more challenging and constraint violation gets worse. Usually the constraint violation stays in a range of about 10^{-8} to 10^{-6} for small initial data. However, when the Kretschmann scalar grows this violation can reach up to 10^{-3}, but still remains several orders of magnitude smaller than the relevant evolved quantities. The second issue was that, in particular for the off-centered families, the shapes of the AHs change drastically the closer one gets to the threshold. It is suspected that there may be AHs which can not be captured by `ahloc3d` due to the Strahlkörper representation described in Section 4.2.3. Fortunately, strategies are available to avoid both of these issues in the future.

Despite the above mentioned shortcomings, the current setup allows rigorous examination of the threshold of BH formation of axisymmetric GWs. Close to the threshold, it was found explicitly that two of the four off-centered families form two disjoint AHs, in agreement with [51, 58] for the centered families. In the remaining two families of off-center data, the expectation is that the same happens due to the spikes in the Kretschmann scalar form away from the origin and along the symmetry axis. These spikes are further separated for off-center data than for centered data. This is not surprising, since the seed functions were off-set in the cylindrical polar direction ρ, the waves have time to propagate in the z-direction before they hit the symmetry axis. It would be interesting to study initial data families off-set in both ρ and z to examine how generic the appearance of pairs of AH is within families of reflection symmetry data. However, with the

(constraint solved) Teukolsky waves from [51] and the present work, the appearance of a par of AHs does seem a fairly robust feature.

The results for the scaling of the Kretschmann scalar shown in Fig. 4.8 agree perfectly with [51, 58], enhancing confidence that the code is reliable as the results for centered Brill waves were reproduced. The main objective was to help establish the extent to which the standard picture of critical collapse extends beyond spherical symmetry. As discussed in Section 1.5, a number of studies suggest that this story is a subtle one, where the present work reinforces this perspective. Four families of off-center initial data were examined for first time. Considering the scaling plot for each family individually, it is tempting to argue that the data take the form of a power-law plus a possibly periodic wiggle. But at least to the level of tuning that is presented here, there appears to be neither a universal power nor period in the wiggle. It might be possible that greater numerical accuracy is needed, but given the solid agreement with the independent implementation in [51] that does seem unlikely. The available evidence at this point suggests that the exponents of the respective power-laws and the periods of the wiggles (if the latter can even be defined), are family dependent. Presumably, this corresponds to the manifestation of different threshold solutions, and so departs from the standard picture of critical phenomena in spherical symmetry (see Section 1.3.1).

Most interestingly, the evidence strongly suggests that aspects of behavior familiar from the spherical setting do carry over. Looking at Fig. 4.10, it is clear that, close enough to the threshold solution, all six families present strikingly similar behavior for the Kretschmann scalar. A peak of practically the same shape appears at different scales. This is a clear indication that some kind of universality still remains. This is, furthermore, in good agreement with the findings by [51] for alternative families of initial data. Likewise it was also found that within individual families, those repeated echoes appear in the curvature scalar.

There are a number of obvious ways in which to extend this work. First, improvements to `ahloc3d` are needed so that the AHs that do not follow the Strahlkörper parametrization can be found. See [112], where the same problem was faced, for a possible solution. It could be possible to analyze even the sets of data that were inconclusive to classify in this work and also to push the same bisection further. Next, is the treatment of alternative families, including radially offset Brill waves and (constraint solved) Teukolsky waves. It is also expected that finer control of constraint violation and coordinates would be of benefit. For the latter, DF-GHG [113–115] formulation is already implemented, but the complete generalization of the outer boundary conditions to that setting is still ongoing. A further question, already mentioned in passing in [58], is whether or not the curvature spikes that are observed have anything to do with BKL behavior. As

such, following [116], it would be interesting to calculate the expected behavior of the Kretschmann scalar for comparison. Ultimately, as `bamps` undergoes further development, in the future it is expected to relax the symmetry assumptions and make full-3d evolutions at the threshold of vacuum collapse. Progress on all of these points will be reported elsewhere.

CONCLUSION TO THIS MANUSCRIPT

5

FINAL DISCUSSION

The aim of this manuscript is to bring further progress in the study of the critical phenomena in gravitational collapse, particularly, beyond spherical symmetry. As it was introduced in Section 1.5, the standard picture of critical phenomena perfectly applies when restricting to spherically symmetric scenarios, however as one can see through the previous Chapters, when moving to fewer symmetry restrictions, not all the features might carry over.

In the first part of this thesis, a critical phenomena modelling project was explained in Chapter 2. Studying critical phenomena in gravitational collapse is normally done using NR. When focusing on setups that depart from spherical symmetry the complications of a numerical code and the necessary computational cost increases by orders of magnitude. In an attempt to investigate critical collapse without spherical symmetry while side-stepping this handicap, the semilinear wave models from Chapter 2 came to light. These models that replicate the full description of critical phenomena in the spherically symmetric case can be studied in a much more efficient manner. A NR inspired spherical 3+1 code was used to prove that in spherical symmetry all the models vindicate the critical phenomena. Moreover, some of them have an analytical solution, which allowed deeper investigation into the mathematical structure and to straightforwardly obtain threshold solutions in axisymmetry. It was analytically proven that different families of initial data lead to different threshold solutions, departing from the assumption of a universal threshold solution when dropping spherical symmetry. Part of the motivation for this manuscript, but in general to study the critical phenomena in gravitational collapse, was to find counterexamples to the SCC and WCC. In this case, these toy models can not be thought of as a model for WCC, however, one can make some connections with the SCC. For these toy models, it was shown that threshold solutions were more regular than generic blowup solutions, allowing extension beyond the blowup depending on the values of some parameters (ν and γ). Despite the lack of proof, one might wonder how this would apply if it carries over to GR. The answer is that such regularity of the threshold solution would allow numerical simulations which could further investigate the SCC.

The second part of this manuscript returned to GR and implications for the critical collapse of GWs in vacuum were investigated. Two approaches were taken in this part, first, in Chapter 3 the focus was on the linearized initial data for vacuum GWs simulations. Second, in Chapter 4 such simulations were carried out to bring some light to the critical phenomena in gravitational collapse beyond spherical symmetry from a computational approach.

In Chapter 3 two types of vacuum GWs initial data, Brill and Teukolsky waves were introduced in the linear regime. It was found in the literature that these two types of initial data behave differently in numerical simulations, with Brill waves in particular proving difficult in previous works. Moreover, in the scenario of evolving GWs in vacuum, it was shown by [51] and in Chapter 4 that different families of initial data have, a priori, different scaling exponents, which is an indication of different threshold solutions. As suggested by studies of critical phenomena in gravitational collapse with electromagnetic waves [67, 68], initial data families leading to quantitative and qualitative different threshold solutions might be due to the different multipolar structure of the initial data. When treating Brill and Teukolsky waves in the linear regime they also have, in general, different multipoles. Given this assumption, it was worth studying if in the case of GWs in vacuum this difference was also behind the cause of the different behavior of the two types of initial data. By comparing them in the linear regime with three different methods, the outcome was that the most common choice of the Brill data, the Holz data [93] (a Gaussian profile for the seed function), had the same multipolar structure as the Teukolsky waves. Since the two types of initial data purely quadrupolar, it was found that the differences between them were negligible and in any case, not the reason why the numerical outcome of both is so different. It is important to remark that this study was focused on the linear regime, therefore the possible explanation for the discordance might be hidden within the nonlinear part and further research is needed.

In Chapter 4 the canonical approach to critical phenomena in gravitational collapse was undertaken. Using the adaptive pseudospectral NR `bamps` code, vacuum GWs initial data were evolved. As discussed in Section 1.5, the pioneering results from Abrahams and Evans [49, 50] about the critical phenomena in the collapse of GWs in vacuum were never successfully reproduced. Instead, when this scenario was studied in [51, 58] the authors found some departures from the standard understanding of the critical collapse in spherical symmetry. The findings that were exposed in Chapter 4 point in the latter direction. In this setup, there is a clear phase transition in the parameter space when two sets of initial data that are infinitesimally close lead to two distinct end points, one finishing in dispersion and the other in BH formation. However, the properties of the threshold solution lying in between both regimes seem to differ from other gravitational collapse

scenarios in spherical symmetry. Although some universal features remain associated with the spikes of the curvature scalar, one can not say that the scaling exponent for all the families is the same, nor the period of the wiggle, if such a period can even be defined. It was neither possible to confirm a DSS behavior of the near threshold solutions, as the echoes in the curvature do not seem to be periodic, at least, in the chosen coordinates. The code `bamps` had major structural changes that are put into practice in this project, dramatically increasing its efficiency. However other limitations regarding constraint violation, coordinate singularities, and finding AHs in the post-process search arose. As these results are in good agreement with [51], work done with an independent code, the confidence in the accuracy of `bamps` is reinforced. Nevertheless, it would be interesting to have more results from independent codes that can evolve GWs. An example of software that could be used for this purpose is the CoCoNut code, which has proven to be valid to evolve GWs in dynamical spacetimes [117]. Together with Chapter 2 and other independent studies, this is a work that also walks towards changing the paradigm of critical phenomena in gravitational collapse when moving beyond spherical symmetry.

When I enrolled in the PhD that results in this document, there was only one study in the literature suggesting that a more intricate structure could arise in the gravitational critical collapse when moving to fewer symmetry restrictions. Such work [62] dates from 2003, and the only departure from the standard story was the appearance of two centers of collapse when getting close to the threshold. It was only 14 years later when such a feature was reproduced in the collapse of GWs in vacuum [58], a work that came out in November of 2017, practically coinciding with my starting date as a PhD student. Since then, several studies by many authors covered a range of different scenarios to bring some light to the still dark world of critical phenomena in gravitational collapse beyond spherical symmetry. The work presented in this manuscript takes part in that group of studies in the recent past years.

Gravity is a very special field of physics. As an undergraduate student would say, there are two main theories to explain the world as we know it: the Standard Model (SM) of particle physics and GR. The SM can explain three of the four fundamental forces, electromagnetic, weak, and strong, however, gravity does not play a role in there and vice versa. It is well known that both theories apply to different scales. Colloquially, one can say that the SM, as a quantum field theory, applies to the physics of the "very small", and, on the other hand, that GR applies to the physics of "big" scales. So far there is not a unified theory that joins these two ends, as it would be the dream of many of us physicists. Of course, both theories are in constant evaluation to face the shortcomings and experimental evidence that is still unexplained, but the fact that gravity itself needs a separate formalism means, at

least, that things might happen differently to other physical systems. Connecting with critical phenomena in gravitational collapse, one might wonder: Are critical phenomena behaving differently in gravity? Are they even critical phenomena at all? Is this an open door to new physics? With the evidence so far, it is fair to say that this subject is a relatively new field of study, whereas, in other areas of physics, such as statistical mechanics, critical phenomena have been studied for longer. The name of critical phenomena in the gravitational context comes after the seminal work of Choptuik [17], where it was found experimentally that the particular setup of a real massless scalar field minimally coupled in spherical symmetry was sharing the same properties as the critical solutions in statistical mechanics. Since then critical phenomena in gravitational collapse was established as a field of research in its own right. However, the recent discoveries that such phenomenology does not completely carry over beyond spherical symmetry for many gravitational settings makes one wonder whether this is actually critical phenomena that simply works with subtleties in gravity, or if it is something quite different but still of fundamental interest. The work developed during this thesis tried to shed some light on that question and it is part of many studies that will come, as more investigation is needed. Only time will tell the final answer.

Part III

APPENDIX

A

ANGULAR FUNCTIONS AND SEED FUNCTION FOR TEUKOLSKY

$$f_{rr} = 2 - 3\sin^2(\theta) \tag{A.1a}$$
$$f_{r\theta} = -3\sin(\theta)\cos(\theta) \tag{A.1b}$$
$$f^{(1)}_{\theta\theta} = 3\sin^2(\theta) \tag{A.1c}$$
$$f^{(2)}_{\theta\theta} = -1 \tag{A.1d}$$
$$f^{(1)}_{\phi\phi} = -f^{(1)}_{\theta\theta} \tag{A.1e}$$
$$f^{(2)}_{\phi\phi} = 3\sin^2(\theta) - 1. \tag{A.1f}$$

For the coefficients A, B and C the seed function is a linear combination of an outgoing solution $(x = t + r)$ and ingoing $(x = t - r)$. In Chapter 3 a concrete seed function is taken but here in the appendix let us take a more general approach to understand how the coefficients are calculated.

Let the seed function, in general, be:

$$F = F_1(t - r) + F_2(t + r). \tag{A.2}$$

Let us define the derivative:

$$F^{(n)} \equiv \left[\frac{d^n F_1(x)}{dx^n}\right]_{x=t-r} + (-1)^n \left[\frac{d^n F_2(x)}{dx^n}\right]_{x=t+r}. \tag{A.3}$$

The coefficients are then given in terms of the seed function and its derivatives

$$A = 3\left[\frac{F^{(2)}}{r^3} + \frac{3F^{(1)}}{r^4} + \frac{3F}{r^5}\right], \tag{A.4}$$

$$B = -\left[\frac{F^{(3)}}{r^2} + \frac{3F^{(2)}}{r^3} + \frac{6F^{(1)}}{r^4} + \frac{6F}{r^5}\right], \tag{A.5}$$

$$C = \frac{1}{4}\left[\frac{F^{(4)}}{r} + \frac{2F^{(3)}}{r^2} + \frac{9F^{(2)}}{r^3} + \frac{21F^{(1)}}{r^4} + \frac{21F}{r^5}\right]. \tag{A.6}$$

B

SPHERICAL HARMONICS

In this appendix the spherical harmonics that are used in Chapter 3 are shown to facilitate the reading of the chapter.

$$Y_{00}(\theta,\phi) = \frac{1}{2\sqrt{\pi}} \tag{B.1}$$

$$Y_{10}(\theta,\phi) = \frac{1}{2}\sqrt{\frac{3}{\pi}}\cos(\theta) \tag{B.2}$$

$$Y_{20}(\theta,\phi) = \frac{1}{4}\sqrt{\frac{5}{\pi}}\left(3\cos^2(\theta)-1\right) \tag{B.3}$$

$$Y_{30}(\theta,\phi) = \frac{1}{4}\sqrt{\frac{7}{\pi}}\left(5\cos^3(\theta)-3\cos(\theta)\right) \tag{B.4}$$

$$Y_{11}(\theta,\phi) = -\frac{1}{2}\sqrt{\frac{3}{2\pi}}e^{i\phi}\sin(\theta) \tag{B.5}$$

$$Y_{1-1}(\theta,\phi) = \frac{1}{2}\sqrt{\frac{3}{2\pi}}e^{-i\phi}\sin(\theta) \tag{B.6}$$

$$Y_{31}(\theta,\phi) = -\frac{1}{8}\sqrt{\frac{21}{\pi}}e^{i\phi}\sin(\theta)\left(5\cos^2(\theta)-1\right) \tag{B.7}$$

$$Y_{3-1}(\theta,\phi) = \frac{1}{8}\sqrt{\frac{21}{\pi}}e^{-i\phi}\sin(\theta)\left(5\cos^2(\theta)-1\right) \tag{B.8}$$

C

CONSTRUCTION OF MONCRIEF FUNCTIONS

C.1 AUXILIARY ANGULAR FUNCTIONS

In the construction of the gauge-invariant Moncrief functions it is useful to express the components of the tensor spherical harmonics in terms of the functions

$$W_{\ell m} = \left(\partial_\theta^2 - \cot\theta\,\partial_\theta - \frac{1}{\sin^2\theta}\partial^2\phi\right) Y_{\ell m} \tag{C.1a}$$

$$X_{\ell m} = 2\partial_\phi\left(\partial_\theta - \cot\theta\right) Y_{\ell m} \tag{C.1b}$$

(see, e.g., Section 9.4.1 and Appendix D in [10]). For $\ell = 2$ and $m = 0$, these functions reduce to

$$W_{20} = \frac{3}{2}\sqrt{\frac{5}{\pi}}\sin^2(\theta) \tag{C.2a}$$

$$X_{20} = 0 \tag{C.2b}$$

C.1.1 *Teukolsky waves*

As one might expect for an axisymmetric, purely quadrupolar wave, the only non-vanishing terms for the Teukolsky wave of Section 3.1.1 are those with $\ell = 2$ and $m = 0$. From Eqs. (9.78) through (9.81) in [10] the functions H_{220}, h_{120}, K_{20}, and G_{20} are computed and shown in Figs. C.1, C.2, C.3 and C.4

$$H^T_{220} = -96\sqrt{\frac{\pi}{5}}\mathcal{A}_T e^{-(r/\lambda)^2} \tag{C.3a}$$

$$h^T_{120} = \sqrt{\frac{\pi}{5}}\frac{16\mathcal{A}_T}{\lambda^2} r e^{-(r/\lambda)^2}\left(2r^2 - 3\lambda^2\right) \tag{C.3b}$$

$$K^T_{20} = 48\sqrt{\frac{\pi}{5}}\mathcal{A}_T e^{-(r/\lambda)^2} \tag{C.3c}$$

$$G^T_{20} = -\sqrt{\frac{\pi}{5}}\frac{8\mathcal{A}_T}{\lambda^4} e^{-(r/\lambda)^2}\left(2r^4 - 8\lambda^2 r^2 + 3\lambda^4\right). \tag{C.3d}$$

Following (9.88) and (9.89) it is possible to then combine these functions, to form

$$k^T_{120} = \sqrt{\frac{\pi}{5}}\frac{32\mathcal{A}_T r^2}{\lambda^6} e^{-(r/\lambda)^2}\left(2r^4 - 15\lambda^2 r^2 + 21\lambda^4\right) \tag{C.4a}$$

$$k^T_{220} = -\sqrt{\frac{\pi}{5}}\frac{48\mathcal{A}_T r^2}{\lambda^6} e^{-(r/\lambda)^2}\left(2r^4 - 13\lambda^2 r^2 + 14\lambda^4\right), \tag{C.4b}$$

which are shown in Figs. C.5 and C.6.

Finally, the gauge-invariant Moncrief function R_{20} for the Teukolsky wave of Section 3.1.1, computed from (9.87) in [10], is given by

$$R^T_{20} = -\sqrt{\frac{\pi}{5}}\frac{8\mathcal{A}_T r^3}{\lambda^4} e^{-(r/\lambda)^2}\left(2r^2 - 7\lambda^2\right) \tag{C.5}$$

(see also exercise 9.7 in [10]).

C.1.2 *Brill waves*

For the Brill waves of Section 3.1.2 the analog computation

$$H^B_{220} = \sqrt{\frac{\pi}{5}}\frac{\mathcal{A}_B}{r^3}\Big[\frac{e^{-(r/\sigma)^2}}{3\sigma^2}(4r^5 + 2r^3\sigma^2 - 3r\sigma^4) - \sqrt{\pi}\frac{\sigma^3}{2}\mathrm{erf}\left(\frac{r}{\sigma}\right)\Big] \tag{C.6a}$$

$$h^B_{120} = 0 \tag{C.6b}$$

$$K^B_{20} = \sqrt{\frac{\pi}{5}}\frac{\mathcal{A}_B}{6r^2}\Big[2e^{-(r/\sigma)^2}\left(2r^2 + 3\sigma^2\right) - \frac{3\sqrt{\pi}\sigma^3}{r}\mathrm{erf}\left(\frac{r}{\sigma}\right)\Big] \tag{C.6c}$$

$$G^B_{20} = \sqrt{\frac{\pi}{5}}\frac{2\mathcal{A}_B}{3\sigma^2} r^2 e^{-(r/\sigma)^2}, \tag{C.6d}$$

and then combine these functions to find

$$k^B_{120} = -\sqrt{\frac{\pi}{5}}\frac{\mathcal{A}_B}{6r^3\sigma^4}\Big[3\sqrt{\pi}\sigma^7\mathrm{erf}\left(\frac{r}{\sigma}\right) + e^{-(r/\sigma)^2}\left(16r^7 - 40r^5\sigma^2 - 4r^3\sigma^4 - 6r\sigma^6\right)\Big] \tag{C.7a}$$

$$k^B_{220} = \sqrt{\frac{\pi}{5}}\frac{\mathcal{A}_B}{4r^3\sigma^4}\Big[-3\sqrt{\pi}\sigma^7\mathrm{erf}\left(\frac{r}{\sigma}\right) + e^{-(r/\sigma)^2}\left(16r^7 - 24r^5\sigma^2 + 4r^3\sigma^4 + 6r\sigma^6\right)\Big]. \tag{C.7b}$$

All these intermediate functions are shown in the figures at the end of this Appendix.

The gauge-invariant Moncrief function R_{20} is then given by

$$R^B_{20} = \sqrt{\frac{\pi}{5}}\frac{\mathcal{A}_B}{12r^2\sigma^2}\Big[2re^{-(r/\sigma)^2}\left(4r^4 + 2r^2\sigma^2 + 3\sigma^4\right) - 3\sqrt{\pi}\sigma^5\mathrm{erf}\left(\frac{r}{\sigma}\right)\Big]. \tag{C.8}$$

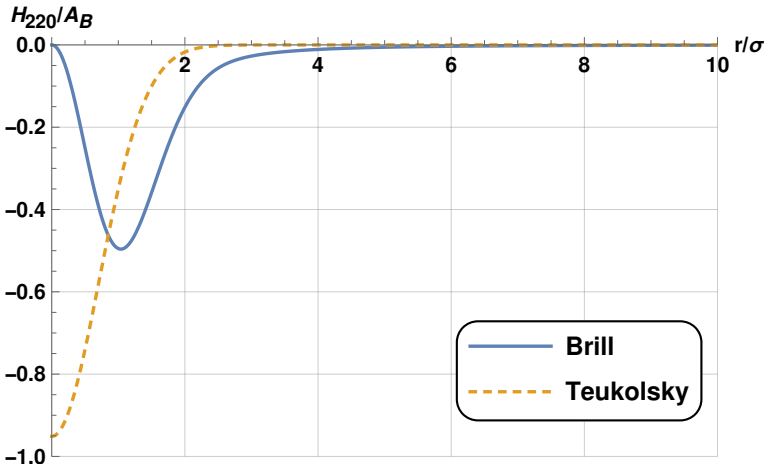

Figure C.1: The intermediate function H_{220} to build R_{20} divided by $\mathcal{A}_B$ is shown for both Brill and Teukolsky data. It was assumed $\sigma = \lambda$ and $\mathcal{A}_T = \mathcal{A}_B/80$.

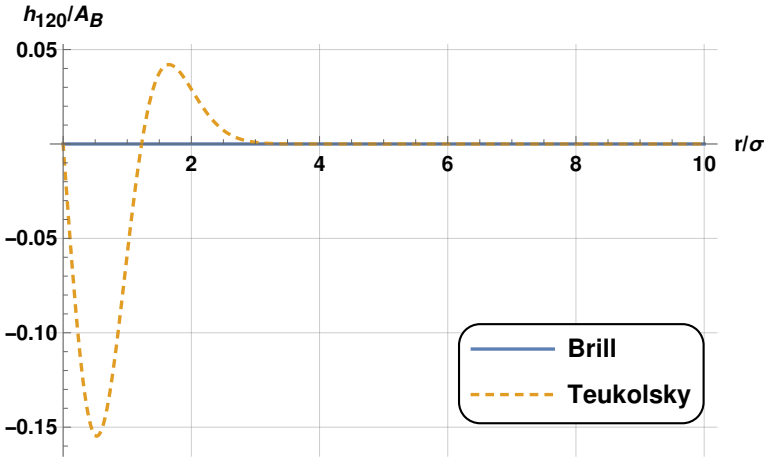

Figure C.2: The intermediate function h_{120} to build R_{20} divided by $\mathcal{A}_B$ is shown for both Brill and Teukolsky data. It was assumed $\sigma = \lambda$ and $\mathcal{A}_T = \mathcal{A}_B/80$.

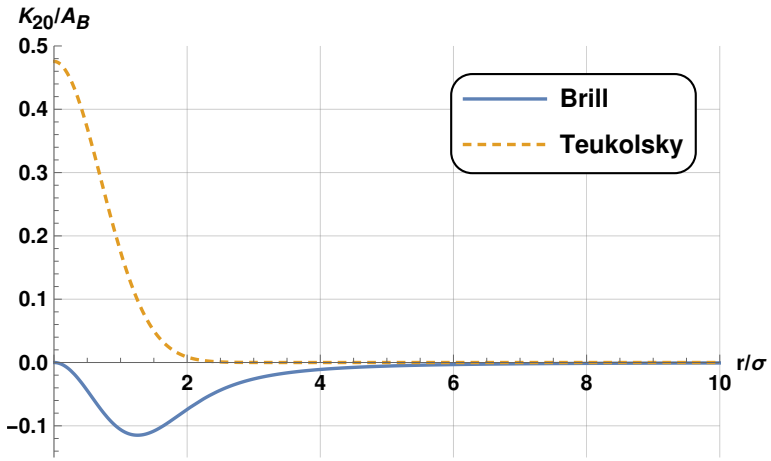

Figure C.3: The intermediate function K_{20} to build R_{20} divided by $\mathcal{A}_B$ is shown for both Brill and Teukolsky data. It was assumed $\sigma = \lambda$ and $\mathcal{A}_T = \mathcal{A}_B/80$.

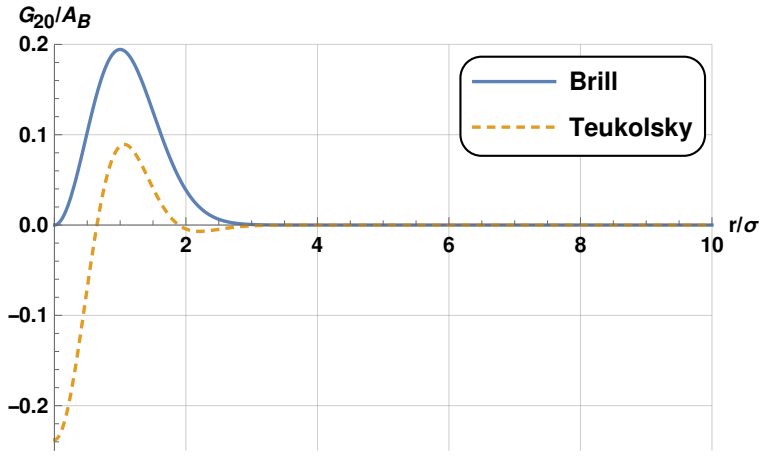

Figure C.4: The intermediate function G_{20} to build R_{20} divided by $\mathcal{A}_B$ is shown for both Brill and Teukolsky data. It was assumed $\sigma = \lambda$ and $\mathcal{A}_T = \mathcal{A}_B/80$.

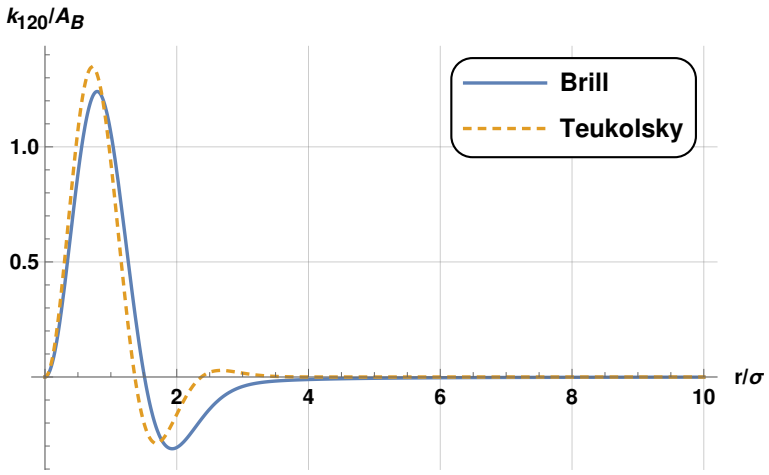

Figure C.5: The intermediate function k_{120} to build R_{20} divided by $\mathcal{A}_B$ is shown for both Brill and Teukolsky data. It was assumed $\sigma = \lambda$ and $\mathcal{A}_T = \mathcal{A}_B/80$.

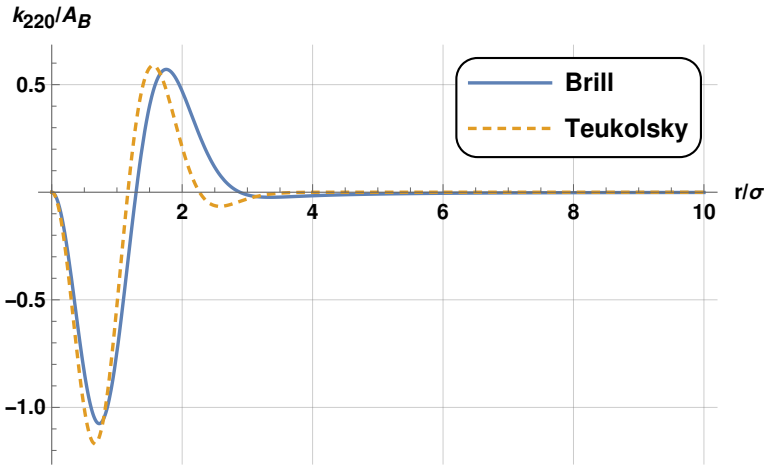

Figure C.6: The intermediate function k_{220} to build R_{20} divided by $\mathcal{A}_B$ is shown for both Brill and Teukolsky data. It was assumed $\sigma = \lambda$ and $\mathcal{A}_T = \mathcal{A}_B/80$.

D

EXPANSION OF $W_{\ell 0}$ IN TERMS OF SPHERICAL HARMONICS $Y_{\ell 0}$

The functions $W_{\ell m}$ may also be written as

$$W_{\ell m} = \ell(\ell+1)Y_{\ell m} + 2\partial_\theta^2 Y_{\ell m} \tag{D.1}$$

(see, e.g., eq. D.12 in [10]). Since the second derivative of $Y_{\ell m}$ with respect to θ can be expressed in terms of spherical harmonics $Y_{\ell' m}$ with $\ell' = \ell - 2$, $\ell' = \ell - 4$ etc., it is possible to see that, for even (odd) ℓ, the $W_{\ell m}$ can be written as a linear combination of all $Y_{\ell' m}$'s with even (odd) ℓ' satisfying $\ell \geq \ell' \geq m$. In axisymmetry, i.e. for $m = 0$, it is possible to derive this linear combination from the properties of Legendre polynomials P_ℓ, which are related to the axisymmetric spherical harmonics by

$$Y_{\ell 0} = \sqrt{\frac{2\ell+1}{4\pi}} P_\ell. \tag{D.2}$$

Starting with the Legendre equation, which may be written in the form

$$\frac{d^2 P_\ell}{d\theta^2} = -\frac{\cos\theta}{\sin\theta}\frac{dP_\ell}{d\theta} - \ell(\ell+1)P_\ell = x\frac{dP_\ell}{dx} - \ell(\ell+1)P_\ell \tag{D.3}$$

where $x \equiv \cos\theta$ in the last step. Using then the recurrence relation

$$xP'_\ell = P'_{\ell-1} + \ell P_\ell \tag{D.4}$$

(see, e.g., Eq. 12.25 in [118]) to find

$$\frac{d^2 P_\ell}{d\theta^2} = P'_{\ell-1} - \ell^2 P_\ell \tag{D.5}$$

Now using the identity

$$P'_{n+1} = P'_{n-1} + (2n+1)P_n \tag{D.6}$$

(see, e.g., 12.23 in [118]) repeatedly. Starting with $n = \ell - 2$, eq. (D.5) becomes

$$\frac{d^2 P_\ell}{d\theta^2} = P'_{\ell-3} + (2\ell-3)P_{\ell-2} - \ell^2 P_\ell, \tag{D.7}$$

next (D.6) is used for $n = \ell - 4$ etc.. Starting with an even ℓ, at some point it ends up with a term P_3', which it is written as

$$P_3' = P_1' + 5P_2 = 5P_2 + P_0, \tag{D.8}$$

where $P_1' = 1 = P_0$ was used. We may therefore write

$$\frac{d^2 P_\ell}{d\theta^2} = \sum_{n=0}^{\ell-2} (2n+1) P_n - \ell^2 P_\ell \qquad (\ell > 2 \text{ even}, n \text{ even}). \tag{D.9}$$

Using (D.2) again

$$\partial_\theta^2 Y_{\ell 0} = -\ell^2 Y_{\ell 0} + \sqrt{2\ell+1} \sum_{n=0}^{\ell-2} \sqrt{2n+1}\, Y_{n0} \qquad (\ell > 2 \text{ even}, n \text{ even}), \tag{D.10}$$

which may be inserted into (D.1) to obtain

$$W_{\ell 0} = \ell\, Y_{\ell 0} + 2\sqrt{2\ell+1} \sum_{n=0}^{\ell-2} \sqrt{2n+1}\, Y_{n0} \qquad (\ell > 2 \text{ even}, n \text{ even}). \tag{D.11}$$

Since the function q in (3.9) contains only monopole and quadrupole terms, only the last two terms in this expansion,

$$W_{\ell 0} = \ldots + 2\sqrt{2\ell+1} \left(\sqrt{5}\, Y_{20} + Y_{00} \right) \quad (\ell > 2 \text{ even}), \tag{D.12}$$

can yield a contribution in the integral (3.65) for $\ell > 2$.

E

COMPONENTS OF THE BRILL AND TEUKOLSKY PERTURBATIONS IN TT GAUGE

For the interested reader here there are presented in Fig. E.1 the non-vanishing components of h_{ab} both for Brill and Teukolsky initial data, in TT gauge, for their respective seed functions 3.8 and 3.2.

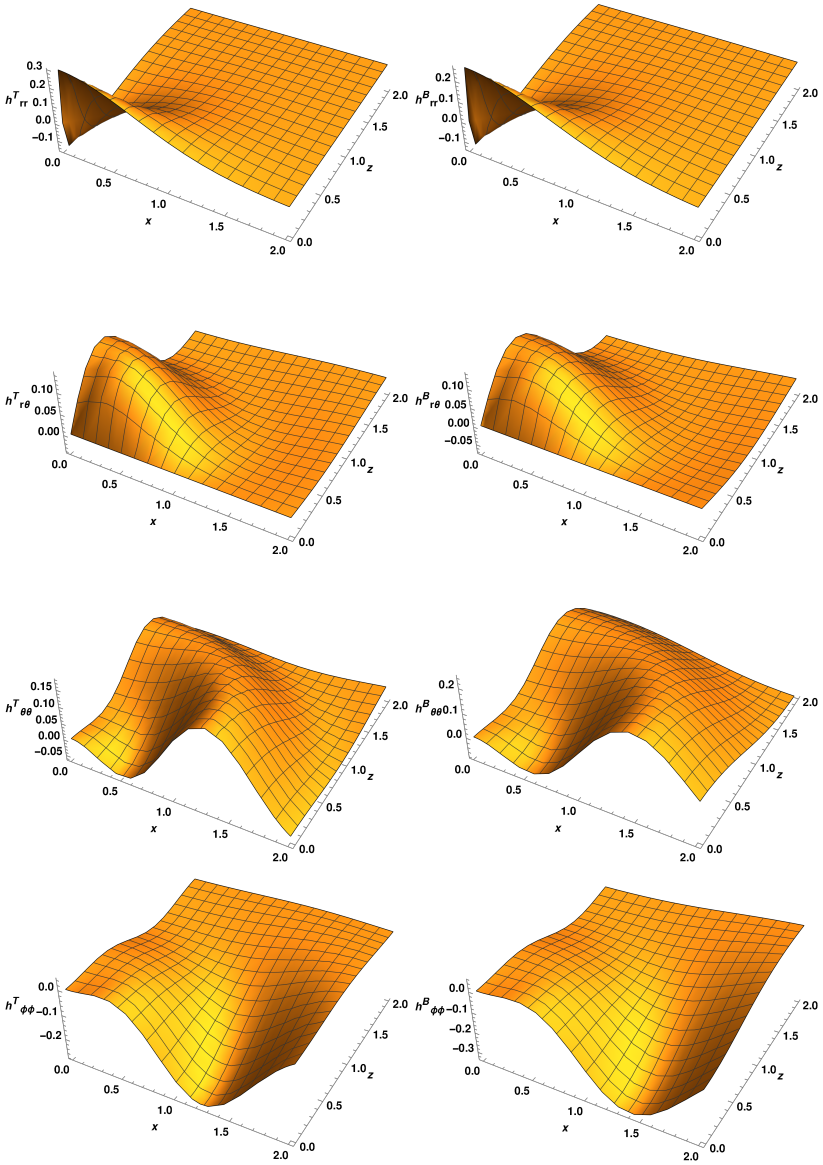

Figure E.1: Non-vanishing components of h_{ab} for Teukolsky and Brill data in TT gauge.

F

COLOR MAPS

In this Appendix the color maps for the logarithm of Kretschmann scalar corresponding to the rest of the studied families in Chapter 4 are shown.

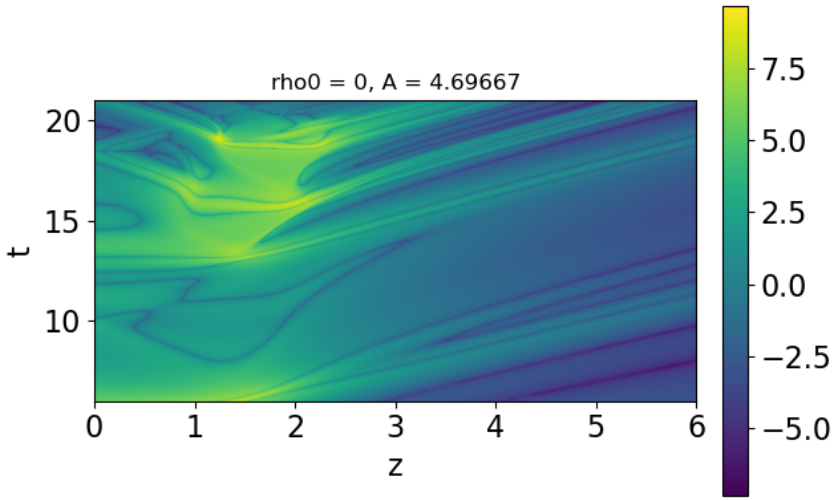

Figure F.1: In this figure a color map of the logarithm of the Kretschmann scalar along the symmetry axis z and through time is shown for the oblate centered family $A > 0$, $\rho_0 = 0$, for the subcritical amplitude $A = 4.69667$.

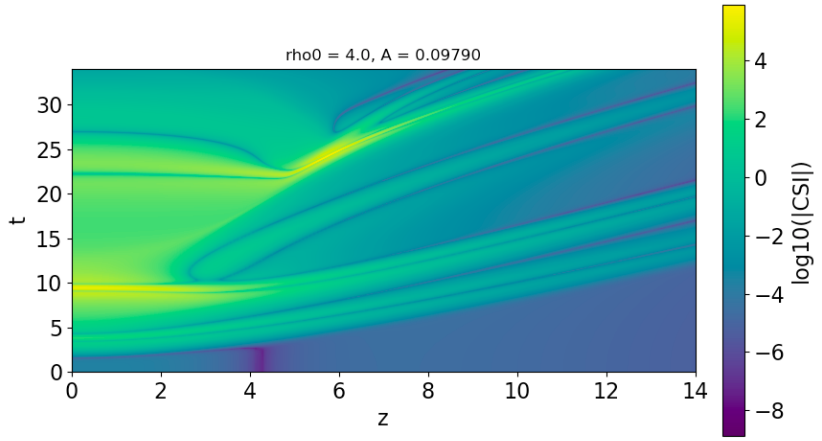

Figure F.2: In this figure a color map of the logarithm of the Kretschmann scalar along the symmetry axis z and through time is shown for the oblate centered family $A > 0$, $\rho_0 = 4$, for the subcritical amplitude $A = 0.09790$.

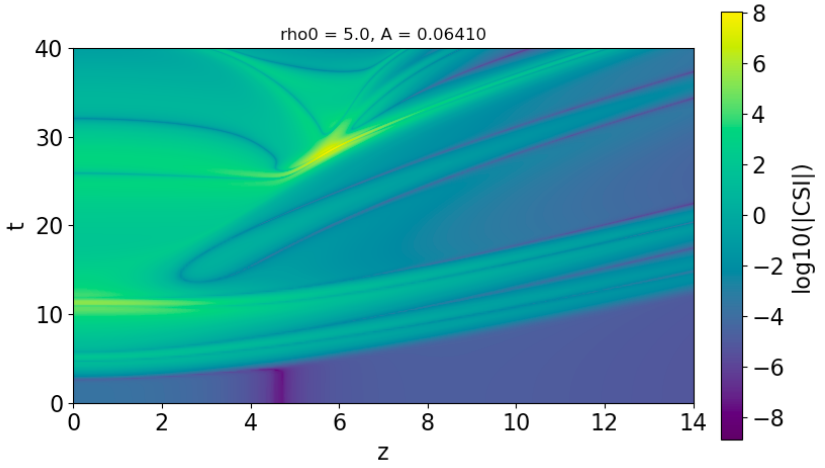

Figure F.3: In this figure a color map of the logarithm of the Kretschmann scalar along the symmetry axis z and through time is shown for the oblate centered family $A > 0$, $\rho_0 = 5$, for the subcritical amplitude $A = 0.06410$.

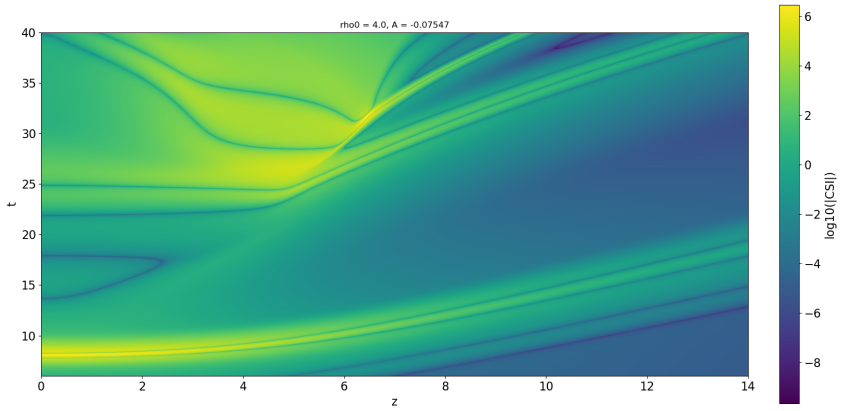

Figure F.4: In this figure a color map of the logarithm of the Kretschmann scalar along the symmetry axis z and through time is shown for the oblate centered family $A < 0$, $\rho_0 = 4$, for the subcritical amplitude $A = -0.07547$.

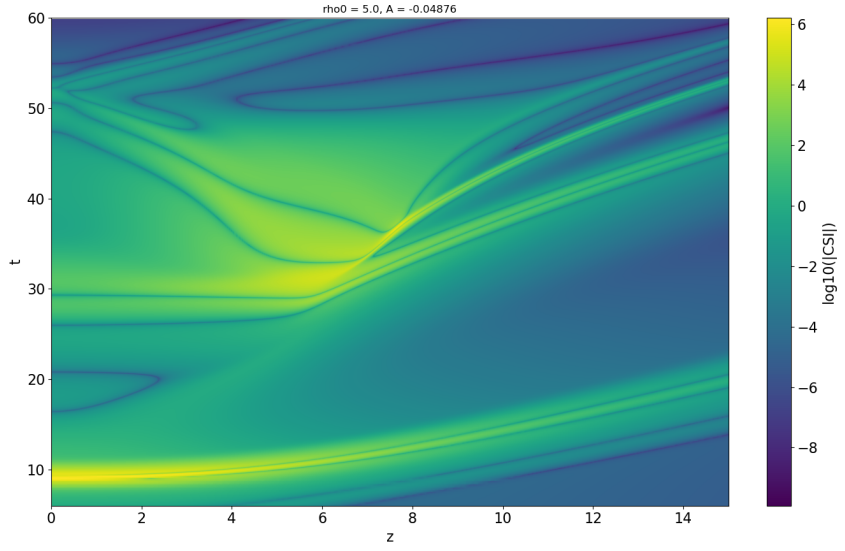

Figure F.5: In this figure a color map of the logarithm of the Kretschmann scalar along the symmetry axis z and through time is shown for the oblate centered family $A < 0$, $\rho_0 = 5$, for the subcritical amplitude $A = -0.04876$.

G

APPARENT HORIZONS

In this Appendix additional AHs are shown. Figs. G.1, G.3 and G.2 correspond to the lowest supercritical run, that is, the closest to threshold that an AH was found, for the rest of the off-centered families that are not shown in Section 4.3.2.

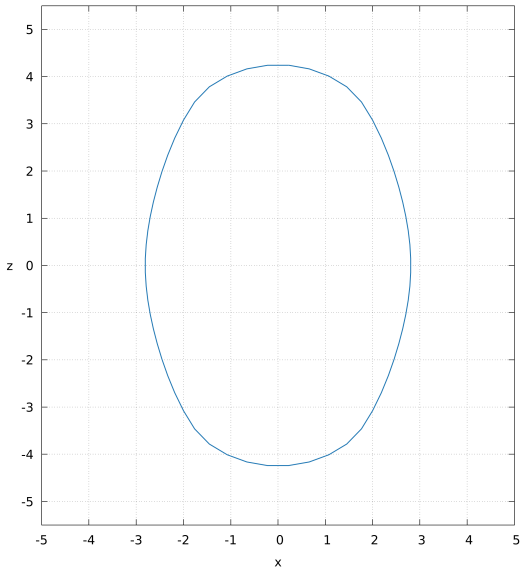

Figure G.1: In this figure an AH found by `ahloc3d` is shown. The horizontal axis represents the x direction and the vertical axis represents the symmetry axis, z. This is for the specific prolate off-centered family $A > 0$, $\rho_0 = 4$ with amplitude $A = 0.09870$ at time $t \simeq 19.55$.

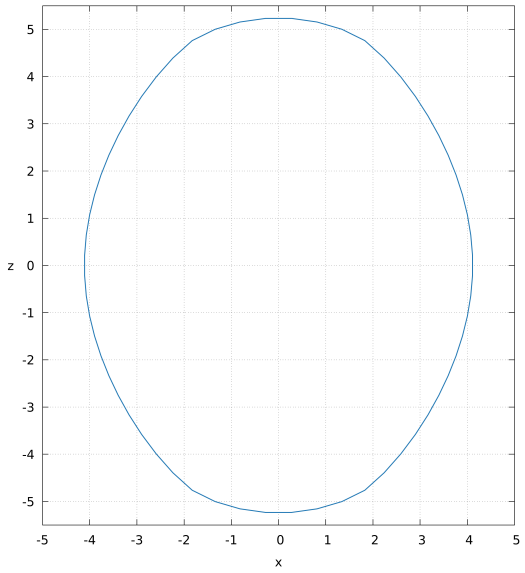

Figure G.2: In this figure an AH found by `ahloc3d` is shown. The horizontal axis represents the x direction and the vertical axis represents the symmetry axis, z. This is for the specific prolate off-centered family $A > 0$, $\rho_0 = 5$ with amplitude $A = 0.0645$ at time $t \simeq 24.06$.

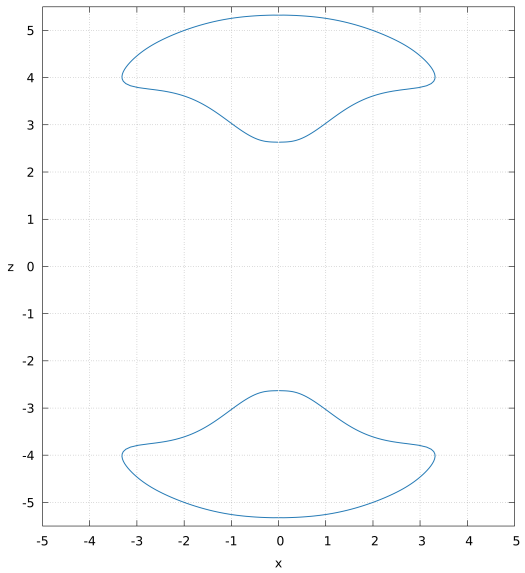

Figure G.3: In this figure a bifurcated AH found by `ahloc3d` is shown. The horizontal axis represents the x direction and the vertical axis represents the symmetry axis, z. This is for the specific oblate off-centered family $A < 0$, $\rho_0 = 5$ with amplitude $A = -0.0490$ at time $t \simeq 29.18$. As in Fig. 4.6 it is possible to observe that the AHs are also separated by a greater distance than in [58].

H

ECHOES

In this Appendix the echoing plots for the rest of the families that are not appearing in Section 4.3.4 are shown.

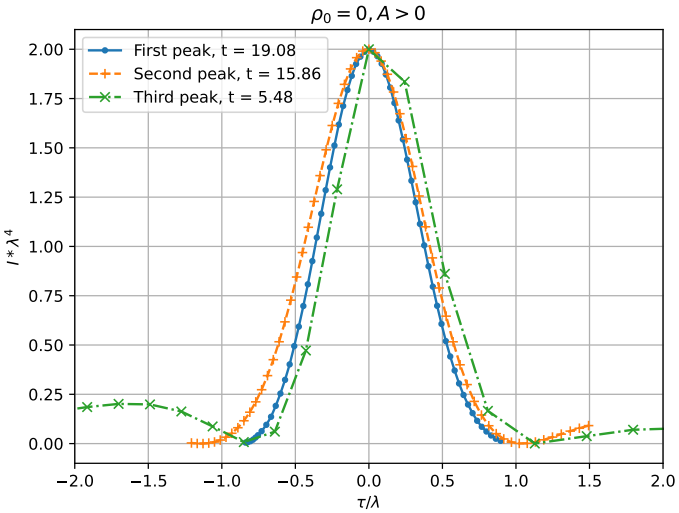

Figure H.1: In this figure four echoes for the family of initial data $A > 0$, $\rho_0 = 0$ with $A = 4.69667$ are shown. Each echo corresponds to a peak of the maximum of the Kretschmann scalar which happens at a different times against the proper time. Both axes are rescaled for each curve by a constant λ which is chosen such that the maximum will correspond to 2 in the plot. The largest ratio of λ's across such curves is ~ 4.

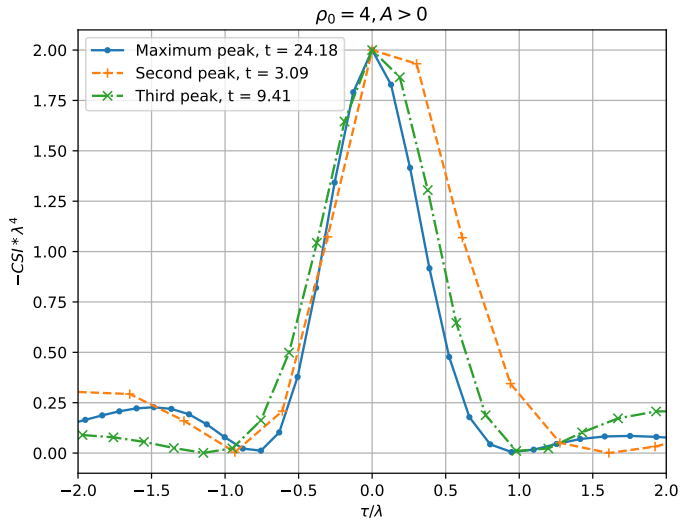

Figure H.2: In this figure four echoes for the family of initial data $A > 0$, $\rho_0 = 4$ with $A = 0.09795$ are shown. Each echo corresponds to a peak of the maximum of the Kretschmann scalar which happens at a different times against the proper time. Both axes are rescaled for each curve by a constant λ which is chosen such that the maximum will correspond to 2 in the plot. The largest ratio of λ's across such curves is ~ 9.

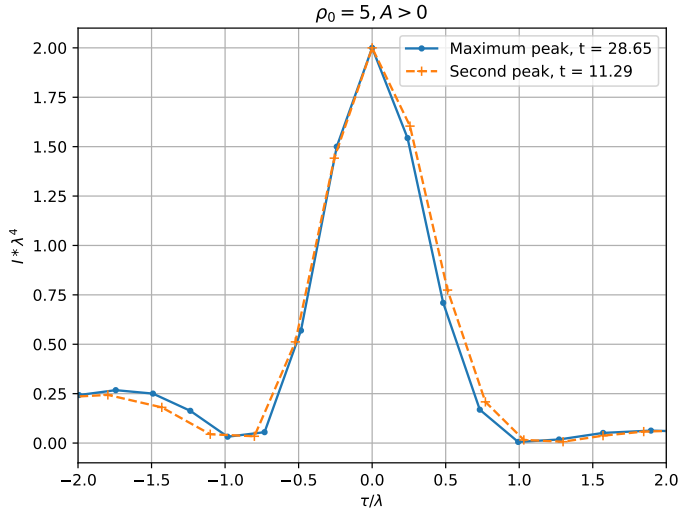

Figure H.3: In this figure four echoes for the family of initial data $A > 0$, $\rho_0 = 5$ with $A = 0.0641$ are shown. Each echo corresponds to a peak of the maximum of the Kretschmann scalar which happens at a different times against the proper time. Both axes are rescaled for each curve by a constant λ which is chosen such that the maximum will correspond to 2 in the plot. The largest ratio of λ's across such curves is ~ 3.

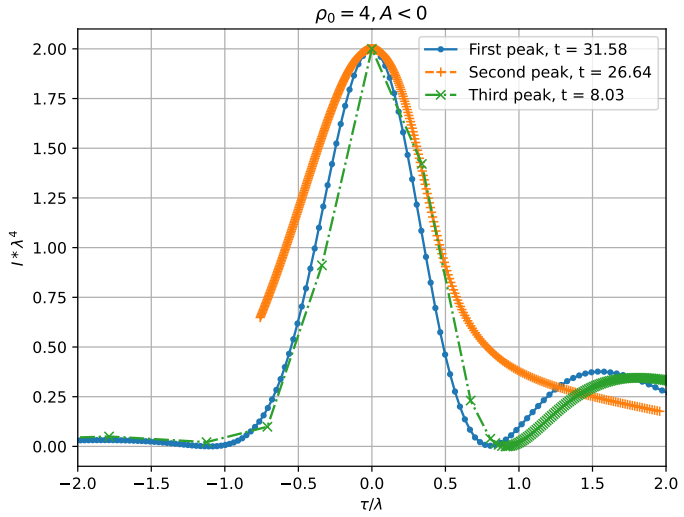

Figure H.4: In this figure four echoes for the family of initial data $A < 0$, $\rho_0 = 4$ with $A = -0.07546$ are shown. Each echo corresponds to a peak of the maximum of the Kretschmann scalar which happens at a different times against the proper time. Both axes are rescaled for each curve by a constant λ which is chosen such that the maximum will correspond to 2 in the plot. The largest ratio of λ's across such curves is ~ 2.

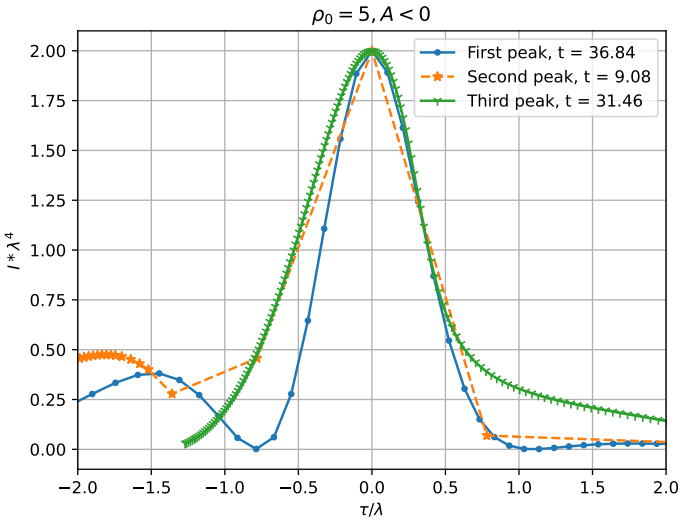

Figure H.5: In this figure four echoes for the family of initial data $A < 0$, $\rho_0 = 5$ with $A = -0.04878$ are shown. Each echo corresponds to a peak of the maximum of the Kretschmann scalar which happens at a different times against the proper time. Both axes are rescaled for each curve by a constant λ which is chosen such that the maximum will correspond to 2 in the plot. The largest ratio of λ's across such curves is ~ 2.

BIBLIOGRAPHY

[1] Vitor Cardoso, Leonardo Gualtieri, Carlos Herdeiro, and Ulrich Sperhake. "Exploring new physics frontiers through numerical relativity." In: *Living Reviews in Relativity* 18.1 (2015), pp. 1–156.

[2] Kip S Thorne, Charles W Misner, and John Archibald Wheeler. *Gravitation*. Freeman San Francisco, 2000.

[3] James B Hartle. *Gravity: an introduction to Einstein's general relativity*. 2003.

[4] Steven Weinberg. "Gravitation and cosmology: principles and applications of the general theory of relativity." In: (1972).

[5] Robert M Wald. *General relativity*. University of Chicago press, 1984.

[6] Yvonne Choquet-Bruhat. *General relativity and the Einstein equations*. OUP Oxford, 2008.

[7] Yvonne Choquet-Bruhat. *Introduction to general relativity, black holes, and cosmology*. Oxford University Press, 2015.

[8] Jose Natario. "Relativity and Singularities - A Short Introduction for Mathematicians." In: (2006). DOI: 10.48550/ARXIV.MATH/0603190. URL: https://arxiv.org/abs/math/0603190.

[9] Jorge A. Rueda and Remo Ruffini. "ON THE INDUCED GRAVITATIONAL COLLAPSE OF A NEUTRON STAR TO A BLACK HOLE BY A TYPE Ib/c SUPERNOVA." In: *The Astrophysical Journal* 758.1 (2012), p. L7. DOI: 10.1088/2041-8205/758/1/l7. URL: https://doi.org/10.1088/2041-8205/758/1/l7.

[10] Thomas W. Baumgarte and Stuart L. Shapiro. *Numerical Relativity: Solving Einstein's Equations on the Computer*. Cambridge University Press, 2010. DOI: 10.1017/CBO9781139193344.

[11] B. P. Abbott et al. "Observation of Gravitational Waves from a Binary Black Hole Merger." In: *Phys. Rev. Lett.* 116 (6 2016), p. 061102. DOI: 10.1103/PhysRevLett.116.061102. URL: https://link.aps.org/doi/10.1103/PhysRevLett.116.061102.

[12] Eric Gourgoulhon. *3+1 Formalism and Bases of Numerical Relativity*. 2007. DOI: 10.48550/ARXIV.GR-QC/0703035. URL: https://arxiv.org/abs/gr-qc/0703035.

[13] Miguel Alcubierre. *Introduction to 3+ 1 numerical relativity*. Vol. 140. OUP Oxford, 2008.

[14] Carles Bona, Carlos Palenzuela-Luque, and Carles Bona-Casas. *Elements of numerical relativity and relativistic hydrodynamics: from Einstein's equations to astrophysical simulations*. Vol. 783. Springer, 2009.

[15] Masaru Shibata. *Numerical relativity*. Vol. 1. World Scientific, 2015.

[16] Ian Hinder et al. "Error-analysis and comparison to analytical models of numerical waveforms produced by the NRAR Collaboration." In: *Classical and Quantum Gravity* 31.2 (2013), p. 025012. DOI: 10.1088/0264-9381/31/2/025012. URL: https://doi.org/10.1088/0264-9381/31/2/025012.

[17] Matthew W. Choptuik. "Universality and scaling in gravitational collapse of a massless scalar field." In: *Phys. Rev. Lett.* 70 (1 1993), pp. 9–12. DOI: 10.1103/PhysRevLett.70.9. URL: https://link.aps.org/doi/10.1103/PhysRevLett.70.9.

[18] Richard Arnowitt, Stanley Deser, and Charles W Misner. "Republication of: The dynamics of general relativity." In: *General Relativity and Gravitation* 40.9 (2008), pp. 1997–2027.

[19] James W York Jr. "Kinematics and dynamics of general relativity." In: *Sources of gravitational radiation* (1979), pp. 83–126.

[20] C. Bona, T. Ledvinka, C. Palenzuela, and M. Žáček. "General-covariant evolution formalism for numerical relativity." In: *Phys. Rev. D* 67 (2003), p. 104005. eprint: gr-qc/0302083.

[21] Daniela Alic, Carles Bona-Casas, Carles Bona, Luciano Rezzolla, and Carlos Palenzuela. "Conformal and covariant formulation of the Z4 system with constraint-violation damping." In: *Phys. Rev. D* 85 (6 2012), p. 064040. DOI: 10.1103/PhysRevD.85.064040. URL: https://link.aps.org/doi/10.1103/PhysRevD.85.064040.

[22] Milton Ruiz, David Hilditch, and Sebastiano Bernuzzi. "Constraint preserving boundary conditions for the Z4c formulation of general relativity." In: *Phys. Rev. D* 83 (2 2011), p. 024025. DOI: 10.1103/PhysRevD.83.024025. URL: https://link.aps.org/doi/10.1103/PhysRevD.83.024025.

[23] Andreas Weyhausen, Sebastiano Bernuzzi, and David Hilditch. "Constraint damping for the Z4c formulation of general relativity." In: *Phys. Rev. D* 85 (2 2012), p. 024038. DOI: 10.1103/PhysRevD.85.024038. URL: https://link.aps.org/doi/10.1103/PhysRevD.85.024038.

[24] Zhoujian Cao and David Hilditch. "Numerical stability of the Z4c formulation of general relativity." In: *Phys. Rev. D* 85 (12 2012), p. 124032. DOI: 10.1103/PhysRevD.85.124032. URL: https://link.aps.org/doi/10.1103/PhysRevD.85.124032.

[25] David Hilditch, Sebastiano Bernuzzi, Marcus Thierfelder, Zhoujian Cao, Wolfgang Tichy, and Bernd Brügmann. "Compact binary evolutions with the Z4c formulation." In: *Phys. Rev. D* 88 (8 2013), p. 084057. DOI: 10.1103/PhysRevD.88.084057. URL: https://link.aps.org/doi/10.1103/PhysRevD.88.084057.

[26] Thomas W. Baumgarte and Stuart L. Shapiro. "Numerical integration of Einstein's field equations." In: *Phys. Rev. D* 59 (2 1998), p. 024007. DOI: 10.1103/PhysRevD.59.024007. URL: https://link.aps.org/doi/10.1103/PhysRevD.59.024007.

[27] Masaru Shibata and Takashi Nakamura. "Evolution of three-dimensional gravitational waves: Harmonic slicing case." In: *Phys. Rev. D* 52 (10 1995), pp. 5428–5444. DOI: 10.1103/PhysRevD.52.5428. URL: https://link.aps.org/doi/10.1103/PhysRevD.52.5428.

[28] Takashi Nakamura, Kenichi Oohara, and Yasufumi Kojima. "General Relativistic Collapse to Black Holes and Gravitational Waves from Black Holes." In: *Progress of Theoretical Physics Supplement* 90 (Jan. 1987), pp. 1–218. ISSN: 0375-9687. DOI: 10.1143/PTPS.90.1. eprint: https://academic.oup.com/ptps/article-pdf/doi/10.1143/PTPS.90.1/5201911/90-1.pdf. URL: https://doi.org/10.1143/PTPS.90.1.

[29] Helmut Friedrich. "On the existence ofn-geodesically complete or future complete solutions of Einstein's field equations with smooth asymptotic structure." In: *Communications in Mathematical Physics* 107.4 (1986), pp. 587–609.

[30] David Garfinkle. "Harmonic coordinate method for simulating generic singularities." In: *Phys. Rev. D* 65 (4 2002), p. 044029. DOI: 10.1103/PhysRevD.65.044029. URL: https://link.aps.org/doi/10.1103/PhysRevD.65.044029.

[31] Frans Pretorius. "Numerical relativity using a generalized harmonic decomposition." In: *Classical and Quantum Gravity* 22.2 (2005), pp. 425–451. DOI: 10.1088/0264-9381/22/2/014. URL: https://doi.org/10.1088/0264-9381/22/2/014.

[32] Heinz-Otto Kreiss and Jeffrey Winicour. "Problems which are well-posed in a generalized sense with applications to the Einstein equations." In: *Class. Quantum Grav.* 23 (2006), S405–S420. eprint: gr-qc/0602051.

[33] Lee Lindblom, Mark A Scheel, Lawrence E Kidder, Robert Owen, and Oliver Rinne. "A new generalized harmonic evolution system." In: *Classical and Quantum Gravity* 23.16 (2006), S447–S462. DOI: 10.1088/0264-9381/23/16/s09. URL: https://doi.org/10.1088/0264-9381/23/16/s09.

[34] David Hilditch, Andreas Weyhausen, and Bernd Brügmann. "Pseudospectral method for gravitational wave collapse." In: *Phys. Rev. D* 93 (6 2016), p. 063006. DOI: 10.1103/PhysRevD.93.063006. URL: https://link.aps.org/doi/10.1103/PhysRevD.93.063006.

[35] Carsten Gundlach. "Critical phenomena in gravitational collapse." In: *Physics Reports* 376.6 (2003), pp. 339–405.

[36] Carsten Gundlach and Jose M Martin-Garcia. "Critical phenomena in gravitational collapse." In: *Living Reviews in Relativity* 10.1 (2007), pp. 1–57.

[37] David Garfinkle and G. Comer Duncan. "Scaling of curvature in subcritical gravitational collapse." In: *Phys. Rev. D* 58 (6 1998), p. 064024. DOI: 10.1103/PhysRevD.58.064024. URL: https://link.aps.org/doi/10.1103/PhysRevD.58.064024.

[38] Matthew W Choptuik, Tadeusz Chmaj, and Piotr Bizoń. "Critical behavior in gravitational collapse of a Yang-Mills field." In: *Physical review letters* 77.3 (1996), p. 424.

[39] Carsten Gundlach. "Critical phenomena in gravitational collapse." In: *Adv. Theor. Math. Phys.* 2 (1998), pp. 1–49. DOI: 10.4310/ATMP.1998.v2.n1.a1. arXiv: gr-qc/9712084.

[40] Patrick R Brady, Chris M Chambers, and Sergio MCV Goncalves. "Phases of massive scalar field collapse." In: *Physical Review D* 56.10 (1997), R6057.

[41] Scott C. Noble and Matthew W. Choptuik. "Driven neutron star collapse: Type I critical phenomena and the initial black hole mass distribution." In: *Phys. Rev. D* 93 (2 2016), p. 024015. DOI: 10.1103/PhysRevD.93.024015. URL: https://link.aps.org/doi/10.1103/PhysRevD.93.024015.

[42] David W Neilsen and Matthew W Choptuik. "Critical phenomena in perfect fluids." In: *Classical and Quantum Gravity* 17.4 (2000), pp. 761–782. DOI: 10.1088/0264-9381/17/4/303. URL: https://doi.org/10.1088/0264-9381/17/4/303.

[43] M. W. Choptuik. *The (Unstable) Threshold of Black Hole Formation*. 1998. arXiv: gr-qc/9803075 [gr-qc].

[44] Julia M Yeomans. *Statistical mechanics of phase transitions*. Clarendon Press, 1992.

[45] John Cardy. *Scaling and renormalization in statistical physics*. Vol. 5. Cambridge university press, 1996.

[46] Nigel Goldenfeld. *Lectures on phase transitions and the renormalization group*. CRC Press, 2018.

[47] Roger Penrose. ""Golden Oldie": Gravitational collapse: the role of general relativity." In: *General Relativity and Gravitation* 34.7 (2002), pp. 1141–1165.

[48] Demetrios Christodoulou. "On the global initial value problem and the issue of singularities." In: *Classical and Quantum Gravity* 16.12A (1999), A23–A35. DOI: 10.1088/0264-9381/16/12a/302. URL: https://doi.org/10.1088/0264-9381/16/12a/302.

[49] Andrew M. Abrahams and Charles R. Evans. "Critical behavior and scaling in vacuum axisymmetric gravitational collapse." In: *Phys. Rev. Lett.* 70 (20 1993), pp. 2980–2983. DOI: 10.1103/PhysRevLett.70.2980. URL: https://link.aps.org/doi/10.1103/PhysRevLett.70.2980.

[50] Andrew M. Abrahams and Charles R. Evans. "Universality in axisymmetric vacuum collapse." In: *Phys. Rev. D* 49 (8 1994), pp. 3998–4003. DOI: 10.1103/PhysRevD.49.3998. URL: https://link.aps.org/doi/10.1103/PhysRevD.49.3998.

[51] Tomá š Ledvinka and Anton Khirnov. "Universality of Curvature Invariants in Critical Vacuum Gravitational Collapse." In: *Phys. Rev. Lett.* 127 (1 2021), p. 011104. DOI: 10.1103/PhysRevLett.127.011104. URL: https://link.aps.org/doi/10.1103/PhysRevLett.127.011104.

[52] Miguel Alcubierre, G. Allen, B. Brügmann, G. Lanfermann, E. Seidel, W.-M. Suen, and M. Tobias. "Gravitational collapse of gravitational waves in 3D numerical relativity." In: *Phys. Rev. D* 61 (2000), 041501 (R). eprint: gr-qc/9904013.

[53] David Garfinkle and G. Comer Duncan. "Numerical evolution of Brill waves." In: *Phys. Rev. D* 63 (2001), p. 044011. eprint: gr-qc/0006073.

[54] Lucia Santamaria. "Nonlinear 3D Evolutions of Brillwave Sapcetimes and Critical Phenomena." MA thesis. Friedrich-Schiller-Universität Jena, 2006.

[55] O. Rinne. "Constrained evolution in axisymmetry and the gravitational collapse of prolate Brill waves." In: *Classical and Quantum Gravity* 25.13, 135009 (July 2008), p. 135009. DOI: 10.1088/0264-9381/25/13/135009. arXiv: 0802.3791 [gr-qc].

[56] Evgeny Sorkin. "On critical collapse of gravitational waves." In: *Class. Quant. Grav.* 28 (2011), p. 025011. DOI: 10.1088/0264-9381/28/2/025011. arXiv: 1008.3319 [gr-qc].

[57] David Hilditch, Thomas W. Baumgarte, Andreas Weyhausen, Tim Dietrich, Bernd Brügmann, Pedro J. Montero, and Ewald Müller. "Collapse of nonlinear gravitational waves in moving-puncture coordinates." In: *Phys. Rev. D* 88 (10 2013), p. 103009. DOI: 10.1103/PhysRevD.88.103009. URL: https://link.aps.org/doi/10.1103/PhysRevD.88.103009.

[58] David Hilditch, Andreas Weyhausen, and Bernd Brügmann. "Evolutions of centered Brill waves with a pseudospectral method." In: *Phys. Rev. D* 96 (10 2017), p. 104051. DOI: 10.1103/PhysRevD.96.104051. URL: https://link.aps.org/doi/10.1103/PhysRevD.96.104051.

[59] Anton Khirnov and Tomáš Ledvinka. "Slicing conditions for axisymmetric gravitational collapse of Brill waves." In: *Classical and Quantum Gravity* 35.21 (2018), p. 215003. DOI: 10.1088/1361-6382/aae1bc. URL: https://doi.org/10.1088/1361-6382/aae1bc.

[60] Isabel Suárez Fernández, Sarah Renkhoff, Daniela Cors Agulló, Bernd Bruegmann, and David Hilditch. *Evolution of Brill waves with an adaptive pseudospectral method*. 2022. arXiv: 2205.04379 [gr-qc].

[61] José M. Martín-García and Carsten Gundlach. "All nonspherical perturbations of the Choptuik spacetime decay." In: *Phys. Rev. D* 59 (6 1999), p. 064031. DOI: 10.1103/PhysRevD.59.064031. URL: https://link.aps.org/doi/10.1103/PhysRevD.59.064031.

[62] Matthew W. Choptuik, Eric W. Hirschmann, Steven L. Liebling, and Frans Pretorius. "Critical collapse of the massless scalar field in axisymmetry." In: *Phys. Rev. D* 68 (4 2003), p. 044007. DOI: 10.1103/PhysRevD.68.044007. URL: https://link.aps.org/doi/10.1103/PhysRevD.68.044007.

[63] James Healy and Pablo Laguna. "Critical Collapse of Scalar Fields Beyond Axisymmetry." In: *Gen. Rel. Grav.* 46 (2014), p. 1722. arXiv: 1310.1955 [gr-qc].

[64] Nils Deppe, Lawrence E. Kidder, Mark A. Scheel, and Saul A. Teukolsky. "Critical behavior in 3-d gravitational collapse of massless scalar fields." In: (2018). arXiv: 1802.08682 [gr-qc].

[65] Thomas W. Baumgarte. "Aspherical deformations of the Choptuik spacetime." In: *Phys. Rev. D* 98 (8 2018), p. 084012. DOI: 10.1103/PhysRevD.98.084012. URL: https://link.aps.org/doi/10.1103/PhysRevD.98.084012.

[66] Matthew W. Choptuik, Eric W. Hirschmann, Steven L. Liebling, and Frans Pretorius. "Critical Collapse of A Complex Scalar Field with Angular Momentum." In: *Phys. Rev. Lett* 93 (2004), p. 131101. eprint: gr-qc/0405101.

[67] Thomas W. Baumgarte, Carsten Gundlach, and David Hilditch. "Critical Phenomena in the Gravitational Collapse of Electromagnetic Waves." In: *Phys. Rev. Lett.* 123 (17 2019), p. 171103. DOI: 10.1103/PhysRevLett.123.171103. URL: https://link.aps.org/doi/10.1103/PhysRevLett.123.171103.

[68] Maria F. Perez Mendoza and Thomas W. Baumgarte. "Critical phenomena in the gravitational collapse of electromagnetic dipole and quadrupole waves." In: *Phys. Rev. D* 103 (12 2021), p. 124048. DOI: 10.1103/PhysRevD.103.124048. URL: https://link.aps.org/doi/10.1103/PhysRevD.103.124048.

[69] Isabel Suárez Fernández, Rodrigo Vicente, and David Hilditch. "Semilinear wave model for critical collapse." In: *Phys. Rev. D* 103 (4 2021), p. 044016. DOI: 10.1103/PhysRevD.103.044016. URL: https://link.aps.org/doi/10.1103/PhysRevD.103.044016.

[70] Isabel Suárez Fernández, Thomas W. Baumgarte, and David Hilditch. "Comparison of linear Brill and Teukolsky waves." In: *Phys. Rev. D* 104 (12 2021), p. 124036. DOI: 10.1103/PhysRevD.104.124036. URL: https://link.aps.org/doi/10.1103/PhysRevD.104.124036.

[71] Sarah Renkhoff. "A Pseudospectral method with Adaptive Mesh Refinement." PhD thesis. Jena, 07743 Jena, Germany: Friedrich-Schiller-Universitaet, 2022.

[72] Carsten Gundlach. "Understanding critical collapse of a scalar field." In: *Phys. Rev. D* 55 (2 1997), pp. 695–713. DOI: 10.1103/PhysRevD.55.695. URL: https://link.aps.org/doi/10.1103/PhysRevD.55.695.

[73] Shahar Hod and Tsvi Piran. "Fine structure of Choptuik's mass-scaling relation." In: *Phys. Rev. D* 55 (2 1997), R440–R442. DOI: 10.1103/PhysRevD.55.R440. URL: https://link.aps.org/doi/10.1103/PhysRevD.55.R440.

[74] Steven L. Liebling. "Singularity threshold of the nonlinear sigma model using 3D adaptive mesh refinement." In: *Phys. Rev. D* 66 (4 2002), p. 041703. DOI: 10.1103/PhysRevD.66.041703. URL: https://link.aps.org/doi/10.1103/PhysRevD.66.041703.

[75] Piotr Bizo, Tadeusz Chmaj, and Zbis aw Tabor. "On blowup for semilinear wave equations with a focusing nonlinearity." In: *Nonlinearity* 17.6 (2004), pp. 2187–2201. DOI: 10.1088/0951-7715/17/6/009. URL: https://doi.org/10.1088/0951-7715/17/6/009.

[76] Steven L. Liebling. "Threshold of singularity formation in the semilinear wave equation." In: *Phys. Rev. D* 71 (4 2005), p. 044019. DOI: 10.1103/PhysRevD.71.044019. URL: https://link.aps.org/doi/10.1103/PhysRevD.71.044019.

[77] Piotr Bizoń, Dieter Maison, and Arthur Wasserman. "Self-similar solutions of semilinear wave equations with a focusing nonlinearity." In: *Nonlinearity* 20.9 (2007), pp. 2061–2074. DOI:

10.1088/0951-7715/20/9/003. URL: https://doi.org/10.1088/0951-7715/20/9/003.

[78] Piotr Bizoń and Anıl Zenginoğlu. "Universality of global dynamics for the cubic wave equation." In: *Nonlinearity* 22.10 (2009), pp. 2473–2485. DOI: 10.1088/0951-7715/22/10/009. URL: https://doi.org/10.1088/0951-7715/22/10/009.

[79] Hans Ringström. *The Cauchy problem in general relativity*. Vol. 6. European Mathematical Society, 2009.

[80] Carsten Gundlach, Richard H. Price, and Jorge Pullin. "Late-time behavior of stellar collapse and explosions. I. Linearized perturbations." In: *Phys. Rev. D* 49 (2 1994), pp. 883–889. DOI: 10.1103/PhysRevD.49.883. URL: https://link.aps.org/doi/10.1103/PhysRevD.49.883.

[81] Sergiu Klainerman. "Global existence for nonlinear wave equations." In: *Communications on Pure and Applied Mathematics* 33.1 (1980), pp. 43–101. DOI: https://doi.org/10.1002/cpa.3160330104. eprint: https://onlinelibrary.wiley.com/doi/pdf/10.1002/cpa.3160330104. URL: https://onlinelibrary.wiley.com/doi/abs/10.1002/cpa.3160330104.

[82] Michael Reiterer and Eugene Trubowitz. "Choptuik's critical spacetime exists." In: *Communications in Mathematical Physics* 368.1 (2019), pp. 143–186.

[83] Piotr Bizo, Tadeusz Chmaj, and Zbis aw Tabor. "On blowup for semilinear wave equations with a focusing nonlinearity." In: *Nonlinearity* 17.6 (2004), pp. 2187–2201. DOI: 10.1088/0951-7715/17/6/009. URL: https://doi.org/10.1088/0951-7715/17/6/009.

[84] CHARLES ROSS EVANS II. *A METHOD FOR NUMERICAL RELATIVITY: SIMULATION OF AXISYMMETRIC GRAVITATIONAL COLLAPSE AND GRAVITATIONAL RADIATION GENERATION (STAR, NEUTRON, SUPERNOVA)*. The University of Texas at Austin, 1984.

[85] Heinz-Otto Kreiss and Joseph Oliger. *Methods for the approximate solution of time dependent problems*. 10. International Council of Scientific Unions, World Meteorological Organization, 1973.

[86] Pauli Virtanen, Ralf Gommers, Travis E Oliphant, Matt Haberland, Tyler Reddy, David Cournapeau, Evgeni Burovski, Pearu Peterson, Warren Weckesser, Jonathan Bright, et al. "SciPy 1.0: fundamental algorithms for scientific computing in Python." In: *Nature methods* 17.3 (2020), pp. 261–272.

[87] Terence Tao. "Finite-time blowup for a supercritical defocusing nonlinear wave system." In: *Analysis & PDE* 9.8 (2016), pp. 1999–2030.

[88] Eric Poisson and Werner Israel. "Internal structure of black holes." In: *Phys. Rev. D* 41 (6 1990), pp. 1796–1809. DOI: 10.1103/PhysRevD.41.1796. URL: https://link.aps.org/doi/10.1103/PhysRevD.41.1796.

[89] Vitor Cardoso, João L. Costa, Kyriakos Destounis, Peter Hintz, and Aron Jansen. "Quasinormal Modes and Strong Cosmic Censorship." In: *Phys. Rev. Lett.* 120 (3 2018), p. 031103. DOI: 10.1103/PhysRevLett.120.031103. URL: https://link.aps.org/doi/10.1103/PhysRevLett.120.031103.

[90] Saul A. Teukolsky. "Linearized quadrupole waves in general relativity and the motion of test particles." In: *Phys. Rev. D* 26 (4 1982), pp. 745–750. DOI: 10.1103/PhysRevD.26.745. URL: https://link.aps.org/doi/10.1103/PhysRevD.26.745.

[91] Dieter R. Brill. "On the positive definite mass of the Bondi-Weber-Wheeler time-symmetric gravitational waves." In: *Annals of Physics* 7.4 (1959), pp. 466–483. ISSN: 0003-4916. DOI: https://doi.org/10.1016/0003-4916(59)90055-7. URL: https://www.sciencedirect.com/science/article/pii/0003491659900557.

[92] Oliver Rinne. "Explicit solution of the linearized Einstein equations in the transverse-traceless gauge for all multipoles." In: *Classical and Quantum Gravity* 26.4 (2009), p. 048003. DOI: 10.1088/0264-9381/26/4/048003. URL: https://doi.org/10.1088/0264-9381/26/4/048003.

[93] D. E. Holz, W. A. Miller, M. Wakano, and J. A. Wheeler. "Coalescence of primal gravity waves to make cosmological mass without matter." In: *Directions in General Relativity: Volume 2: Proceedings of the 1993 International Symposium, Maryland: Papers in Honor of Dieter Brill*. Vol. 2. Cambridge University Press. 1993, p. 339.

[94] Wolfram Research, Inc. *Mathematica, Version 12.2*. Champaign, IL, 2020.

[95] Vincent Moncrief. "Gravitational perturbations of spherically symmetric systems. I. The exterior problem." In: *Annals of Physics* 88.2 (1974), pp. 323–342. ISSN: 0003-4916. DOI: https://doi.org/10.1016/0003-4916(74)90173-0. URL: https://www.sciencedirect.com/science/article/pii/0003491674901730.

[96] Alessandro Nagar and Luciano Rezzolla. "Gauge-invariant non-spherical metric perturbations of Schwarzschild black-hole spacetimes." In: *Classical and Quantum Gravity* 22.16 (2005), R167–R192. DOI: 10.1088/0264-9381/22/16/r01. URL: https://doi.org/10.1088/0264-9381/22/16/r01.

[97] Carsten Gundlach. "Understanding critical collapse of a scalar field." In: *Phys. Rev. D* 55 (1997), p. 695. eprint: gr-qc/9604019.

[98] Shahar Hod and Tsvi Piran. "Fine structure of Choptuik's mass-scaling relation." In: *Physical Review D* 55.2 (1997), R440.

[99] Harald P. Pfeiffer, Lawrence E. Kidder, Mark A. Scheel, and Deirdre Shoemaker. "Initial data for Einstein's equations with superposed gravitational waves." In: *Phys. Rev. D* 71 (2 2005), p. 024020. DOI: 10.1103/PhysRevD.71.024020. URL: https://link.aps.org/doi/10.1103/PhysRevD.71.024020.

[100] David Garfinkle. "Choptuik scaling in null coordinates." In: *Phys. Rev. D* 51 (1995), pp. 5558–5561.

[101] Carsten Gundlach, Thomas W. Baumgarte, and David Hilditch. "Critical phenomena in gravitational collapse with two competing massless matter fields." In: *Phys. Rev. D* 100 (10 2019), p. 104010. DOI: 10.1103/PhysRevD.100.104010. URL: https://link.aps.org/doi/10.1103/PhysRevD.100.104010.

[102] Bernd Brügmann. "A pseudospectral matrix method for time-dependent tensor fields on a spherical shell." In: *Journal of Computational Physics* 235 (2013), pp. 216–240. ISSN: 0021-9991. DOI: https://doi.org/10.1016/j.jcp.2012.11.007. URL: https://www.sciencedirect.com/science/article/pii/S0021999112006833.

[103] O Rinne. "Stable radiation-controlling boundary conditions for the generalized harmonic Einstein equations." In: *Classical and Quantum Gravity* 23.22 (2006), pp. 6275–6300. DOI: 10.1088/0264-9381/23/22/013. URL: https://doi.org/10.1088/0264-9381/23/22/013.

[104] Miguel Alcubierre, Bernd Brügmann, Daniel Holz, Ryoji Takahashi, Steven Brandt, Edward Seidel, and Jonathan Thornburg. "Symmetry without symmetry: Numerical simulation of axisymmetric systems using Cartesian grids." In: *International Journal of Modern Physics D* 10.03 (2001), pp. 273–289.

[105] Frans Pretorius. "Evolution of Binary Black-Hole Spacetimes." In: *Phys. Rev. Lett.* 95 (12 2005), p. 121101. DOI: 10.1103/PhysRevLett.95.121101. URL: https://link.aps.org/doi/10.1103/PhysRevLett.95.121101.

[106] Jan S Hesthaven. "Spectral penalty methods." In: *Applied Numerical Mathematics* 33.1-4 (2000), pp. 23–41.

[107] Jan S Hesthaven, Sigal Gottlieb, and David Gottlieb. *Spectral methods for time-dependent problems*. Vol. 21. Cambridge University Press, 2007.

[108] Nicholas W Taylor, Lawrence E Kidder, and Saul A Teukolsky. "Spectral methods for the wave equation in second-order form." In: *Physical Review D* 82.2 (2010), p. 024037.

[109] Sarah Renkhoff. https://git.tpi.uni-jena.de/srenkhoff/ahloc3d.

[110] Erik Schnetter. "A fast apparent horizon algorithm." gr-qc/0206003. 2002.

[111] K. P. Tod. "Looking for marginally trapped surfaces." In: *Class. Quantum Grav.* 8 (1991), pp. L115–L118.

[112] Anton Khirnov. "Representation of dynamical black hole spacetimes in numerical simulations." PhD thesis. Charles University, Prague, 2021.

[113] David Hilditch. "Dual Foliation Formulations of General Relativity." In: (2015). arXiv: 1509.02071 [gr-qc].

[114] David Hilditch, Enno Harms, Marcus Bugner, Hannes Rüter, and Bernd Brügmann. "The evolution of hyperboloidal data with the dual foliation formalism: Mathematical analysis and wave equation tests." In: *Class. Quant. Grav.* 35.5 (2018), p. 055003. DOI: 10.1088/1361-6382/aaa4ac. arXiv: 1609.08949 [gr-qc].

[115] Maitraya K. Bhattacharyya, David Hilditch, K. Rajesh Nayak, Sarah Renkhoff, Hannes R. Rüter, and Bernd Brügmann. "Implementation of the dual foliation generalized harmonic gauge formulation with application to spherical black hole excision." In: *Phys. Rev. D* 103 (6 2021), p. 064072. DOI: 10.1103/PhysRevD.103.064072. URL: https://link.aps.org/doi/10.1103/PhysRevD.103.064072.

[116] David Garfinkle and Frans Pretorius. "Spike behavior in the approach to spacetime singularities." In: *Phys. Rev. D* 102 (12 2020), p. 124067. DOI: 10.1103/PhysRevD.102.124067. URL: https://link.aps.org/doi/10.1103/PhysRevD.102.124067.

[117] Isabel Cordero-Carrión, Pablo Cerdá-Durán, and José María Ibáñez. "Gravitational waves in dynamical spacetimes with matter content in the fully constrained formulation." In: *Phys. Rev. D* 85 (4 2012), p. 044023. DOI: 10.1103/PhysRevD.85.044023. URL: https://link.aps.org/doi/10.1103/PhysRevD.85.044023.

[118] George B. Arfken and Hans J. Weber. *Mathematical methods for physicists, 6th ed.* Elsevier, 2005.

[119] J. D. Hunter. "Matplotlib: A 2D graphics environment." In: *Computing in Science & Engineering* 9.3 (2007), pp. 90–95. DOI: 10.1109/MCSE.2007.55.

COLOPHON

Most symbolic calculations in this thesis were carried out in `Mathematica` [94]. The numerical code of Chapter 2 was written in `Python`. Most of the document plots were rendered with the library `matplotlib` [119]. This document was typeset using the template `classicthesis` developed by André Miede and Ivo Pletikosić.

Final Version as of July 20, 2022 (Final version).